

MNRAS **540,** 871–906 (2025) Advance Access publication 2025 May 2

AT 2018dyk: tidal disruption event or active galactic nucleus? Follow-up observations of an extreme coronal line emitter with the Dark Energy Spectroscopic Instrument

Peter Clark , 1.2* Joseph Callow , 2 Or Graur , 2.3 Claire Greenwell , 4 Lei Hu , 5 Jessica Aguilar , 6 Steven Ahlen , 7 Davide Bianchi , 8 David Brooks , 9 Todd Claybaugh , 6 Kyle Dawson , 10 Axel de la Macorra , 11 Peter Doel , 9 Satya Gontcho A Gontcho , 6 Gaston Gutierrez , 12 Klaus Honscheid , 13,14 Stephanie Juneau , 15 Robert Kehoe, 16 Theodore Kisner , 6 Anthony Kremin , 6 Martin Landriau , 6 Laurent Le Guillou , 17 Aaron Meisner , 15 Ramon Miquel , 18,19 John Moustakas , 20 Ignasi Pérez-Ràfols , 21 Eusebio Sanchez , 22 Michael Schubnell , 23 David Sprayberry, 15 Gregory Tarlé , 23 Benjamin A. Weaver , and Hu Zou , 24

Affiliations are listed at the end of the paper

Accepted 2025 April 29. Received 2025 April 24; in original form 2025 February 6

ABSTRACT

We present fresh insights into the nature of the tidal disruption event (TDE) candidate AT 2018dyk. AT 2018dyk has sparked a debate in the literature around its classification as either a bona-fide TDE or as an active galactic nucleus (AGN) turn-on state change. A new follow-up spectrum taken with the Dark Energy Spectroscopic Instrument, in combination with host-galaxy analysis using archival SDSS–MaNGA data, supports the identification of AT 2018dyk as a TDE. Specifically, we classify this object as a TDE that occurred within a gas-rich environment, which was responsible for both its mid-infrared (MIR) outburst and development of Fe coronal emission lines. Comparison with the known sample of TDE-linked extreme coronal line emitters (TDE-ECLEs) and other TDEs displaying coronal emission lines (CrL-TDEs) reveals similar characteristics and shared properties. For example, the MIR properties of both groups appear to form a continuum with links to the content and density of the material in their local environments. This includes evidence for a MIR colour–luminosity relationship in TDEs occurring within such gas-rich environments, with those with larger MIR outbursts also exhibiting redder peaks.

Key words: galaxies: active – transients: tidal disruption events.

1 INTRODUCTION

The supermassive black holes (SMBHs) at the centres of galaxies can produce numerous astrophysical phenomena, including tidal disruption events (TDEs). These are luminous flaring transients produced by the gravitational shredding of a star that passes too close to its galaxy's SMBH and result in a portion of the star's mass being accreted onto the SMBH with the remaining being ejected from the system (Ulmer 1999). Whilst the specific mechanisms responsible for the associated ultraviolet (UV)/optical emission remain debated, a combination of the circularization of the disrupted material to form an accretion disc around the SMBH and collisions within the infalling material streams are likely the primary processes involved (e.g., Lacy, Townes & Hollenbach 1982; Rees 1988; Evans & Kochanek 1989; Phinney 1989). TDEs were first identified in the 1990s within X-ray surveys, the energy regime where the overall peak of TDE emission occurs (Bade, Komossa & Dahlem 1996). TDEs are now routinely detected by wide-field optical surveys, with

TDEs cause rapid increases in the accretion rates of material onto SMBHs and can occur around SMBHs regardless of previous levels of activity. Already 'active' SMBHs (i.e., those with ongoing accretion rates sufficient to form accretion discs) are located within active galactic nuclei (AGNs). The presence of an AGN can have a significant effect on the resulting spectrum of its host galaxy, with the energy output of an active SMBH potentially exceeding that of the galaxy's stellar population. The spectra of AGN can display narrow or broad emission lines overlaid on a power-law continuum of emission, with the AGN unification model positing the observer's viewing angle of the accretion disc explains the significant observed diversity despite the identical physical processes involved across AGN classifications (Antonucci 1993; Netzer 2015). AGNs are known to display variability on a range of time-scales and across the electromagnetic spectrum as a result of instabilities within the feeder accretion discs. For example, a drop in the SMBH's accretion rate will lead to a reduction of an AGN's output, while a temporary increase in the accretion rate can lead to flares in emission (e.g., Ulrich, Maraschi & Urry 1997).

subsequent follow-up observations also having detected TDEs at radio and infrared (IR) wavelengths – for example, Alexander et al. (2017) and Dou et al. (2017), respectively.

^{*} E-mail: P.S.J.Clark@soton.ac.uk

Table 1. Properties of AT 2018dyk.

Parameter	Value	Source
Host galaxy	SDSS J153308.01+443208.4	
Right ascension	233.2833955	1
Declination	+ 44.5356122	1
Redshift	0.0367^{\dagger}	1
E(B-V) – Milky Way	0.0164 mag	2
Alternative identifiers	ZTF18aajupnt, WTP 18aamced	

Notes. † Retrieved from the TNS and consistent with the pre-transient SDSS spectrum. The redshift value returned by the DESI redshift measuring pipeline REDROCK (Guy et al. 2023, Bailey et al., in preparation) returns a slightly different redshift value of 0.0368. We believe this offset is due to the increasing strength of the anomalously redshifted [O III] lines (see Section 4.1) at the time of the DESI spectrum and as such we adopt the value determined before these lines strengthened post outburst.

Sources:

- 1. Transient Name Server (TNS): https://www.wis-tns.org/object/2018dyk
- 2: IRSA Galactic Dust Reddening and Extinction: https://irsa.ipac.caltech.edu/applications/DUST/

As TDEs and AGN variability are both produced through accretion of material onto a SMBH, it can be difficult to distinguish between the two. There are, however, differences in properties that can be used to separate the two. TDEs are distinct events rather than ongoing processes and as such have defined beginnings, peaks, and ends, compared to AGN, which will show repeated increases and decreases in luminosity over time. TDEs also tend to produce brighter peaks in luminosity (with outbursts several magnitudes brighter than the quiescent host galaxy flux), whilst the variability in AGN tends to be on the level of 0.1 mag (though some AGN have been seen to also produce bright flares e.g., Neustadt et al. 2023). The types and evolution of spectral features exhibited by TDEs and AGNs can also be used to distinguish between the two. Despite these differences, some observed transients remain difficult to definitively classify; one such example, AT 2018dyk, is the subject of this work.

AT 2018dyk was first detected on 2018 May 31 (MJD 58269.31) by the Zwicky Transient Facility (ZTF; Bellm et al. 2019) with a *g*-band magnitude of 19.41 (Fremling 2023). The host galaxy was determined to have a redshift of 0.0367 (Table 1). It was classified as a TDE due to the presence of broad Balmer and He II emission lines (Arcavi et al. 2018), though was noted to have narrow emission lines that had not been previously observed in TDEs and was fainter than most such transients.

Frederick et al. (2019) found that the host galaxy of AT 2018dyk transitioned from a low-ionization nuclear emission-line region (LINER) galaxy to a narrow-line Seyfert 1 (NLSy1) galaxy and so classified this event as the turn-on phase of this transition rather than being the result of a TDE, with AT 2018dyk being included in their sample of 'changing look' LINERs (CL-LINERs). LINERs present an additional difficulty for distinguishing between true TDEs and AGN activity, as the source of the emission lines is also ambiguous, with a weak underlying AGN or evolved stellar populations in the nucleus of a galaxy containing a quiescent SMBH both being possible sources. This is in comparison to Seyfert galaxies, whose spectral properties are conclusively the result of an AGN.

AT 2018dyk was also included in the sample of Ambiguous Nuclear Transients (ANTs) investigated by Hinkle (2024). ANTs are objects displaying narrow UV/optical emission features and smooth photometric evolution but unclear, likely multiple possible origins (e.g., Wiseman et al. 2023, 2025). In that work, AT 2018dyk was determined to have a high dust covering fraction (0.42 \pm 0.15:

a value much larger than typical TDEs) and mid-infrared (MIR) behaviour consistent with a dust reprocessing echo. ANTs were generally found to occur in hosts currently displaying AGN activity; that recently hosted an AGN; or whose nuclei had a high dust fraction due to other processes, such as significant star formation. Hinkle (2024) also noted that whilst the dust covering factors of the ANT sample are similar to those of AGNs, the evolution of the events are unlike AGN outbursts.

AT 2018dyk was revisited by Huang et al. (2023), who used further multiwavelength observations to reassess the CL-LINER classification. The variability of AT 2018dyk was found to be shorter lived than typical variability in AGNs, and it showed none of the characteristic trends between colour and brightness that have previously been seen in such objects. The optical light curve was found to follow the characteristic $t^{-\frac{5}{3}}$ power law expected of TDEs, and a TDE scenario was also able to explain the ~ 140 d lag between the optical and X-ray light-curve peaks. They concluded that AT 2018dyk was a TDE that had occurred in an LINER. However, they also noted that the mass of the black hole in the host galaxy of AT 2018dyk was high for a TDE host, with mass estimates based on luminosity, bulge mass, and velocity dispersion measured by Frederick et al. (2019) ranging from 7.6–8.0 $\log_{10}(M_{\odot})$, though we note here that the mass estimate provided by the virial method is much lower at $5.5 \log_{10}(M_{\odot})$ as derived from the low measured velocity of the H β line. The highest mass estimates are close to the Hills mass (Hills 1975) for Solar type stars – the upper mass limit for SMBHs for which the tidal radius is outside the event horizon and thus is capable of producing a visible TDE. Huang et al. (2023) also noted the presence of a dusty torus around the nucleus of the host galaxy.

Designated WTP 18aamced, AT 2018dyk was also included in the silver sample of MIR TDEs selected from Near-Earth Object Widefield Infrared Survey Explorer (NEOWISE) flares by Masterson et al. (2024). The authors excluded it from their gold sample due to its preflare LINER emission features, which may have marked it as an AGN contaminant.

The optical spectra following the discovery of AT 2018dyk exhibited the high-ionization (coronal) iron emission lines [Fe VII] $\lambda 5722$ Å, [Fe VII] $\lambda 6088$ Å, [Fe X] $\lambda 6376$ Å, and [Fe XIV] λ 5314 Å. The presence of these lines requires the presence of a extreme UV/soft X-ray continuum, with required photon energies exceeding ~ 100 eV, which identifies AT 2018dyk as an extreme coronal line emitter (ECLE). In objects where these emission lines are transient in nature, they are thought to be produced by TDEs, where X-rays generated by the accretion of the tidally disrupted star's matter are absorbed and reprocessed by the surrounding interstellar medium (ISM; Komossa et al. 2008; Wang et al. 2011, 2012; Yang et al. 2013; Callow et al. 2024, 2025; Clark et al. 2024; Hinkle, Shappee & Holoien 2024). Such coronal lines have also been observed in some Type IIn supernovae (SNe), but the lines were much weaker than those seen in either type of ECLE (Izotov & Thuan 2009; Smith et al. 2009).

Where these ECLE line signatures do not vary on a time-scale of years to decades, such objects are thought to be exotic AGNs in gas-rich environments that produce unusually strong coronal line signatures. High-ionization Fe coronal lines are present in some Seyfert galaxies but only at the level of a few per cent the line strength of [O III] λ 5007 Å (Nagao, Taniguchi & Murayama 2000). As discussed by Frederick et al. (2019), the spectra of AT 2018dyk obtained around peak brightness match the criteria set out by Wang et al. (2012) to classify it as an ECLE (the [Fe x] line was stronger than [O III] λ 5007 Å where Wang et al. 2012 require coronal line strength greater than 20 per cent that of [O III] λ 5007 Å).

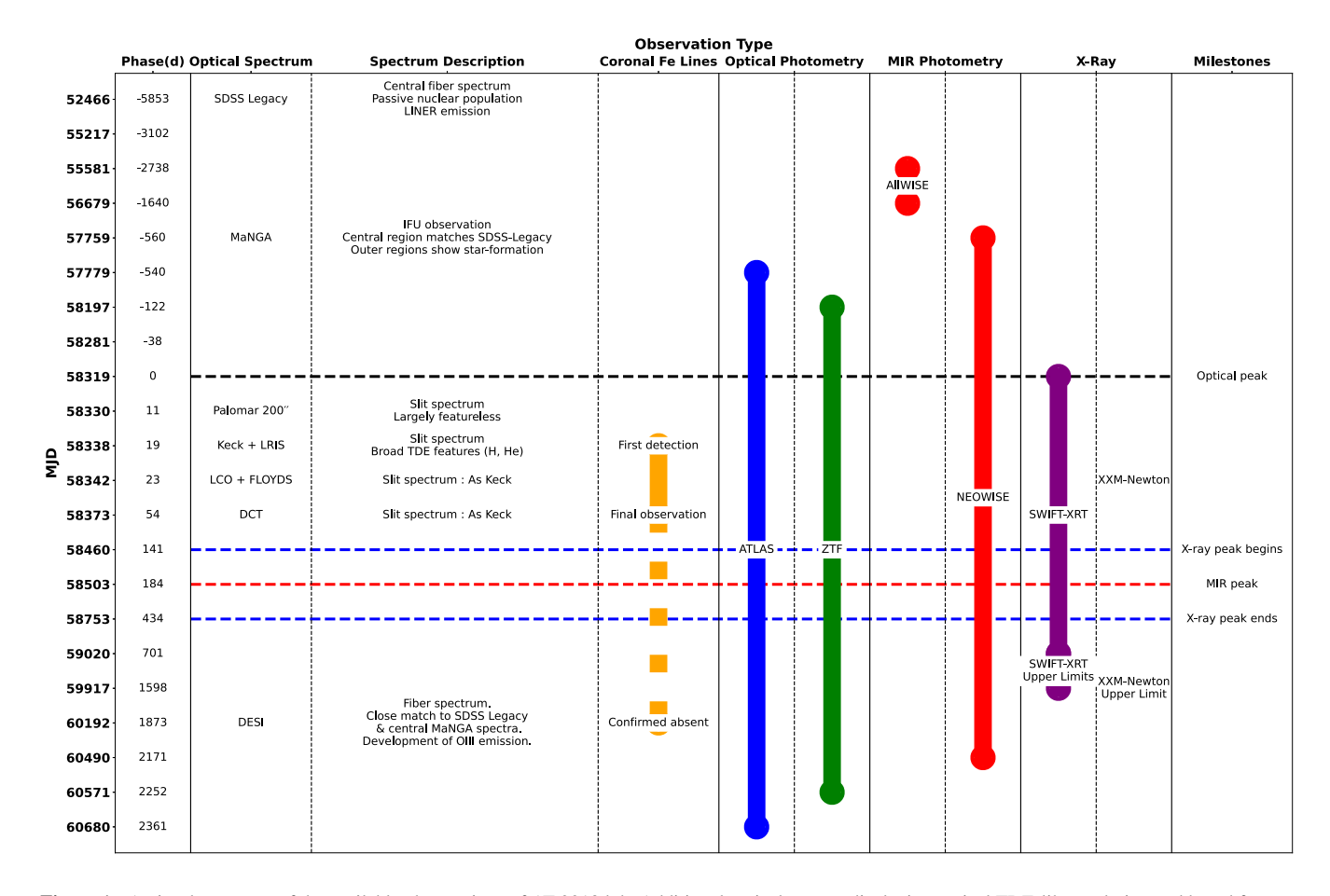


Figure 1. A visual summary of the available observations of AT 2018dyk. Additional optical spectra displaying typical TDE-like evolution and broad features exist between the LCOGT+FLOYDS and the DCT spectrum. All show similar coronal and other emission features. As these have not been made available publicly, we do not utilize them further in this work. Two observations of *HST* UV spectra were also obtained at phases of +182 and +226 d. We do not make use of these spectra within this work as there are no comparable observations for the other objects in the sample. The additional optical and UV spectra can be viewed in Frederick et al. (2019).

We utilize a new spectrum of AT 2018dyk, obtained several years post outburst, obtained by the Dark Energy Spectroscopic Instrument (DESI; Levi et al. 2013; DESI Collaboration 2016a, b, 2022, 2024g), to explore the long-term evolution of AT 2018dyk and conclusively identify it as a transient generated by a TDE rather than AGN activity.

In this paper, we perform a detailed analysis of AT 2018dyk and seek to settle the discussion on its origin. In Section 2, we discuss the spectroscopic, photometric, and comparative data sets constructed for the analysis. In Section 3, we first analyse the optical spectroscopic evolution of AT 2018dyk and its host galaxy over a timespan of more than 20 yr, placing this evolution in context with other transient populations through comparisons with similar events. We then move on to an analysis of its MIR evolution and include a detailed study of its host galaxy's properties, with a focus on determining the source of its LINER emission features. In Section 4, we discuss the implications of the evolution of AT 2018dyk's oxygen emission behaviour, as well as the MIR outburst properties of the transient in the context of ECLEs, TDEs ,and CL-LINERs. Finally, in Section 5, we conclude that the evolution of AT 2018dyk is well matched by variable or ECLEs assumed to be caused by TDEs (TDE-ECLEs) though on a faster evolutionary time-scale (Callow et al. 2024; Clark et al. 2024). To minimize potential confusion between 'coronal line' and 'changing look' objects, we abbreviate 'coronal line' to 'CrL' and 'changing look' to 'CL'.

Throughout, we assume a Hubble–Lemaître constant $H_0=73$ km s⁻¹ Mpc⁻¹ and adopt a standard cosmological model with $\Omega_M=0.27$ and $\Omega_\Lambda=0.73$.

2 OBSERVATIONS AND DATA REDUCTION

Here, we describe the collection and reduction of the spectroscopic and photometric data sets used in this work. Additionally, a summary of all the various observations of AT 2018dyk across all wavelength regimes is presented visually in Fig. 1.

2.1 Optical spectroscopy

The DESI spectrum of AT 2018dyk presented in this work (Fig. 2) was obtained on 2023 May 05 (MJD 60192) as part of the Bright Galaxy Survey (Hahn et al. 2023) during main survey operations (Schlafly et al. 2023). The spectrum was processed by the custom DESI spectroscopic pipeline, which includes a full suite of processing and correction steps to provide fully flux- and wavelength-calibrated spectra (Guy et al. 2023). DESI itself is designed primarily as a cosmological experiment, and whilst not the focus of this work, Data Release 1 (DESI Collaboration 2025) provides a range of state-of-the-art cosmological analyses, including two-point clustering measurements and validation (DESI Collaboration 2024a), baryon-acoustic oscillation (BAO) measurements from galaxies and quasars (DESI Collaboration 2024b), and from the Lya forest (DESI

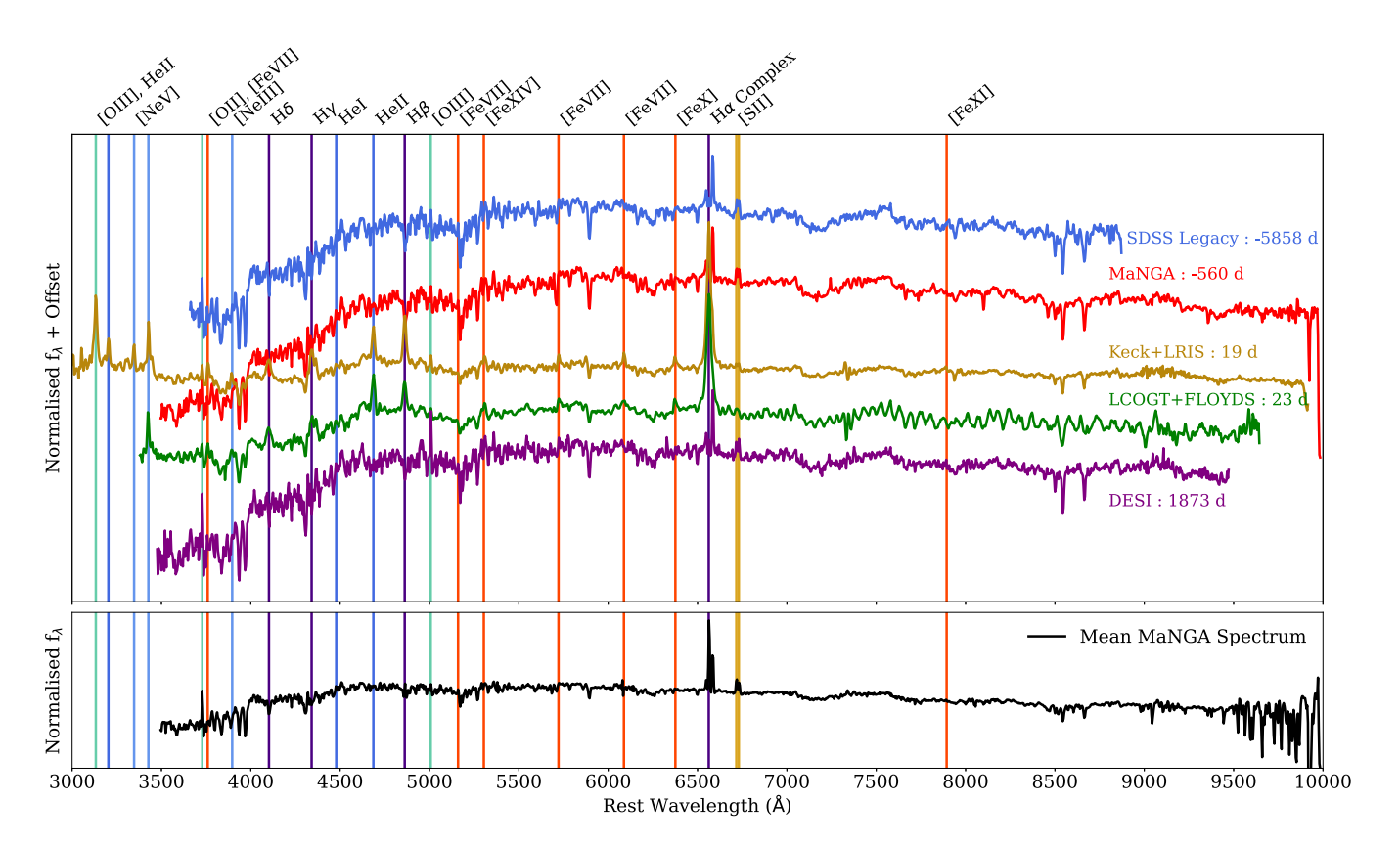


Figure 2. Spectroscopic evolution of AT 2018dyk with observations from 16 yr before and more than 5 yr following optical peak. Top panel: comparison between the normalized fibre and long-slit spectra of AT 2018dyk showing the emergence and subsequent fading of broad H and He features along with Fe coronal lines. The MaNGA spectrum shown here is from the local region of AT 2018dyk and consists of one spaxel (31, 31). The phase of each spectrum relative to the peak of the optical outburst is indicated. Bottom panel: normalized mean MaNGA spectrum covering all spaxels, showing the star-forming nature of SDSS J1533+4432 as a whole. In all cases, spectra have been Gaussian smoothed ($\sigma = 1$) and rebinned to a resolution of 4 Å. For all plots in this work, solid vertical lines are used to indicate the location of important spectral features. Additionally, these have a shared colour scheme where lines from the same element are displayed using the same colour, e.g., orange for all Fe emission lines.

Collaboration 2024c), as well as a full-shape study of galaxies and quasars (DESI Collaboration 2024d). There are cosmological results from the BAO measurements (DESI Collaboration 2024e) and the full-shape analysis (DESI Collaboration 2024f).

We compare our DESI spectrum to the archival Sloan Digital Sky Survey (SDSS; York et al. 2000) Legacy spectrum of the host of AT 2018dyk, SDSS J1533+4432, retrieved from the 17th data release (DR17; Abdurro'uf et al. 2022). This spectrum was obtained on 2002 July 11 (MJD 52466), providing a separation of 7726 d (21.15 yr) between the earliest archival spectrum of this object and the most recent DESI spectroscopic observation. This timescale provides a long baseline to compare the prior behaviour of the transient's host galaxy to the outburst itself, which returned to photometric quiescence over ~2 yr. This is comparable to the wider population of TDEs, which primarily evolve on similar time-scales (Charalampopoulos et al. 2022), with the longer term presence of UV-optical plateaus (van Velzen et al. 2019; Mummery et al. 2024).

The host galaxy of AT 2018dyk was observed as part of the SDSS-IV Mapping Nearby Galaxies at Apache Point Observatory survey (MaNGA; Smee et al. 2013; Bundy et al. 2015; Yan et al. 2016). This observation was obtained on 2017 January 6 (MJD 57759), 5293 d following the original spectrum and 560 d prior to the optical peak of AT 2018dyk. The MaNGA spectrum provides spatially resolved integral field unit (IFU) spectroscopy of SDSS J1533+4432. In this work, we use the reduced data processed by the MaNGA data analysis

pipeline (Belfiore et al. 2019; Westfall et al. 2019), accessed via the MARVIN toolkit (Cherinka et al. 2019).

Finally, we retrieve two publicly available spectra from the Weizmann Interactive Supernova Data Repository (WISeREP) online archive (Yaron & Gal-Yam 2012),¹ obtained close to the optical peak of the transient. The first spectrum was obtained with the low-resolution imaging spectrometer (LRIS; Oke et al. 1995) on the Keck telescope by the ZTF team on 2018 August 8 (MJD 58338), 19 d following the observed peak. The second spectrum was obtained with the FLOYDS spectrograph² on the 2-m Las Cumbres Observatory telescope (LCOGT) on Haleakala, Hawai'i, as part of the 'Transients in Galaxy Centers' observational program (PI: I. Arcavi) on 2018 August 12 (MJD 58342), 23 d following maximum light. A summary of the spectroscopic data used in this work is given in Table 2.

An additional set of optical spectra was obtained in the phase range +11–54 d and described by Frederick et al. (2019). Spectra observed prior to the +19 d Keck + LRIS spectrum are similar to the the archival SDSS Legacy and MaNGA spectra with the exception of increased Balmer emission. Spectra following the +19 d Keck + LRIS spectrum in this set displayed similar emission features (including the coronal lines) and minimal evolution. Two *Hubble*

¹https://wiserep.weizmann.ac.il/

²https://lco.global/observatory/instruments/floyds

Table 2. Spectroscopic observations of AT 2018dyk and its host galaxy (SDSS J1533+4432) used in this work.

Source	Туре	MJD	Phase (d) ¹	R^2	Source
SDSS Legacy	Fibre	52466	-5853	1500–2500	SDSS DR17
MaNGA	IFU	57759	-560	2000	SDSS DR17
Keck + LRIS	Slit	58338	+19	~ 4760	WISeREP
LCOGT + FLOYDS	Slit	58342	+23	400-700	WISeREP
DESI	Fibre	60192	+1873	1500-4000	This work

Notes. ¹Here and throughout the paper, phase is quoted relative to the optical peak (MJD 58319) as measured by Huang et al. (2023) in ZTF observations. ²Spectral resolving power. Quoted based on instrumental specifications.

Space Telescope (HST) UV spectra were also obtained as part of the follow-up program conducted by Frederick et al. (2019) at phases of +182 and +226 d. As we have no additional observations covering this wavelength regime, or additional comparison spectra from other similar objects, we do not explore this wavelength regime further in this work.

2.2 Photometry

In addition to spectroscopy, we make use of photometric observations from both optical and IR surveys. These are summarized in Table 3. In the optical regime, we use observations taken by the Asteroid Terrestrial-impact Last Alert System (ATLAS; Tonry et al. 2018; Smith et al. 2020) and ZTF (Bellm 2014; Bellm et al. 2019).

ATLAS data were retrieved using the ATLAS forced-photometry server (Shingles et al. 2021).³ ATLAS uses two broad-band filters: 'cyan' (c; approximately equivalent to g + r) and 'orange' (o; approximately equivalent to r + i). ATLAS observations are available over the MJD range (following the removal of some early unreliable observations) 57779–60680 and thus cover a time range prior to, during, and post outburst and were processed using a modified version of PLOT_ATLAS_FP.PY (Young 2024).

ZTF observations were made using the *gri* filters, and retrieved using the ZTF Forced Photometry Service (Masci et al. 2023). These observations cover an MJD range of 58197–60571.

In Section 3.3, we use both ATLAS and ZTF photometry to look for post-transient variability in the host galaxy, such as repeating outburst behaviour.

In an identical manner to Clark et al. (2024), we retrieve and process the available MIR photometry of AT 2018dyk and its host from both the AllWISE Data Release and the final NEOWISE Reactivation Release (NEOWISE-R) from the through the NASA/IPAC infrared science archive (IRSA).⁴ This processing includes the removal of any individual observations suffering from potential problems (such as contamination by excess moonlight, or being obtained when the spacecraft was close to the south Atlantic anomaly) and combining the individual observations from each visit to provide a single weighted average. The MIR behaviour of AT 2018dyk was previously investigated by Huang et al. (2023) and Masterson et al. (2024). In this work, we compare the MIR behaviour of AT 2018dyk to that of TDEs and ECLEs (Section 3.4) and include more recent observations available in the final NEOWISE data release.

Throughout this work, apparent magnitudes are given as observed. For absolute magnitudes, a correction for Milky Way extinction was applied using the appropriate photometric extinction coefficients which, unless specified otherwise, were retrieved from Schlafly & Finkbeiner (2011). To match the preferred extinction parameters of

Schlafly & Finkbeiner (2011), we use the extinction law of Fitzpatrick (1999) and assume $R_V = 3.1$.

2.3 Comparison objects

Whilst this work focuses extensively on the behaviour and properties of AT 2018dyk itself, it also makes use of comparisons to other ECLEs and traditionally identified TDEs that are known to have displayed Fe coronal emission.

In comparisons between AT 2018dyk and other objects, this paper makes a distinction between coronal-line TDEs (CrL-TDEs), which were spectroscopically confirmed as TDEs prior to the development of Fe coronal emission features, and TDE-linked ECLEs (TDE-ECLEs), which were identified initially through their coronal emission lines after the traditional UV/optical signatures had faded. Physically, however, these objects are fundamentally identical, with TDE-ECLEs representing a subpopulation with long durations that happened to be observed at a late stage in their evolution.

Additionally, several objects show evidence for multiple epochs of TDE associated MIR emission, either through distinct outburst episodes or through extended and multipeaked MIR rises. We refer to these as 'multi-epoch' events and include them as comparison objects only if the MIR light curve suggests one extended period of activity. All of the selected comparison objects are summarized in Table 4.

To better place these objects in context with the wider transient population, we also make use of the WISE MIR photometry for the optically selected TDE 2019azh, which displayed a weak MIR outburst, but no Fe coronal line emission (Faris et al. 2024) along with the two known AGN-ECLEs to compare and contrast their MIR behaviour. An optical spectral comparison between AT 2018dyk and the AGN-ECLEs has also been conducted.

Furthermore, we also compare the MIR behaviour of AT 2018dyk to the other members of the CL-LINER classification of Frederick et al. (2019).

3 ANALYSIS

First, we summarize the optical spectroscopic evolution of AT 2018dyk with a focus on the evolution displayed in our new DESI spectrum (Section 3.1). Next, we compare the optical spectra of AT 2018dyk at various phases to a range of other astrophysical objects to provide context on the behaviour of AT 2018dyk before, during, and post outburst (Section 3.2). We then conduct a search for signs of more recent transient activity in optical photometric observations (Section 3.3). Finally, we analyse the MIR behaviour of AT 2018dyk including a comparative analysis to other transients) before completing the analysis with an in-depth study of the properties of its host galaxy (Section 3.4).

³https://fallingstar-data.com/forcedphot/

⁴https://irsa.ipac.caltech.edu/

Table 3. Photometric observations used in this work.

Survey	MJD	Phase (d) ¹	Filters	Reference
Optical				
ATLAS	57779-60680	-540 to 2361	c , o^2	Tonry et al. (2018); Shingles et al. (2021)
ZTF	58197-60571	-122 to 2252	g, r, i	Bellm et al. (2019); Masci et al. (2023)
MIR				
AllWISE	55217-55581	-3102 to -2738	W1, W2, W3	Wright et al. (2010)
NEOWISE	56679-60490	-1640 to 2171	W1, W2	Mainzer et al. (2014)

Notes. ¹Phase quoted relative to ZTF optical peak as measured by Huang et al. (2023): MJD 58319.

3.1 Spectroscopic evolution

The pre-outburst SDSS Legacy optical spectrum was obtained just over 16 yr prior to the optical peak of AT 2018dyk and displays the typical spectral features of a largely passive stellar population with LINER emission-line diagnostics. The SDSS Legacy spectrum was obtained through a nuclear targeted fibre 3 arcsec in diameter. It covers the central and bar regions of SDSS J1533+4432 but does not capture the outer star-forming regions, which when explored using the MaNGA data show much bluer spectra with the prominent $H\alpha$ emission expected from star-forming regions. Indeed, the mean MaNGA spectrum produced from a combination of all observed spaxels (covering a large fraction of SDSS J1533+4432, with each having a width of 0.5 arsec) has the expected strong H α emission and non-LINER emission-line diagnostics of a normal star-forming galaxy (see the bottom panel of Fig. 2 and Section 3.5). The local environment of AT 2018dyk, as revealed by the central MaNGA spaxel coincident with its location (MJD 57759), consists of an older - and redder - stellar population with little active star formation but prominent [N II] emission lines observed in LINERs.

Following the outburst, broad H and He typical of optically selected TDEs developed, as seen in the Keck and LCOGT spectra included in Fig. 2. As noted by Frederick et al. (2019), in addition to these typical features, Fe coronal lines had emerged by the time of the Keck spectrum (MJD 58338, 19 d post-optical peak) and persisted until at least 2018 September 12 (MJD 58373, 54 d post peak for a minimum duration of 35 d) as observed in the Discovery Channel Telescope (DCT) spectrum presented by Frederick et al. (2019). However, given the slow evolution of the coronal lines observed in other TDEs, it is reasonable to assume their true duration is longer than this lower limit; see, for example, AT 2017gge (Onori et al. 2022) and the original TDE-ECLE sample (Wang et al. 2012; Yang et al. 2013; Clark et al. 2024). Additionally, since all Fe coronal lines had faded prior to the DESI observation, we can derive an (albeit loose) upper limit on the duration of the coronal line emission of <1819 d (time between the DCT and DESI spectra). In summary, Fe coronal line emission in AT 2018dyk commenced 19 d following the peak of optical emission and persisted for between 35 and 1819 d. In addition to the Fe coronal lines, coronal emission lines from [Ne V] are present in the Keck, LCOGT, and DCT spectra. These lines have very similar energy requirements to [Fe VII] and independently confirm the existence of a high-energy continuum. Unfortunately neither the pre-outburst nor the DESI spectra extend blueward enough for a comparative analysis, though a similar evolution to [Fe VII] is

As seen in other CrL-TDEs, the start of an X-ray flaring event was also observed prior to the emergence of the coronal lines. This is consistent with the coronal lines resulting from X-ray reprocessing by material close to the SMBH. Despite the small number of

CrL-TDEs currently known (15 at time of writing based on public reports of coronal line emission in classified TDEs), there is already a significant range in observed delays between the optical peak and the ensuing X-ray emission. In the case of AT 2018dyk, this X-ray emission peaked \sim 140 d following the optical peak as reported by Huang et al. (2023). Whilst the X-ray peak is not covered by the available optical spectra, the Keck and LCOGT spectra were taken whilst the X-ray emission was on the rise and the high ionization potential of the Fe coronal lines requires the presence of a strong X-ray continuum which, given the previous X-ray non-detections, was not previously present in this object.

The most recent spectrum of AT 2018dyk is the DESI spectrum obtained more than 5 yr post-optical peak (MJD 60192). This spectrum now closely resembles the archival pre-outburst SDSS spectrum (Fig. 2). The broad H and He features and coronal lines are no longer present, and the original continuum shape is now restored. In Fig. 3, we show the evolution of the H α complex and [O III] λ 5007 Å line region (with local normalization and no smoothing or rebinning). Whilst H α , H β , [N II], and [S II] emission lines have now returned to their quiescent states, the same cannot be said for [O III] λ 5007 Å, which has significantly strengthened compared to the pre-outburst SDSS spectrum. This evolution is also seen in the behaviour of the [O II] λ 3727 Å emission line. We discuss this evolution in Section 4.1.

We note here that the SDSS Legacy and DESI spectra were obtained with fibres of differing diameter (3 and 1.5 arcsec, respectively). This results in the respective spectra sampling different regions of SDSS J1533+4432 which could influence the obtained spectra. We investigate the potential effect of this difference in fibre size using the MaNGA IFU observation which covers a much larger fraction of SDSS J1533+4432. We obtain synthetic aperture spectra by applying circular apertures of radii matched to both the SDSS Legacy and DESI spectra, centred on the nucleus of SDSS J1533+4432 (spaxel 31, 31) and obtaining a mean of all spaxels that are at least 80 per cent within the aperture region. Following this, we normalize each resultant spectrum and generate a residual by subtracting the smaller aperture (DESI-like) spectrum from the larger (SDSS-like). Using synthetic aperture spectra constructed from the MaNGA IFU observation ensures that no temporal variation is present within the comparison, allowing any aperture size related effects to be fully isolated. This comparison (Fig. 4) reveals that the synthetic aperture spectra are almost identical, with the normalized residual spectrum having a mean absolute difference of 1 per cent. Additionally, neither the [O II] λ3728 Å nor [O III] λ5007 Å emission lines are outliers in the residual spectrum, confirming that their increase in strength between the SDSS Legacy and DESI spectra is the result of true evolution rather than the differing aperture sizes between the observations.

² ATLAS observations were made using two broad-band filters; c (cyan) is approximately equivalent to g + r and o (orange) is roughly r + i.

Table 4. Summary of TDE-ECLEs, CrL-TDEs, and other objects used as comparison objects to AT 2018dyk.

Object	Classification	Data used	References for coronal line classification
SDSS J0748+4712	TDE-ECLE	MIR photometry, SDSS spectrum	Wang et al. (2011, 2012); Yang et al. (2013); Dou et al. (2016); Clark et al. (2024)
SDSS J0952+2143	TDE-ECLE	MIR photometry, SDSS spectrum	Komossa et al. (2008, 2009); Wang et al. (2012); Yang et al. (2013); Dou et al. (2016); Clark et al. (2024)
SDSS J1241+4426	TDE-ECLE	MIR photometry, SDSS spectrum	Wang et al. (2012); Yang et al. (2013); Dou et al. (2016); Clark et al. (2024)
SDSS J1342+0530	TDE-ECLE	MIR photometry, SDSS spectrum	Wang et al. (2012); Yang et al. (2013); Dou et al. (2016); Clark et al. (2024)
SDSS J1350+2916	TDE-ECLE	MIR photometry, SDSS spectrum	Wang et al. (2012); Yang et al. (2013); Dou et al. (2016); Clark et al. (2024)
AT 2017gge	CrL-TDE	MIR photometry, Optical spectra	Onori et al. (2022)
AT 2018gn ¹	CrL-TDE	MIR photometry	Wang et al. (2024)
AT 2018bcb	CrL-TDE	MIR photometry	Neustadt et al. (2020)
AT 2021dms	CrL-TDE ²	MIR photometry	Hinkle et al. (2024)
TDE 2021qth	CrL-TDE	-3	Yao et al. (2023)
AT 2021acak	CrL-TDE ⁴	MIR photometry	Li et al. (2023)
TDE 2022fpx	CrL-TDE	MIR photometry	Koljonen et al. (2024)
TDE 2022upj ⁵	CrL-TDE	MIR photometry	Newsome et al. (2022, 2024)
TDE 2024mvz	CrL-TDE	_6	Shitrit et al. (2024)
SDSS J0113+0937	CrL-TDE	_7	Callow et al. (2025)
AT 2019avd	Multi-epoch CrL-TDE/CrL-AGN 7	MIR photometry	Malyali et al. (2021)
TDE 2019qiz	Multi-epoch CrL-TDE 8	MIR photometry	Short et al. (2023)
AT 2019aalc	Multi-epoch CrL-TDE 9	_	Veres et al. (2024)
TDE 2020vdq	Multi-epoch CrL-TDE? 10	-	Somalwar et al. (2025)
VT J154843.06+220812.6 11	CrL-TDE/CrL-AGN	MIR photometry	Somalwar et al. (2022)
SDSS J0938+1353	AGN-ECLE	SDSS spectrum, MIR photometry	Wang et al. (2012); Yang et al. (2013); Clark et al. (2024)
SDSS J1055+5637	AGN-ECLE	SDSS spectrum, MIR photometry	Wang et al. (2012); Yang et al. (2013); Clark et al. (2024)
TDE 2019azh	NonCrL-TDE	MIR photometry	Faris et al. (2024)
iPTF16bco	CL-LINER	MIR photometry	Frederick et al. (2019)
AT 2018aij (ZTF18aahiqfi) 12	CL-LINER	MIR photometry	Frederick et al. (2019)
AT 2018gkr (ZTF18aaabltn)	CL-LINER	MIR photometry	Frederick et al. (2019)
AT 2018ivp (ZTF18aaidlyq)	CL-LINER	MIR photometry	Frederick et al. (2019)
AT 2018lnh (ZTF18aasszwr)	CL-LINER	MIR photometry	Frederick et al. (2019)
ZTF18aasuray	CL-LINER	MIR photometry	Frederick et al. (2019)

Notes. Has a 'SN' rather than an 'AT' or 'TDE' designation on the TNS due to an initial Type II SN classification by Falco et al. (2018). We refer to it by an 'AT' designation here to avoid confusion.

Further information on each object for which data has been used in this work, including coordinates and redshifts, are given in Table A1.

3.2 Spectral comparisons

Here, we compare AT 2018dyk with other types of transients that exhibit coronal iron lines in their spectra. In these comparisons, the spectra are first rebinned to 2 Å or the dispersion resolution of the comparison spectrum (whichever is larger) to improve the signal-to-noise ratio (SNR). Given the close separation in phase between the two spectra of AT 2018dyk that display coronal lines, we only use the higher quality Keck + LRIS spectrum for this analysis. The spectra used in these comparisons are shown in Fig. 5.

We first compare the Keck spectrum of AT 2018dyk spectrum to the spectral sequence of the CrL-TDE AT 2017gge (Onori et al. 2022). We find good matches – as determined through the use of the Akaike information criterion (AIC; Akaike 1974) – to the spectra of AT 2017gge from 2018 April 8–June 29. The overall spectral shape and coronal line features are very similar, though the Balmer emission features of AT 2017gge are significantly broader. These spectra are from a much later phase in the evolution of AT 2017gge: 218–321 d post optical peak compared to 19 d post-optical peak for

² Final epoch of MIR photometry shows rebrightening in both bands. MIR colour evolution at this epoch remains consistent with previous observations. As such, we treat this object as a single epoch event for the purposes of this analysis. Additional observations are required to determine if this rebrightening is a single-epoch outlier or a longer term trend in evolution.

³ The host galaxy of TDE 2021qth is in very close proximity to another galaxy, making reliable photometric separation at the resolution of WISE very difficult. As such, we exclude it from the photometric comparison given the significant contamination that would result.

⁴ Host galaxy also likely hosts an AGN.

⁵ Now known to display quasi-periodic X-ray eruptions (QPEs) as described by Chakraborty et al. (2025).

⁶ Transient occurred too close to the conclusion of the NEOWISE-R mission for useful inclusion in the MIR analysis.

⁷ Excluded from the MIR comparisons due a poorly constrained time of MIR peak.

⁸ Displays an extended, multipeaked MIR rise. TDE 2019qiz also displays QPEs (Nicholl et al. 2024).

⁹ Two overlapping MIR outbursts. As the transient did not return to MIR quiescence between the outbursts, this object is excluded from the MIR comparisons. This transient occurs within a galaxy hosting an AGN.

¹⁰ Two distinct flaring epochs, with only the first displaying coronal emission. As this is the only such object to show multiple possible TDE-linked outbursts with differing behaviour, we do not directly compare TDE 2020vdq to AT 2018dyk.

¹¹ Referred to as VT J1548 in the remainder of this work. Based on a lack of pre-outburst AGN activity and similarity in MIR evolution to other CrL-TDEs, we treat VT J1548 as a CrL-TDE in our analysis but note its classification uncertainty in upcoming plots.

¹² Recent observations show a potential second MIR outburst.

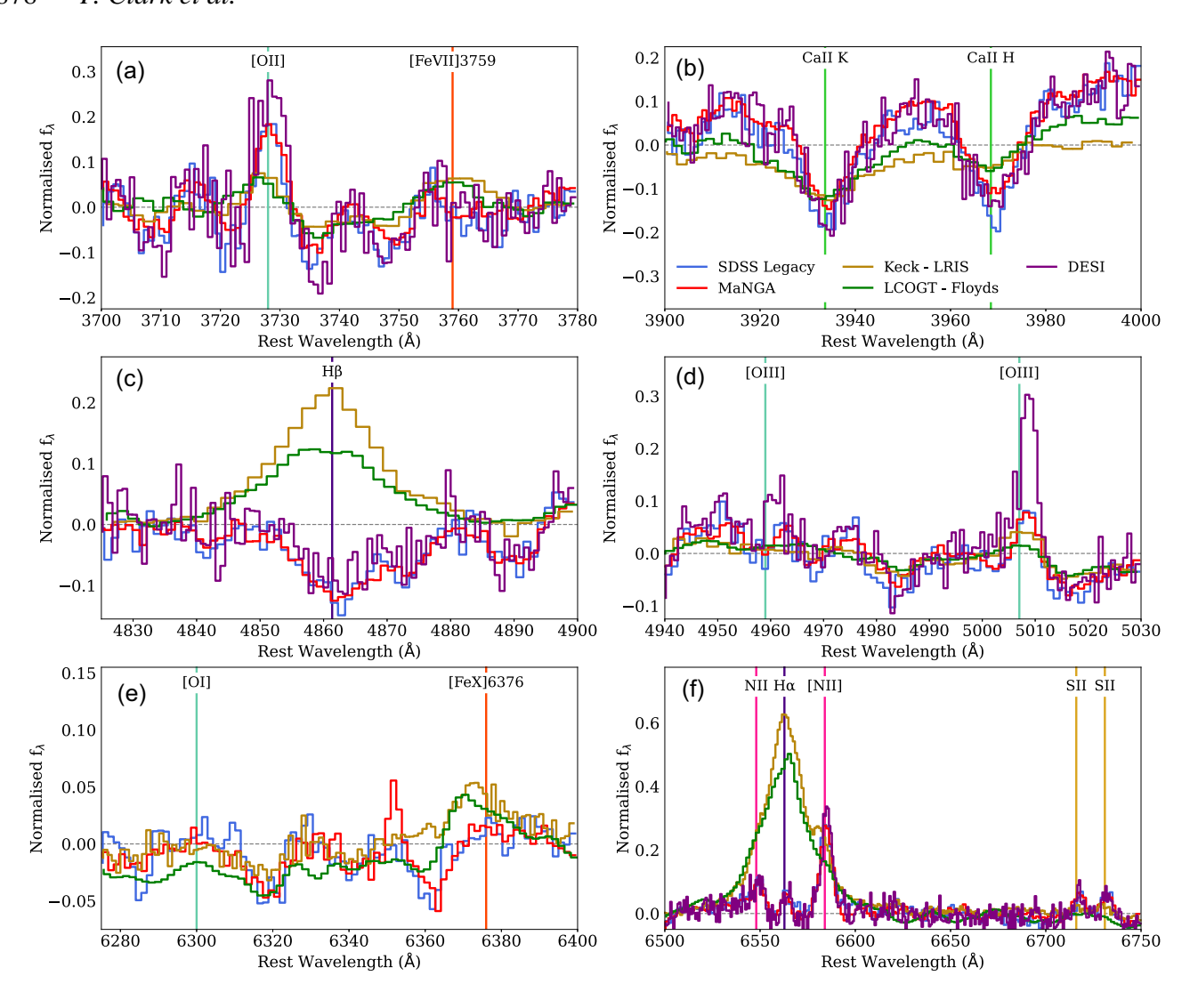


Figure 3. Emission-line evolution of AT 2018dyk across the full range of spectral observations. Spectral normalization and scaling is shared along rows with all spectra first normalized and then scaled to the mean of a local region clear of spectral features: (a) and (b) scaled to the 3650–3700 Å region, (c) and (d) scaled to the 4900–4950 Å region, and (e) and (f) scaled to the 6400–6500 Å region. All selected scaling regions are free from spectral features. Additionally, no rebinning or smoothing has been applied. A dashed horizontal line marking the scaled continuum level is included for reference. (a) Spectral evolution of the [O II] λ3728 Å line region including the weak coronal line [Fe VII] λ3759 Å. The increase in the [O II] λ3728 Å line strength post-outburst relative to spectra obtained both pre and during the outburst is clear. (b) Spectral evolution of the Ca II H&K absorption features. (c) Spectral evolution of the Hβ line region. Transient and broad Hβ emission generated by the TDE is clearly visible. This feature has completely faded away, with the most recent DESI spectrum now matching the pre-outburst SDSS Legacy and local MaNGA spectra. (d) Spectral evolution of the [O III] λ4959 Å and [O III] λ5007 Å lines. Emergence of the [O III] λ4959 Å and the strengthening of the narrow [O III] λ5007 Å emission line in the latest DESI spectrum is observed. This emission, whilst slightly redshifted from the zero velocity position, has not displayed velocity evolution across the available observations (see Fig. 12 and Section 4.1). (e) Spectral evolution of the [O III] λ6300 Å emission feature (which remains undetected at all phases) and the coronal [Fe x] λ6376 Å emission line which is only present in the Keck+LRIS and LCOGT + FLOYDS spectra. The DESI spectrum is excluded from this subplot as its lower SNR would otherwise mask the [Fe x] λ6376 Å feature. As with other regions, the DESI spectrum closely matches the SDSS-Legacy and MaNGA spectra. (f) Spectral evolution of the Hα complex region. As with Hβ

the AT 2018dyk Keck spectrum, highlighting the significant diversity in evolution time-scales of these objects.

As previously discussed, Type IIn SNe have also been observed to display weak Fe coronal line features. For comparison, we examine the spectral sequence of the Type IIn SN 2005ip (Stritzinger et al. 2012).

In Fig. 5, we show the spectrum of SN 2005ip at a phase of +29 d, due to the similar phase and wavelength coverage when compared to the AT 2018dyk Keck spectrum. As expected, the coronal line features of AT 2018dyk are significantly stronger than those of SN

2005ip, with SN 2005ip also lacking the strong He I, He II, and higher order Balmer emission lines present in AT 2018dyk. Additionally, the [Ne III] and [Ne V] emission lines at wavelengths $<4000\ \mbox{\normalfont\AA}$ displayed by AT 2018dyk are not observed in SN 2005ip. Finally, whilst AT 2018dyk does have a broad H\$\alpha\$ emission component at this phase of evolution, the equivalent emission in SN 2005ip is much stronger and broader overall.

Following these single object comparisons, we also compare AT 2018dyk to the TDE-ECLE and AGN-ECLE templates constructed by Clark et al. (2024), though due to observational

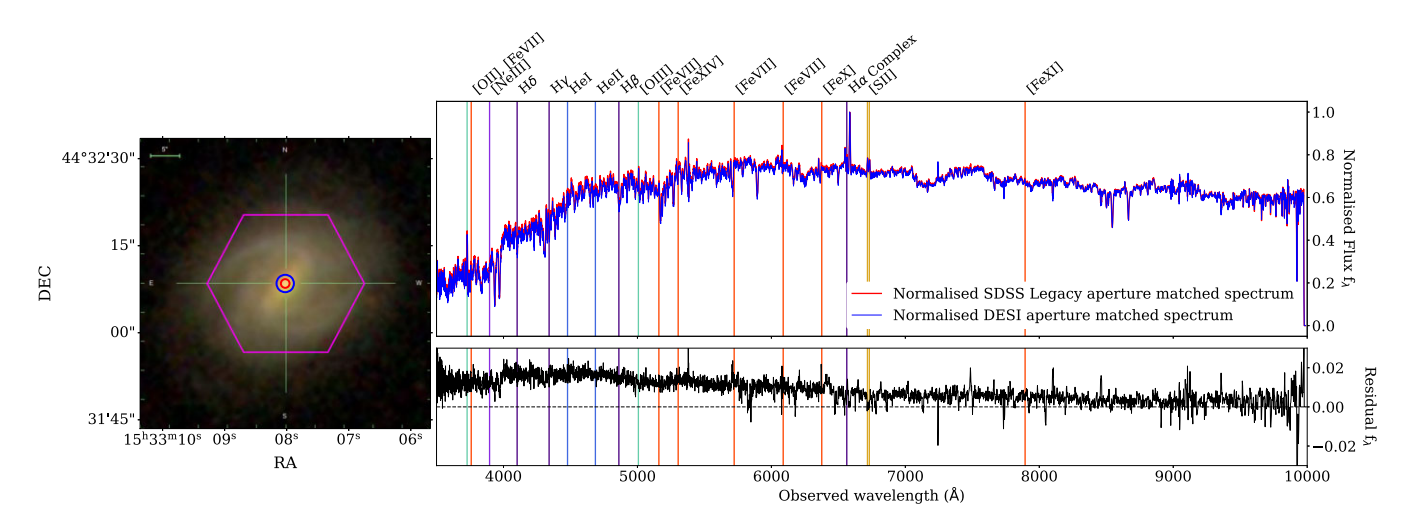


Figure 4. Comparison between the synthetic aperture spectra generated from the MaNGA observation and configured to match the fibre sizes of the SDSS Legacy survey and DESI observation. The overall extent of the MaNGA data is shown by the outer purple hexagon, with the regions used to construct the synthetic apertures shown by circles with colours that match those used for the spectra. The inner DESI matched aperture has a diameter of 1.5 arcsec, with the outer SDSS Legacy matched aperture having a diameter of 3 arcsec. The choice to use synthetic aperture spectra here rather than a direct comparison is made to isolate any temporal variation from the comparison and highlight any potential aperture effect. No significant differences are observed, with a mean absolute difference of 1 per cent, confirming that the changes observed between the SDSS and DESI spectra are not the result of aperture size and reflect the residual physical effects of AT 2018dyk. The aperture spectra presented here have been de-redshifted and corrected for Milky-Way extinction, but have not undergone any smoothing for this comparison.

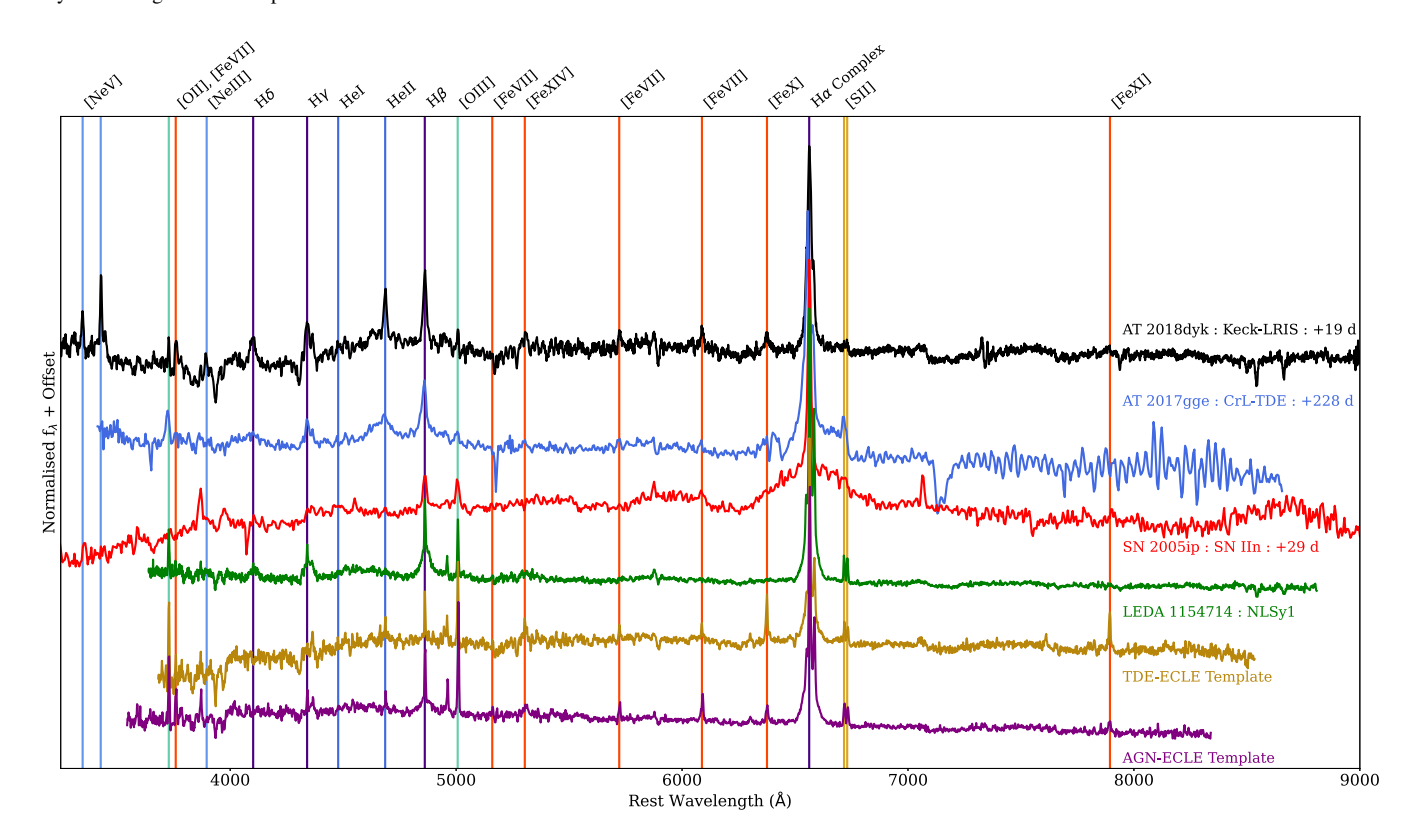


Figure 5. Comparison between the Keck + LRIS spectrum (obtained 19 d following optical peak) to a range of comparison objects. The AT 2018dyk spectrum shows similar coronal line features as those seen in the CrL-TDE AT 2017gge and in the ECLE templates (composite spectra obtained by combining the SDSS Legacy spectral observations of the sample) from Clark et al. (2024), though at lower relative strength than the ECLE templates. The broad TDE features of H, He I, and He II are also shown by both AT 2018dyk and AT 2017gge. The spectrum of AT 2017gge is from a later phase relative to maximum light compared to AT 2018dyk as the coronal line features of AT 2017gge developed \sim 200 d post-maximum light (as opposed to the near maximum light line emergence in AT 2018dyk). Such features are absent from the TDE-ECLE template as this is composed of spectra at much later relative phases (several years). The Type IIN SN 2005ip displays coronal emission at a much lower intensity than AT 2018dyk and the rest of the comparison sample. It also has a much broader H α emission component, but lacks the He I, He II, Hγ, and Hδ emission lines.

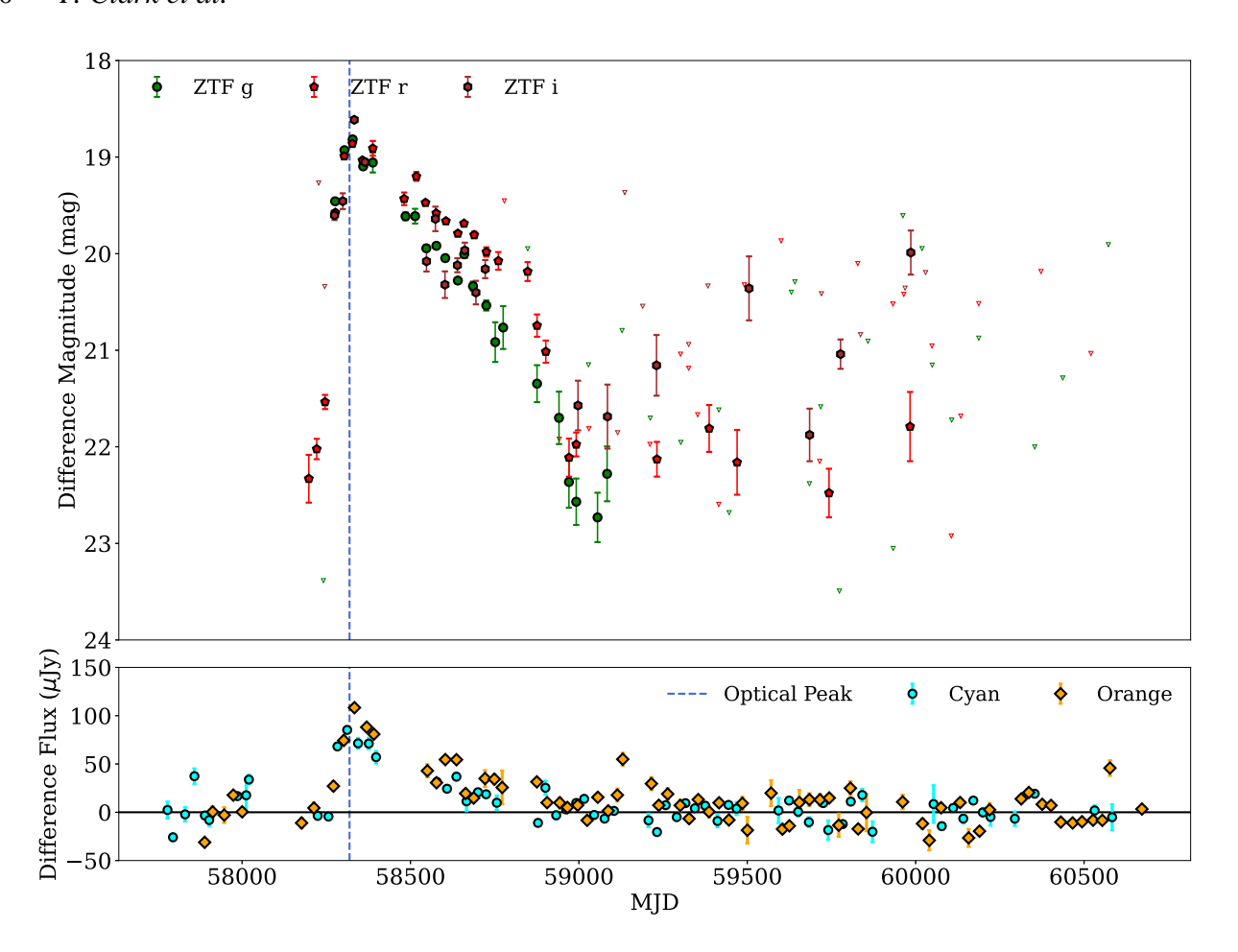


Figure 6. Top: ZTF forced photometry difference light curves for AT 2018dyk. Upper limits for non-detections are shown by empty triangles. Late time detections are likely spurious as evidenced by their erratic nature and deeper proximal upper detection limits. Bottom: ATLAS difference light curves for AT 2018dyk. For both data sources, observations in each band have been stacked to obtain a 30 d cadence and are displayed following the trimming of unreliable observations. The time of optical peak observed in ZTF photometry (as detailed by Huang et al. 2023) is shown for reference by the dashed blue line. As some flux from AT 2018dyk is present in the reference ranges used by the forced photometry systems of both telescopes, all observations have been rescaled based on the per-band mean difference flux of observations made at MJDs > 59500. ATLAS observations are shown in flux rather than magnitude space due to the lower overall SNR of the observations. In both data sets, AT 2018dyk is clearly a single-epoch, non repeating event.

limitations, these represent a much later phase in the evolution of these objects. These template spectra were constructed by averaging the SDSS Legacy spectra of the TDE-ECLE and AGN-ECLEs originally identified in the search of SDSS DR7 by Wang et al. (2012).

Whilst similar in overall spectral shape, the Fe coronal emission lines exhibited by AT 2018dyk are weaker than those displayed in either ECLE template. However, both AT 2018dyk and the TDE-ECLE template lack the strong [O III] emission typical of AGN activity. The comparative weakness of, the coronal emission features of AT 2018dyk when compared to the existing TDE-ELCE sample is explored in the context of its MIR behaviour in Section 3.4.

3.3 Search for additional transient outburst activity

As stated in previous works, AT 2018dyk was visible in optical photometric observations with a rapid rise and decline consistent with a power law with a best-fitting index of -1.58 (Huang et al. 2023). We use recent ZTF and ATLAS observations to investigate whether any additional flares occurred since 2018, which could point to AT 2018dyk resulting from recurrent AGN flaring. The resulting

multifilter light curves generated from forced photometry are shown in Fig. 6. No flaring activity has been observed in the ~ 2000 d since the transient returned to quiescent optical flux, with a stable flux level observed following the singular outburst and decline. There have also been no new reports of transient activity at the location of AT 2018dyk or elsewhere within its host galaxy.

3.4 MIR photometric evolution

3.4.1 Light-curve analysis

The MIR evolution of TDEs (and AGNs) reveals the presence of circumnuclear material in the region around the SMBH. Higher energy photons are absorbed by this material, reprocessed, and re-radiated in the MIR with the luminosity of this MIR, emission directly linked to the incoming flux. As such, where circumnuclear material is present in sufficient quantities and in a suitable physical configuration, a TDE is expected to generate an MIR outburst (delayed from the peak of the direct emission from the disruption itself due to distance between the SMBH and surrounding material) which will then fade as the higher energy emission from the TDE also fades and thus provides less incident radiation for reprocessing.

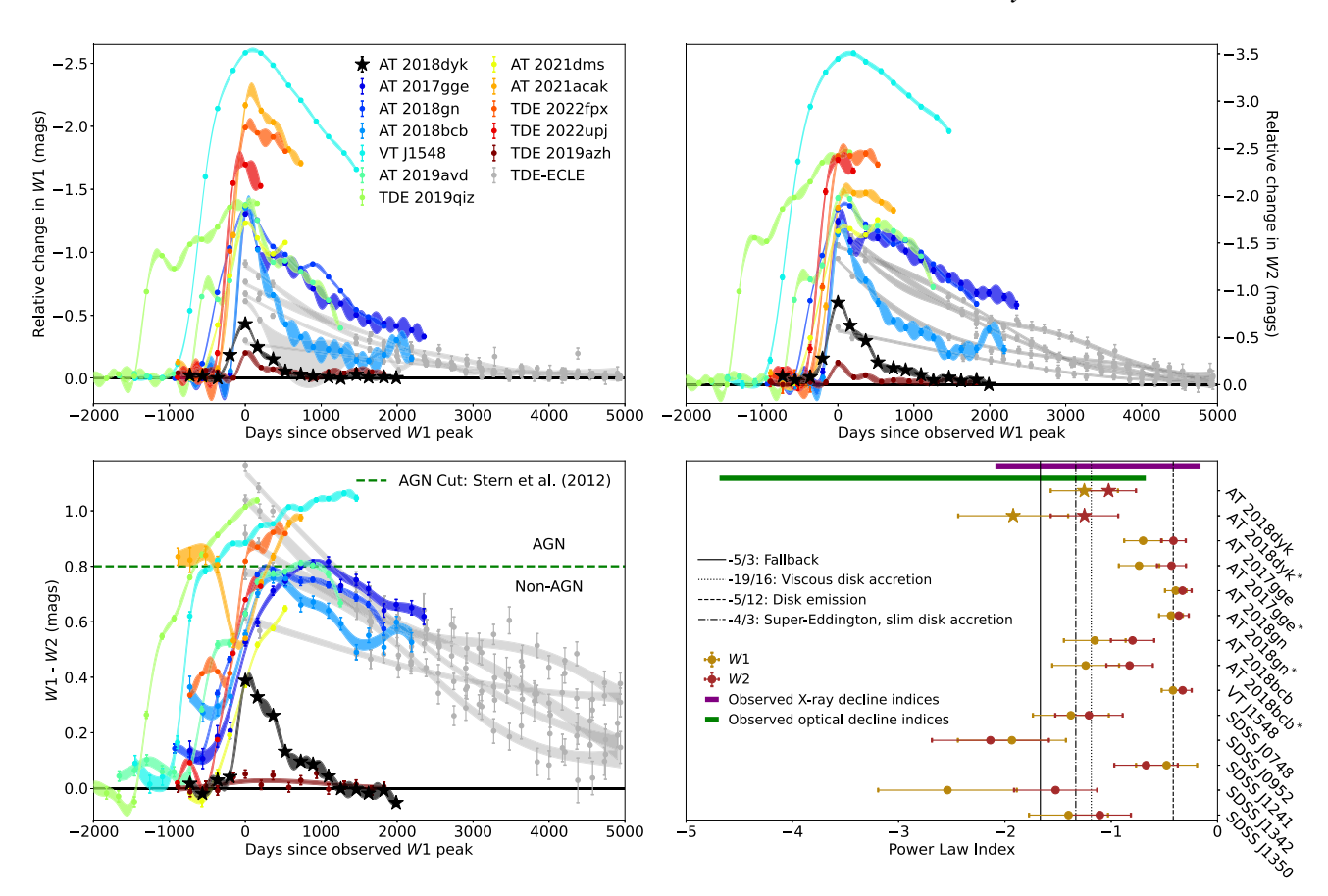


Figure 7. Top left: relative change in W1 compared to observed W1 peak. Top right: relative change in W2 compared to observed W2 peak. Bottom left: W1-W2 colour evolution. The dashed horizontal line shown is the AGN/non-AGN dividing line from Stern et al. (2012). Objects with a W1-W2 colour greater than this value display AGN-like behaviour. In all panels, fits displayed are obtained through Gaussian processes, with the shaded regions indicating the 1σ fitting uncertainties. Bottom right: comparison between the MIR power-law decline indices for AT 2018dyk, the TDE-linked ECLEs (Clark et al. 2024), and the coronal line TDEs AT 2017gge and AT 2018bcb, along with the range of X-ray power-law decline indices determined from the Auchettl, Guillochon & Ramirez-Ruiz (2017) TDE sample (purple shading), and the optical decline indices of the Hammerstein et al. (2023a) TDE sample (green shading). Vertical lines indicate the expected values for a range of accretion models.

In contrast, as AGNs are not single epoch events, but rather variable objects, their MIR emission is expected to show smaller amplitude but repeated variation as their overall energy output varies. Colour evolution is produced by varied strengthening of specific spectral emission features, with AGN seen to be redder than quiescent galaxies in W1-W2 colour space.

As described by Huang et al. (2023) and Masterson et al. (2024), prior to the observed outburst the MIR luminosity of the host galaxy of AT 2018dyk was largely constant in both W1 and W2, with the exception of low-level stochastic variability. Specifically, the standard deviation of the NEOWISE observations prior to outburst was 0.01 mag in both W1 and W2, while standard deviations of 0.01 mag in W1 and 0.03 mag in W2 were measured after the end of the outburst. This is in good agreement with the pre-outburst level of variability observed in the CrL-TDE sample, which averaged 0.03 mag in W1 and 0.05 mag in W2. It is also lower than the variability displayed by either the AGN-ECLEs or CL-LINERs, with mean standard deviations of 0.08 and 0.15 mag in W1 and 0.09 and 0.20 mag in W2, respectively. Additionally, the overall maximum changes in pre-outburst magnitude for AT 2018dyk and the other Crl-TDEs are also smaller (0.04 and 0.11 mag in W1 and 0.03 and 0.17 mag in W2, respectively) compared to the variability displayed by AGN-ECLEs or CL-LINERs (0.33 and 0.49 mag in W1 and

0.36 and 0.62 mag in *W*2, respectively). This serves to highlight that AT 2018dyk and the other CrL-TDEs display pre-outburst MIR variability at a lower level than observed in otherwise potentially contaminating AGN. A full detailing of this variability analysis can be found in Appendix Tables B1 and B2.

We extend previous light-curve analyses to include the most recent NEOWISE data release, which shows that AT 2018dyk has now returned to its pre-outburst quiescent brightness in both W1 and W2 (Fig. 7). The observed emission peaked on 2019 January 20 (MJD 58503) with an apparent delay of \sim 180 d with respect to the optical peak (approximately coincident with the observed peak of X-ray emission). However, given the lower cadence of WISE observations (\sim 6 months) relative to the optical observations, the true MIR peak was likely brighter than what is captured by the available observations.

Prior to outburst, the W1-W2 colour of AT 2018dyk was close to 0 mag, well below the Stern et al. (2012) AGN colour cut of W1-W2>0.8 mag. The W1-W2 colour of AT 2018dyk changes significantly with the onset of the MIR flare and reaches a peak value of 0.4 mag, coincident with peak MIR luminosity, before returning to its original colour over the next ~ 1000 d. Additionally, at no point during its evolution does AT 2018dyk meet the (Assef et al. 2018) W1-W2 versus W2 classification for AGN activity, at either the 90 per cent or

50 per cent confidence levels. Further observations will be required to confirm that AT 2018dyk has returned to a long-term stable post-outburst flux (i.e., that no additional outbursts occur). However, both the lack of pre-outburst AGN activity and the return to quiescent behaviour following the end of the outburst are consistent with the absence of any significant AGN activity prior to, or following the end of the outburst.

When compared to the TDE-ECLEs and CrL-TDEs, the MIR evolution of AT 2018dyk shows the same overall behaviour, though has some notable distinctions. The variability displayed by AT 2018dyk has a smaller amplitude (both in the individual MIR bands and in the W1-W2 colour) and a shorter duration. For example, whilst AT 2018dyk returned to MIR quiescence ~ 3.5 yr following outburst, several TDE-ECLEs are still in their decline phase more than 20 yr following their initial outburst. Additionally, whilst the beginning of the ECLE MIR outbursts were not observed (as the outbursts pre-date the start of WISE observations), they all initially had W1-W2 colours at or above the Stern et al. (2012) 0.8 mag AGN colour cut; AT 2018dyk, however, remains much bluer than this cut at all stages of its evolution, though it does trend towards it during outburst.

We investigate whether the MIR post-outburst behaviour of AT 2018dyk can be modelled using a power-law decline in a similar manner as TDE-ECLEs. Following Dou et al. (2016) and Clark et al. (2024), we fit both the W1 and W2 bands separately in flux space and compare to the other objects in the comparison sample (lower right of Fig. 7). Given the low cadence of the WISE observations, for the purposes of the power-law fitting we assume that true peak MIR luminosity occurred 100 d prior to the observed peak for AT 2018dyk and the other CrL-TDEs (i.e., at approximately half the time between the observed peak and the prior observation), whilst adopting the peak times of the TDE-ECLEs used by Dou et al. (2016) and Clark et al. (2024). We note here that the time of peak luminosity and the power-law index are highly degenerate, with tests showing that changing the peak date by 50 d produces a change of \sim 23 per cent in the determined values of the power-law indices. Due to the cadence of WISE observations, the true time of peak cannot be constrained further, and we include a 25 per cent statistical uncertainty for the power-law index values plotted in Fig. 7. This statistical uncertainty is not included in the reporting of the direct fitting results within the following text or in Appendix B2, which detail the values obtained directly from the fitting.

Additionally, unlike in previous analyses (Dou et al. 2016; Clark et al. 2024), we are able to constrain the expected quiescent flux of the underlying galaxies of AT 2018dyk and the comparison CrL-TDEs using the available pre-outburst photometry by setting the floor of the power-law fit to reflect this baseline flux. This was not possible for studies into the TDE-ECLEs as pre-outburst MIR observations for these objects do not exist.

For AT 2018dyk, there are notable early flux excesses immediately following peak in both MIR bands (also observable in the light curves as noticeable shoulders). When these excesses are removed the overall fits to the remaining photometry (as determined by an AIC comparison) are significantly improved. This is the first time such features have been identified in the light curves of CrL-TDEs, with the presence of such excesses are indications of multiple emission components likely produced by complex dust configurations. Whilst deconvolving these components and modelling of their corresponding physical configurations is beyond the scope of this work, we report the results of the power-law fits with and without excluding these early data points. The full results of these fits are given in Table B2 and the lower right panel of Fig. 7.

When including all post-peak data, the measured power-law indices for AT 2018dyk are -1.25 ± 0.04 in W1 and -1.02 ± 0.03 in W2. When the two observations comprising the excess are excluded, the overall fit to both the early peak and late-time decline tails are improved, particularly for the W2 band with decline indices of -1.92 ± 0.19 and -1.25 ± 0.05 for W1 and W2, respectively.

For comparison, we perform the same fitting procedure on the existing sample of TDE-ECLEs, updating the work of Clark et al. (2024) to include the data from the latest NEOWISE-R release, whilst also performing new fits on the CrL-TDE sample.

As only a fraction of the CrL-TDEs have passed their MIR peaks and are now declining, we only fit AT 2017gge, AT 2018gn, AT 2018bcb, and VT J1548, which all have at least five observations following their MIR peaks. Additionally, we do not include AT 2019avd in this comparison due to its differing overall multiepoch MIR behaviour, despite now being in an established decline phase. The resultant power-law indices are compared to a range of models of different types of SMBH accretion: standard fallback (e.g., Evans & Kochanek 1989; Phinney 1989), viscous disc accretion (Cannizzo, Lee & Goodman 1990), disc emission (Lodato & Rossi 2011), and advective super-Eddington thin-disc accretion (Cannizzo & Gehrels 2009; Cannizzo, Troja & Lodato 2011). As with AT 2018dyk, AT 2017gge, AT 2018gn, and AT 2018bcb show evidence of complex circumnuclear dust configurations with post-peak excesses/light-curve shoulders in both WISE bands, as such we report the fitting results including and excluding these excesses (Table B2). For these objects, a visual inspection of the light-curves indicates that fits to both bands are improved when the excesses are removed, with an AIC comparison confirming this for AT 2018bcb. However, retaining the excesses for AT 2017gge and AT 2018gn is statistically preferred. The resulting power-law indices for all objects are found within the parameter space consistent with other previous works, with the range of index values spanning -2.51 to -0.42 in W1 and -1.97 to -0.32 in W2.

The results of the fitting excluding these excesses are shown in full in Fig. B1, with the corresponding fits removing the early excesses shown in Fig. B2.

Earlier AllWISE photometry includes the longer wavelength W3 filter, though only for two epochs, both obtained well before the outbursts of any of the objects explored in this work. This can be used to better differentiate between various galaxy types or AGN activity, obscured or otherwise. We present these data in Fig. 8 for AT 2018dyk and for selected comparison objects, including the original TDE-ECLE sample and other CrL-TDEs. In this parameter space, AT 2018dyk sits well within the region occupied by starforming galaxies and is outside the 'Mateos wedge' of AGN-hosting galaxies (Mateos et al. 2012) and other regions that would indicate the presence of an obscured AGN. This is similar to other optically selected CrL-TDEs (excluding AT 2021acak, which occupies the edge of several different AGN regions, attributed to its host galaxy also possessing an AGN, as described by Li et al. 2023), but distinct from the original TDE-ECLE sample, which were observed by the AllWISE survey during their MIR outburst phase and display colours consistent with AGNs (Fig. 8). As TDE-ECLEs and CrL-TDEs are subpopulations of the same underlying group, whilst, the AllWISE observations are limited in time, they provide a general view of their behaviour, i.e., quiescent prior to outburst and AGN-like during outburst. No object within the sample has AllWISE observations post the end of their outbursts, but given the return to quiescence in both W1 and W2 bands, it is reasonable to conclude a similar behaviour in the W3 band, though any potential differences in time-scale are of course unobserved.

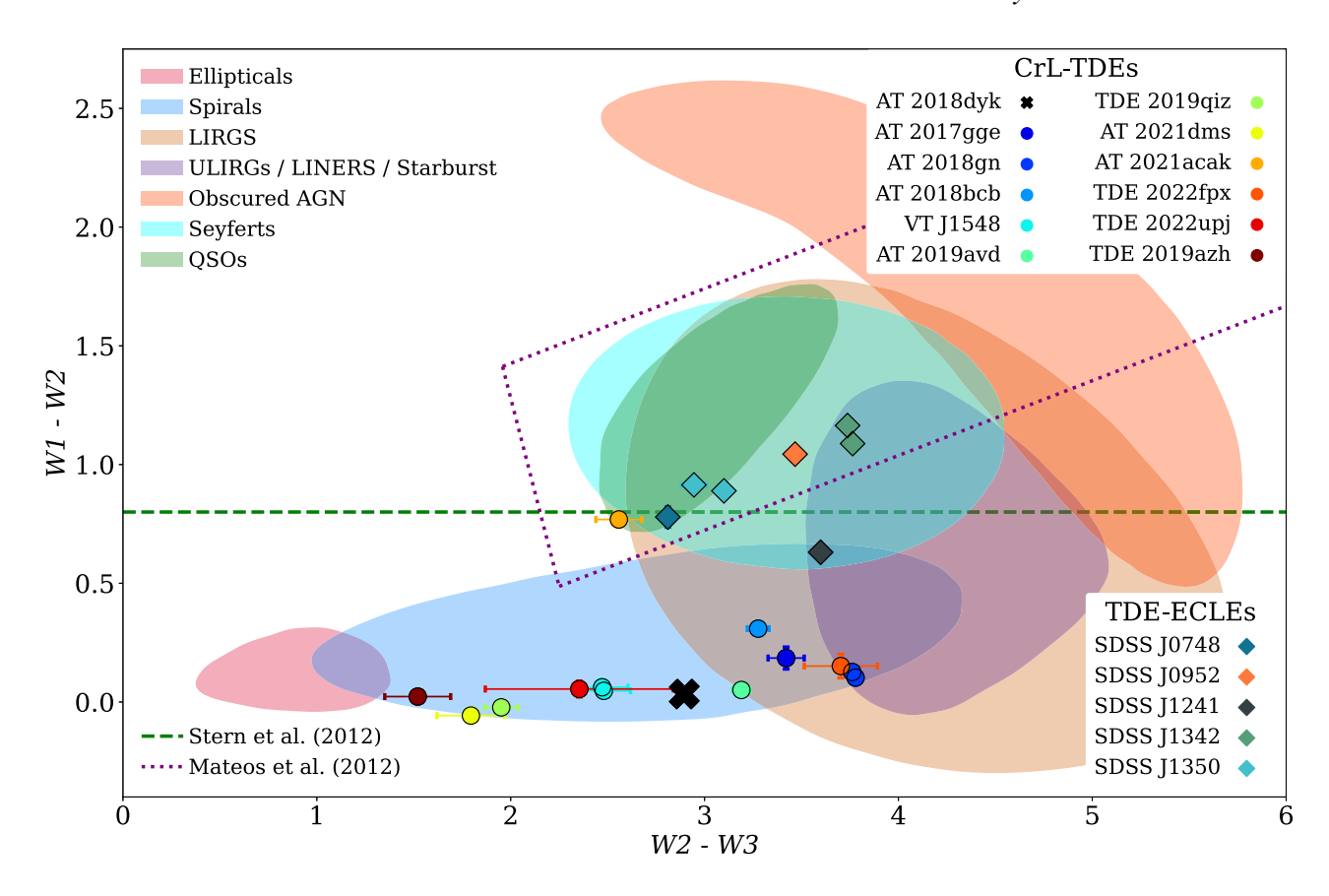


Figure 8. AllWISE colour–colour plot showing AT 2018dyk (black cross) in comparison to the known sample of TDE-ECLEs (diamonds) and CrL-TDEs (circles). Whilst two epochs of data are included for AT 2018dyk, they overlap due to the lack of variability during this time. Regions have been sourced from Wright et al. (2010). The AGN identification cuts from Stern et al. (2012) and Mateos et al. (2012) are included as a green dashed line and purple dotted lines, respectively. Additionally, we note that NLSy1 AGNs occupy the same region of parameter space as more conventional Seyfert galaxies, as shown by Paliya et al. (2024). AT 2018dyk and the other CrL-TDEs that were observed in their pre-TDE quiescent state occupy the parameter space of spiral/star-forming galaxies and are outside the regions that would indicate any AGN activity, with the exception of AT 2021acak, which is hosted by a galaxy that also hosts an AGN. In contrast, the SDSS TDE-ECLEs—observed by AllWISE during outburst—are found within or close to the AGN regions. We remind the reader that these classes of objects likely represent the same underlying population observed at different phases in their evolution. Uncertainties in both axes are included but are generally smaller than the points.

3.4.2 Outburst properties

We also measure the maximum difference between outburst peak and pre-outburst quiescence (Δ values) for both MIR bands and colour. For AT 2018dyk, these values are $\Delta W1 = 0.40 \pm 0.01$ mag, $\Delta W2 = 0.79 \pm 0.01$ mag, and $\Delta (W1 - W2) = 0.39 \pm 0.01$ mag.

For comparison, we measure the equivalent values for the other objects within the comparison sample, treating these as lower limits for those objects that are still rising. Additionally, as the quiescent states of the TDE-ECLEs were not observed in the MIR, lower limits on the magnitude of the outbursts are obtained using the observed differences in magnitudes between the first and faintest observations. We note here that as values are measured independently, they do not necessarily occur at the same MJD, especially when comparing the maximum change in colour, which can lag the peak MIR luminosity by several years (see the lower left panel of Fig. 7). We detail the full results of these calculations for all objects in the comparison sample within Table 5 and Fig. 9, grouped by object classification. We now highlight the results from this analysis.

All other members of the CL-LINER class described by Frederick et al. (2019), with the exception of AT 2018gkr, display $\Delta W1$ and $\Delta W2$ at close to a one-to-one ratio, with all having maximum brightening in both bands of less than 1 mag. This behaviour is shared by the AGN-ECLEs and the non-CrL TDE 2019azh. These

objects also display small $\Delta(W1 - W2)$ values of less than 0.2 mag. The exception to this general behaviour is AT 2018gkr, which has displayed a long-term rise in luminosity in both *WISE* bands since the start of observations, though preferentially brightening in W2.

In contrast, all observed CrL-TDEs (including AT 2018dyk) and TDE-ECLEs display outbursts that are brighter in W2 than W1. Additionally, whilst there is no apparent relation between the overall change in brightness and the colour of the outburst for the CLLINERs and AGN-ECLEs, a trend is apparent for the CrL-TDEs and TDE-ECLEs with the brighter the outburst, the redder its peak change in colour (see the left panel of Fig. 9). We further discuss these results and the behaviour of the CrL-TDE sample as a whole in Section 4.2.

3.5 Host-galaxy analysis

With both the spectroscopic and photometric behaviour of AT 2018dyk consistent with that of a CrL-TDE, we now explore the properties of its host galaxy (SDSS J1533+4432) on both global and local scales to determine if it is consistent with the wider TDE host galaxy population. We note than in this section, uncertainties quoted are determined directly from observations and do not include any scatter inherent in scaling relations used.

Table 5. Peak changes in absolute magnitude and colour of the MIR outbursts displayed by AT 2018dyk and objects of interest from the literature.

Object	$\Delta W1$	$\Delta W2$	$\Delta(W1-W2)$
AT 2018dyk	-0.40 ± 0.01	-0.79 ± 0.01	0.39 ± 0.01
CrL-TDEs			
AT 2017gge	-1.29 ± 0.01	-1.66 ± 0.02	0.66 ± 0.02
AT 2018gn	-1.34 ± 0.01	-1.90 ± 0.01	0.68 ± 0.02
AT 2018bcb	-1.30 ± 0.01	-1.57 ± 0.01	0.47 ± 0.02
AT 2021dms	-1.21 ± 0.01	< -1.75	> 0.69
AT 2021acak ¹	-2.13 ± 0.01	-2.01 ± 0.01	> 0.15
TDE 2022fpx	-1.89 ± 0.01	-2.38 ± 0.02	0.57 ± 0.02
TDE 2022upj	-1.67 ± 0.01	-2.30 ± 0.01	> 0.68
Multi-epoch CrL-TDEs			
AT 2019avd	-1.36 ± 0.01	-1.92 ± 0.01	0.74 ± 0.01
TDE 2019qiz	< -1.35	< -2.42	> 1.07
Uncertain CrL-TDEs/AGNs			
VT J154843.06+220812.6	-2.57 ± 0.01	-3.47 ± 0.01	1.01 ± 0.01
TDE-ECLEs			
SDSS J0748+4712	< -0.77	< -1.48	> 0.73
SDSS J0952+2143	< -0.61	< -1.33	> 0.73
SDSS J1241+4426	< -0.30	< -0.61	> 0.35
SDSS J1342+0530	< -0.67	< -1.80	> 1.14
SDSS J1350+2916	< -0.91	< -1.70	> 0.89
AGN-ECLEs			
SDSS J0938+1353 ²	-0.09 ± 0.02	-0.11 ± 0.07	0.03 ± 0.01
SDSS J1055+5637 ²	-0.52 ± 0.02	-0.54 ± 0.03	0.08 ± 0.02
NonCrL-TDEs			
TDE 2019azh	-0.16 ± 0.01	-0.20 ± 0.01	0.05 ± 0.02
CL-LINERs			
iPTF16bco ³	-0.22 ± 0.01	-0.27 ± 0.01	0.14 ± 0.02
AT 2018aij ⁴	-0.30 ± 0.01	-0.38 ± 0.01	0.16 ± 0.01
AT 2018gkr ²	-0.61 ± 0.01	-0.98 ± 0.02	0.55 ± 0.01
AT 2018ivp	-0.54 ± 0.01	-0.60 ± 0.02	0.08 ± 0.02
AT 2018lnh ³	-0.35 ± 0.01	-0.36 ± 0.01	> 0.16
ZTF18aasuray	-0.71 ± 0.01	0.89 ± 0.01	0.20 ± 0.01

Notes. In all cases, values for each band and the overall observed peak colour change are determined independently and do not necessarily occur at the same phase.

3.5.1 Global properties

We retrieve photometrically determined global host galaxy properties for SDSS J1533+4432 from the MaNGA Visual Morphology Catalogue (Vázquez-Mata et al. 2022), the GALEX-SDSS-WISE Legacy Catalog (GSWLC-2; Salim et al. 2016; Salim et al. 2018), the MaNGA PyMorph DR17 photometric catalogue (MPP-VAC-DR17; Fischer et al. 2019; Domínguez Sánchez et al. 2022), and the NASA Sloan Atlas (NSA).⁵ The retrieved properties are summarized in Table 6. Given their specific configuration for galaxies observed by MaNGA and the inclusion of uncertainties, where a parameter has been measured in multiple catalogues, we prefer the values included in GSWLC-2 and MPP-VAC-DR17.

To determine if the global galaxy properties of SDSS J1533+4432 are consistent with other TDE host galaxies, we explore a range of properties, comparing each in turn to existing samples of optically selected TDE host galaxies from Law-Smith et al. (2017), Graur et al. (2018), and Hammerstein et al. (2023b). Furthermore, we investigate the local properties of the region in which AT 2018dyk occurred in more depth in Section 3.5.2.

We find that the stellar mass of SDSS J1533+4432 is consistent with, though is at the high end of measured TDE host galaxy masses, with a GSWLC-2 mass of 11.02 \pm 0.02 $\log_{10}(M_{\odot} yr^{-1})$. For comparison, Law-Smith et al. (2017) found a TDE host galaxy mass range of 9.2–10.4 $\log_{10}(M_{\odot})$, similar to the Graur et al. (2018) range of 8.5–11.0 $\log_{10}(M_{\odot})$ and the Hammerstein et al. (2023b) range of 9.49–11.23 $\log_{10}(M_{\odot})$.

We also examined whether the Sérsic profile of SDSS J1533+4432 is consistent with the previously described TDE host samples. Taking a weighted mean of the per-band Sérsic indices from

¹ Host galaxy also likely hosts an AGN.

² These objects have not displayed specific outbursts, with these values describing their level of general variability instead.

³ MIR outburst occurred significantly after initial behavioural change and classification (i.e., years later).

⁴ Recent observations show re-brightening in both W1 and W2 bands and a reddening of W1-W2 colour. Values quoted are based on photometry obtained prior to the start of the rebrightening phase.

⁵In this work we make use of v1_0_1 of the NSA accessible here: https://www.sdss4.org/dr17/manga/manga-target-selection/nsa/

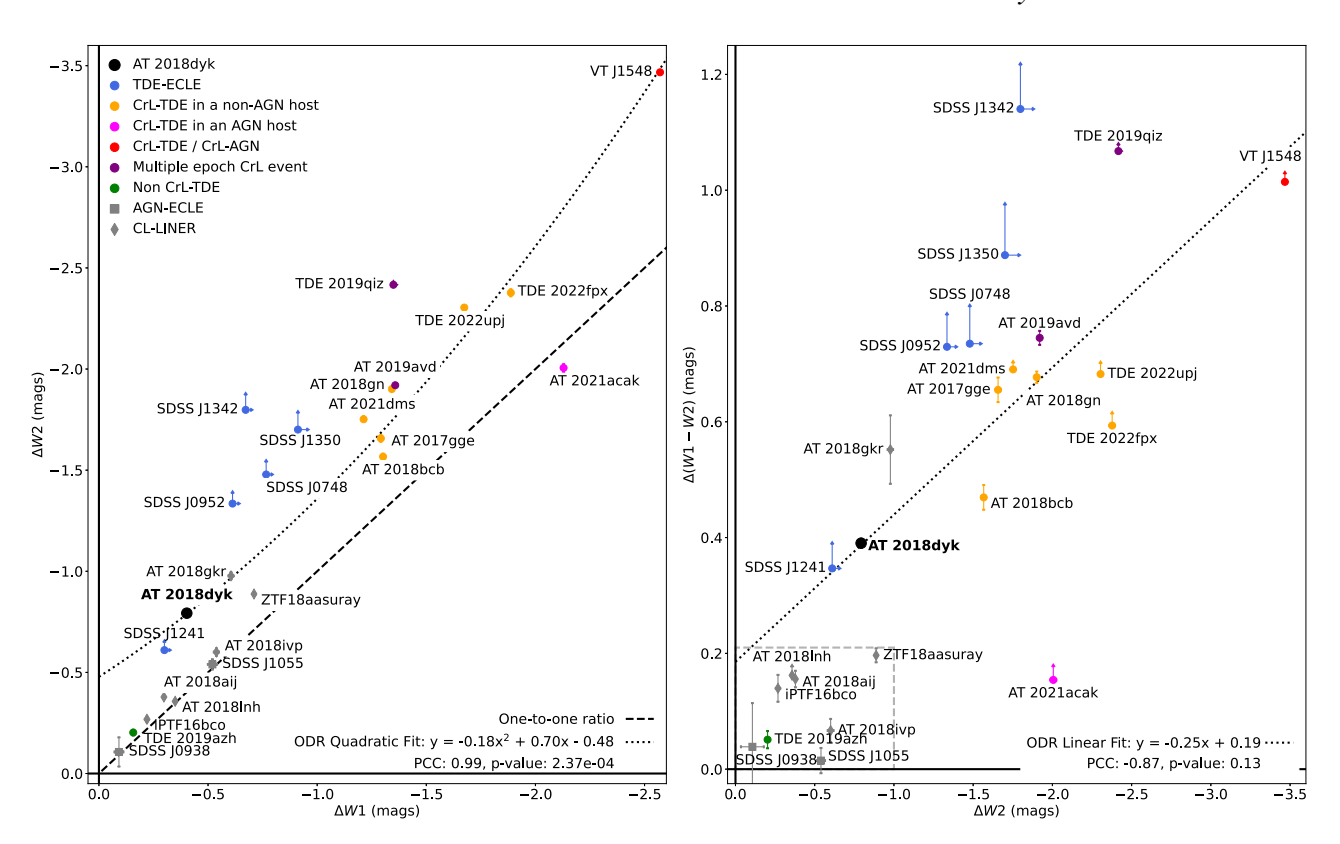


Figure 9. Left: comparison between the maximum change in W1 and W2 between AT 2018dyk (black circle) and a range of comparison objects. Dashed black line shows a 1-to-1 relation. Dotted line shows the orthogonal distance regression (ODR) best-fitting quadratic for the CL-TDEs excluding objects with only upper limits. A quadratic fit to the data was preferred at $a > 5\sigma$ level when tested against a constant and a linear fit using a likelihood ratio test, supported through AIC comparisons. A strong positive correlation is also supported by the Pearson's correlation coefficient with a value of 0.99 and corresponding p-value of 2.4 \times 10⁻⁴. Right: comparison between the maximum change in W1 - W2 colour versus maximum change in W2 brightness. A trend is visible in the behaviour of the CrL-TDEs and TDE-ECLEs with those objects with brighter MIR outbursts (larger $\Delta W2$ values) also showing larger shifts to MIR redder colours. Dotted line shows the ODR linear fit for this trend after excluding objects that only have upper limits on either variable. The small number of data points available for fitting (4) prevents the statistical confirmation of this trend as seen in the high value of the Pearson's correlation p-value of 0.13. The region of parameter space occupied by the CL-LINERs and AGN-ECLEs (excluding AT 2018gkr) is demarcated by the dashed grey box.

MPP-VAC-DR17 pure Sérsic fits, we find a mean index $n = 2.20 \pm 0.01$, consistent within 1.5σ of the median measured by Law-Smith et al. (2017) (4.03 $^{+0.92}_{-1.55}$) and close to the median of the Hammerstein et al. (2023b) sample (1.87).

Next, we explored the stellar surface mass density of SDSS J1533+4432 measured using the Sérsic half-light radius. We find a value from GSWLC-2 of $8.46 \pm 0.02 \log_{10}(M_{\odot} kpc^{-2})$, which is also consistent with the values measured for the Hammerstein et al. (2023b) sample but lower than the average stellar surface mass density of the TDE host galaxies in the Graur et al. (2018) sample. Law-Smith et al. (2017) and Hammerstein et al. (2023b) find that TDE host galaxies are more centrally concentrated than the general galaxy population, with this attributed to TDEs being more likely to occur in galaxies that have experienced a recent merger event (Graur et al. 2018). Similarly, while the density of the passive TDE host galaxies in the Graur et al. (2018) sample was consistent with the general population of passive galaxies (PGs) in SDSS, the starforming host galaxies were significantly denser than the general star-forming galaxy population.

Finally, using the stellar mass and star formation rate measurements from GSWLC-2, we calculate the specific star formation rate (sSFR) of SDSS J1533+4432 to be $-10.97 \pm 0.13 \log_{10}(yr^{-1})$. This value falls within the 'green valley' of galaxies thought to be transitioning between star-forming and quenched states. Salim

(2014) defines this region as:

$$-11.8 \ge sSFR(\log_{10}) \ge -10.8 \tag{1}$$

The lower values for stellar mass from the NSA when using either Sérsic or Petrosian photometry (10.68 \pm 0.04 and 10.56 \pm 0.04 $\log_{10}(M_{\odot})$, respectively), correspond to higher overall sSFRs of -10.62 ± 0.13 and $-10.51 \pm 0.13 \, \log_{10} \, (yr^{-1})$. These place SDSS J1533+4432 slightly outside the high sSFR limit of the green valley, though both estimates are $<\!3\sigma$ of the upper boundary.

All the measured sSFRs are within the low star formation tail of the observed sample of MaNGA galaxies with spiral morphologies (see e.g., fig. 1 of Biswas & Wadadekar 2024). Hammerstein et al. (2023b) found that TDE hosts were preferentially hosted by galaxies within or close to the green valley (63 per ecnt of their TDE host sample were green valley galaxies when classified using rest-frame u-r colours compared to 13 per cent of their comparison galaxy population).

As noted by Frederick et al. (2019), whilst SDSS J1533+4432 was observed by the Very Large Array survey, Faint Images of the Radio Sky at Twenty-cm (FIRST) (Becker, White & Helfand 1994) in the 20 cm radio band, no source was detected to an upper limit of 0.89 mJy beam⁻¹, ruling out any radio-loud AGN activity at the time of observation in 1997.

Table 6. Photometrically determined properties of AT 2018dyk's host galaxy SDSS J1533+4432. Where parameter values have been obtained from more than one source the preferred value is shown in bold.

Parameter	Unit	Value	Data source
Morphological classification		SBb	1
Star formation rate (SFR)	$\log_{10}(\mathrm{M}_{\odot}\mathrm{yr}^{-1})$	0.06 ± 0.13	2
Stellar mass	$\log_{10}(\mathrm{M}_{\odot})$		
		11.02 ± 0.02	2
		$10.68 \pm 0.04^*$	3
		$10.56 \pm 0.04^*$	4
Specific star formation rate (sSFR)	$\log_{10}(yr^{-1})$		
		-10.97 ± 0.13	Calculated using 2
		-10.62 ± 0.13	Calculated using the SFR of 2 and mass from 3
		-10.51 ± 0.13	Calculated using the SFR of 2 and mass from 4
Sérsic index			
		$2.30 \pm 0.02 *$	3
		2.20 ± 0.01	5 [†]
Half-light radius	arcseconds		
-		9.96 ± 0.06 *	3
		8.78 ± 0.06 *	4 □
		10.20 ± 0.03	5 [†]
Stellar surface mass density	$\log_{10}(M_{\odot}kpc^{-2})$		
•	2-21 0 1 /	8.14 ± 0.02	Calculated using 3
		8.56 ± 0.02	Calculated using 4
		8.46 ± 0.02	Calculated using 5

Notes. * No uncertainties for these parameters are quoted within the NSA. As these parameters are required to derive the value of further parameters, we assume a conservative estimate on the error double that of the measurement given in GSWLC-2.

- 1: MaNGA Visual Morphology Catalogue: Vázquez-Mata et al. (2022).
- 2: GSWLC-2: Salim et al. (2016) and Salim, Boquien & Lee (2018).
- 3: Sérsic-based photometry from the NSA v1_0_1: https://www.sdss4.org/dr17/manga/manga-target-selection/nsa/
- 4: Petrosian-based photometry the NSA v1_0_1: https://www.sdss4.org/dr17/manga/manga-target-selection/nsa/

3.5.2 Spatially resolved spectroscopic host galaxy analysis with MaNGA

The available pre-outburst MaNGA IFU observation allows for a detailed examination of the spatially resolved properties of SDSS J1533+4432 on much smaller physical scales than is possible with global properties. Considering local properties is known to be important for studies of transients as environmental properties can vary widely across a galaxy – a nuance that is lost when considering only the overall averaged properties and can significantly affect the interpretation of transient events (e.g., TDEs: Nicholl et al. 2019; Type Ia SNe: Kelsey et al. 2021; core-collapse SNe: Pessi et al. 2023).

The MaNGA observations for SDSS J1533+4432 were made on Plate 9870–9101 with MaNGA ID 1–199368 (Fig. 10a). Using the reported coordinates of AT 2018dyk, the local environment of AT 2018dyk is within the central spaxel (31, 31), coincident with the galactic nucleus.

We investigate Baldwin-Phillips-Terlevich (BPT; Baldwin, Phillips & Terlevich 1981) and WH α versus [N II]/H α (WHAN; Cid Fernandes et al. 2010, 2011) diagnostics produced from each spaxel, with a focus on the galactic nucleus (Figs 10b and c). We also explore the stellar velocity dispersion (Fig. 10d) and D4000 spectral index (Fig. 10e) measurement across the galaxy.

The per spaxel MaNGA BPT diagram (Fig. 10b) indicates that SDSS J1533+4432 is predominantly a star-forming galaxy with LINER emission diagnostics that serve as potential indications of some AGN activity in its nucleus. The source of these LINER emission-line signatures in SDSS J1533+4432 is actively debated

in the literature. Frederick et al. (2019) proposed that AT 2018dyk was the result of an 'AGN turn-on' event where a low-intensity AGN-LINER flared into a more active narrow-lined Seyfert-1 type nucleus. In contrast, Huang et al. (2023) favoured a TDE occurring within a LINER galaxy. Masterson et al. (2024) classified AT 2018dyk as a possible TDE, but did not include it in their 'gold' sample of MIR identified TDEs given its potential as an AGN produced contaminant.

The source of LINER emission can be difficult to identify, with both weak AGN activity and ionization from older stellar populations producing similar ionization signatures. The WHAN diagram was devised to help break this degeneracy and enable more robust classification using two typically strong emission lines, H α and [N II], with the width of $H\alpha$ and the line ratio of the two being the properties used for classification. Specifically, these diagnostics can be used to delineate LINER emission into two categories: those that are produced by 'weak AGN (wAGN)' and those generated by evolved stellar populations, so-called retired galaxies (RG). The WHAN diagram also classifies galaxies as 'pure star-forming', 'strong AGN' - analogous to the Seyfert classification on a BPT diagram and 'PG'. Frederick et al. (2019) explored the WHAN classification of SDSS J1533+4432 as a whole using the SDSS spectrum and determined a somewhat ambiguous RG/wAGN classification. Here, we utilize the available MaNGA data to better explore the galaxy's nuclear region. The MaNGA data provide a clear RG classification for the location of AT 2018dyk and its surroundings, with an SNR per spaxel exceeding 20. Additionally, we have explored the MaNGA AGN Catalog (Comerford et al. 2020), which includes WISE colour and X-ray and radio diagnostics to identify AGNs within MaNGA

[†] Value calculated from the weighted average of the *gri* pure Sérsic profile fits for comparison to Hammerstein et al. (2023b). When using the MPP-VAC-DR17 preferred Sérsic + Exponential fit, the weighted average of Sérsic index for the bulge component is 1.36 ± 0.78 . Sources:

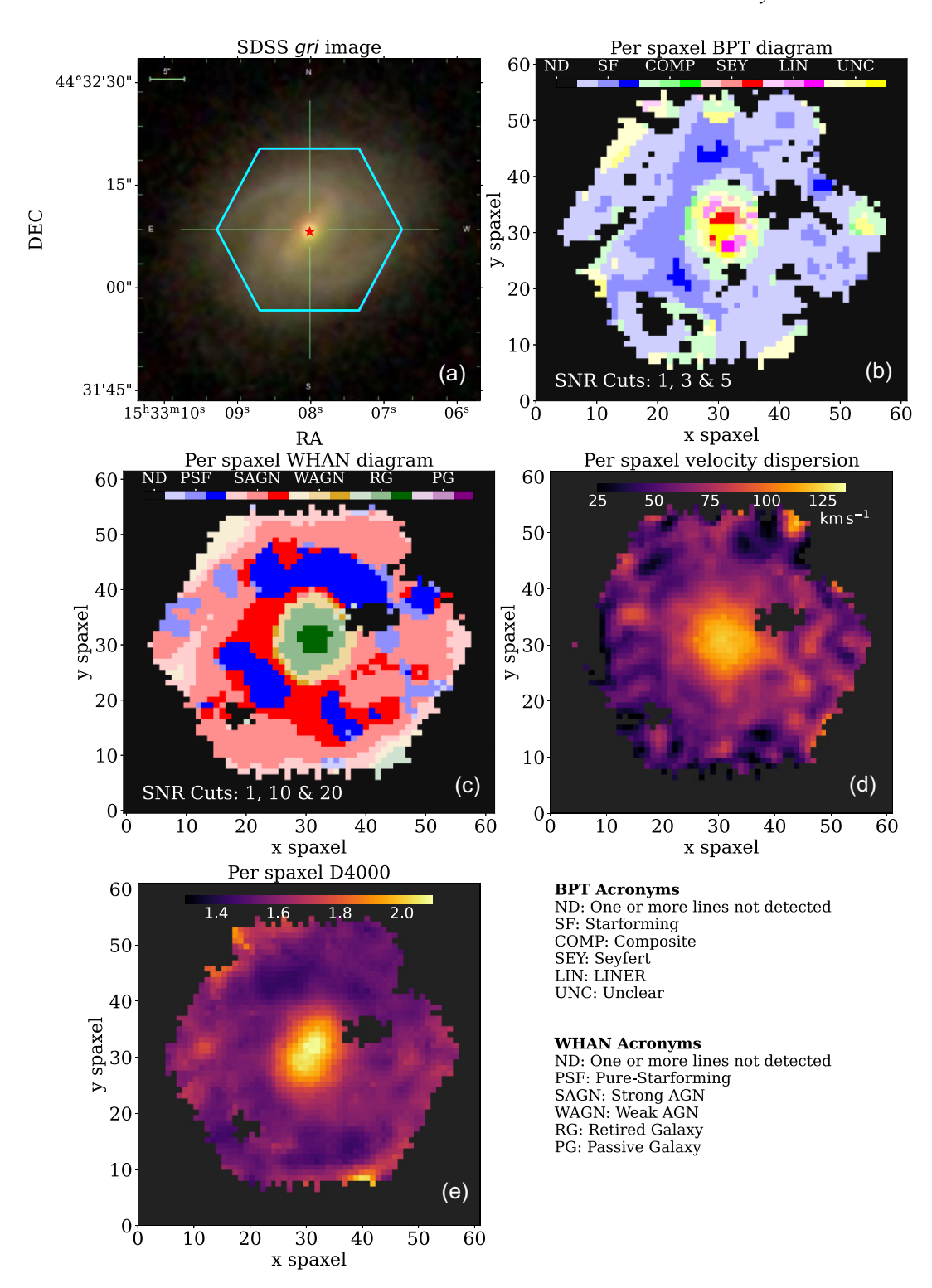


Figure 10. (a) SDSS *gri* composite image of SDSS J1533+4432. Hexagonal outline displays the footprint of the MaNGA IFU data. (b) Per spaxel combined BPT diagram of SDSS J1533+4432. Colour intensity indicates the SNR of the included emission lines in three bins at SNRs of 1, 3, and 5. Classifications use all four standard BPT diagnostic line ratios. BPT diagnostics cannot provide a clear classification for the emission-line properties at the location of AT 2018dyk. (c) Per spaxel WHAN diagram of SDSS J1533+4432. Colour intensity indicates the SNR of the included emission lines in three bins at SNRs of 1, 10, and 20. The WHAN diagram returns a clear (SNR of all lines >20) 'RG' classification for the nuclear region of SDSS J1533+4432, including the location of AT 2018dyk, indicating the LINER emission features are produced by an older stellar population rather than AGN activity. (d) Per spaxel map of the measured stellar velocity dispersion (measured in km s⁻¹) of SDSS J1533+4432. Overall velocity dispersion is within the range, though above the mean, of the velocity dispersions of TDE hosts found by Graur et al. (2018). (e) Per spaxel map of the measured *D*4000 spectral indices within SDSS J1533+4432. The increasing magnitude of this value moving radially towards the centre of the galaxy is consistent with increasing average stellar age. The spiral arms observable in both optical imaging and through BPT diagnostics are visible as the dark coloured regions above and below the galactic nucleus.

Table 7. Spectroscopically determined properties of AT 2018dyk's host galaxy SDSS J1533+4432.

Parameter	Unit	Value	Data source
Global properties			
Stellar velocity dispersion	${\rm km}~{\rm s}^{-1}$	68.0 ± 1.1	1
Central SMBH mass †	$\log_{10}(\mathrm{M}_{\odot})$	6.86 ± 0.05	1
D4000		1.65 ± 0.01	1
Local properties			
Stellar velocity dispersion	${\rm km}~{\rm s}^{-1}$	122.5 ± 1.9	2
Central SMBH mass †	$log_{10}(M_{\odot})$	7.56 ± 0.04	2
D4000		2.09 ± 0.01	2

Notes. † Calculated using the relation from Kormendy & Ho (2013). Sources:

- 1: Measured from a weighted mean of all MaNGA spaxels.
- 2: Measured from the central (31,31) spaxel of the MaNGA FU data cube coincident with the location of AT 2018dyk.

observations without using emission-line ratios. SDSS J1533+4432 is not classified as an AGN by any of these diagnostics and is thus not included in the catalogue. Based on the MIR behaviour shown in Section 3.4 and the discussion above, we conclude that the LINER emission classification for SDSS J1533+4432 is the result of an evolved stellar population rather than underlying AGN activity. This conclusion supports the assessment of Huang et al. (2023).

Initially noted by Arcavi et al. (2014) and expanded upon by French, Arcavi & Zabludoff (2016), Law-Smith et al. (2017), and Graur et al. (2018), TDEs are over-represented in quiescent Balmerstrong galaxies (also known as post-starburst or E + A galaxies). Masterson et al. (2024) investigated whether SDSS J1533+4432 could be categorized as such a galaxy using the original SDSS spectrum. Whilst the SDSS-Legacy spectrum points to a quiescent central region, there was no indication of the strong Balmer absorption required for a post-starburst classification. We extend this analysis through the MaNGA data to explore whether the local environment of AT 2018dyk is consistent with this type of stellar population using the spaxel at the location of AT 2018dyk. We find that whilst, like the larger region covered by the SDSS-Legacy spectrum, this central region hosting AT 2018dyk is quiescent, with an H α equivalent width of 1.95 \pm 0.05 Å, it again lacks the strong Balmer absorption, with a measured H δ_A spectral index of 1.28 \pm 0.16 Å, compared to the French et al. (2016) Balmer-strong threshold of >4 Å.

We also make use of the MaNGA data to investigate the stellar velocity dispersion, central SMBH mass, and the spatially resolved D4000 spectral index of SDSS J1533+4432, with these spectroscopically derived host galaxy properties summarized in Table 7. We find that the central region of SDSS J1533+4432 has a stellar velocity dispersion of 122.5 \pm 1.9 km s⁻¹ when measured at the spaxel at the coordinates of AT 2018dyk. This is consistent with, though higher than the mean, stellar velocity dispersions of the TDE hosts reported by Graur et al. (2018). When all measured spaxels are considered, we measure a mean value of 85.0 ± 0.2 km s⁻¹ which remains higher than the mean stellar velocity dispersion measured by Graur et al. (2018) of 68.0 ± 1.1 km s⁻¹.

To provide an estimate of the central SMBH mass, we use the MaNGA stellar velocity dispersion measurements and the scaling relation from Kormendy & Ho (2013). When using the mean stellar velocity measured from all spaxels, a mass of $6.86 \pm 0.05 \log_{10}(M_{\odot})$ is obtained. A higher mass estimate of $7.56 \pm 0.04 \log_{10}(M_{\odot})$ is measured when only the central spaxel is considered, corresponding to the higher central velocity dispersion. We adopt the lower mass estimate for our analysis in Section 4.1, as the Kormendy & Ho

(2013) relation was determined using full galaxy, rather than local, spectra.

The D4000 spectral index (a measure of the continuum difference before and after the 4000 Å spectral break) has long been used as a proxy for stellar population ages (Poggianti & Barbaro 1997). Low values of the D4000 index ($\sim < 1.6$) indicate young stellar populations (which should be closely matched to star-forming regions identified through other methods), whilst larger values of D4000 indicate older stellar populations ($\sim > 1.6$, Loubser et al. 2016). The resolved map of the D4000 index values (Fig. 10e) matches the properties shown by both the BPT and WHAN diagnostics. The visible spiral arms and outer regions of SDSS J1533+4432 have the low D4000 values expected of young stellar populations with D4000 increasing towards the galactic nucleus – well matched by the 'RG' classification of this region in the WHAN diagram.

3.6 SMBH and stellar mass estimation with TDEMASS

For comparison to the spectroscopically derived host galaxy SMBH masses, we utilize the TDEMASS PYTHON code (Ryu, Krolik & Piran 2020) to estimate both the SMBH mass and the mass of the star undergoing disruption in AT 2018dyk. TDEMASS is an implementation of the slow circularization and shock-driven model for a TDE's optical luminosity, as described by Piran et al. (2015).

We use the peak blackbody luminosity as calculated by Huang et al. (2023) and assume a peak blackbody temperature matching the earliest measurement calculated by Hinkle et al. (2021) (\sim 24 500 $^{+1200}_{-1100}$ K at \sim 20 d post-peak) as the input parameters for TDEMASS. We use both the original TDEMASS model described by Ryu et al. (2020) and the new model incorporating slow-cooling described by Krolik, Piran & Ryu (2025) to provide SMBH mass estimates.

The model not incorporating slow-cooling finds an SMBH mass of $6.63_{+0.17}^{-0.24}\log_{10}(M_{\odot})$ and the mass of the star undergoing disruption to be $0.4_{+0.19}^{-0.18}~M_{\odot}$, with the model including cooling measuring the respective parameters to be $6.94_{+0.11}^{-0.20}\log_{10}(M_{\odot})$ and $0.25_{+0.15}^{-0.20}~M_{\odot}$. Both estimates are on the low end of the range of SMBH black hole estimates for AT 2018dyk (see Fig. 11) but are consistent with our estimate measured using the mean stellar velocity dispersion within the MaNGA data.

As described by Ryu et al. (2020), whilst the dominant factor in the determination of SMBH mass is peak blackbody temperature, for a given temperature, increasing the peak blackbody luminosity will increase the measured SMBH mass. Additionally, the measured values for the stellar mass determined from both models is significantly lower than what is expected of a Sun-like star. The calculation of stellar mass is dominated by peak blackbody luminosity, with the parameters being positively correlated.

From the presence of a significant MIR outburst and CrL emission, it is clear that AT 2018dyk occurs in a gas-rich environment. Thus, significant absorption of its peak emission could be expected which in turn would lead to a lower measurements of SMBH and stellar mass. As such, direct application of such models should be treated with care as the assumptions used may not be directly applicable to the physical configuration of events such as AT 2018dyk.

Alternatively, if the model assumptions do hold, the lower stellar mass (and relatively faint overall luminosity) estimated by TDEMASS, could be explained by AT 2018dyk being produced by a partial disruption of a larger star, as suggested by Huang et al. (2023).

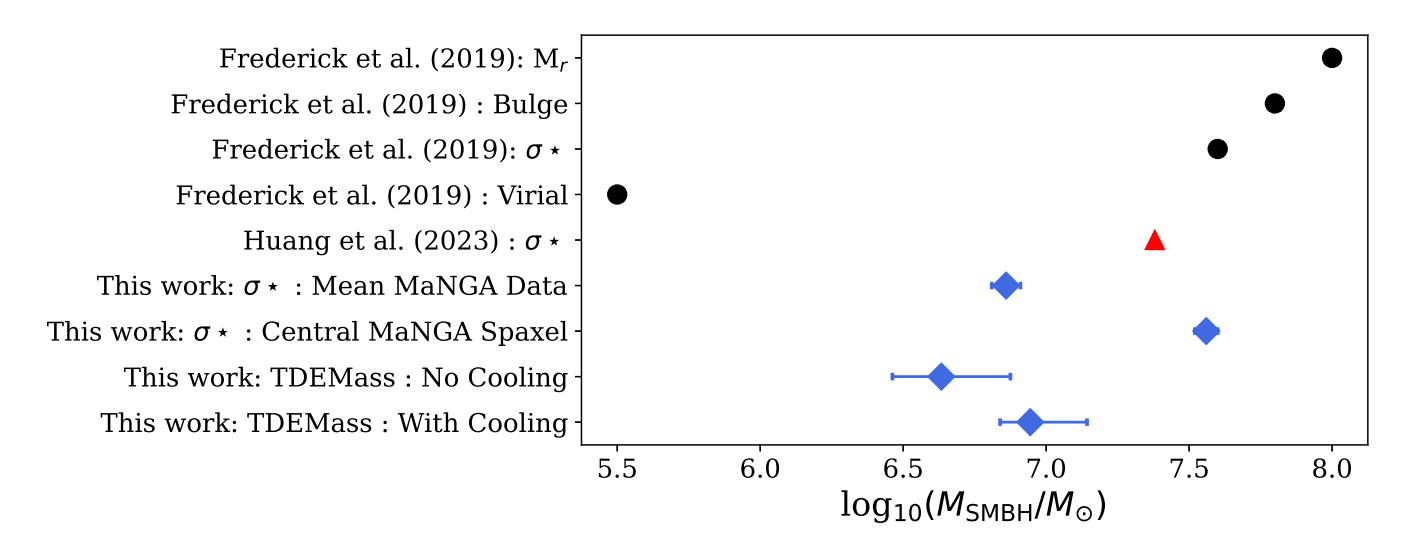


Figure 11. Compiled mass estimates for the SMBH at the centre of AT 2018dyk's host galaxy. Data collated from Frederick et al. (2019), Huang et al. (2023), and this work. Note that the error bars reflect measurement uncertainties (where available) only and do not include any statistical uncertainties resulting from intrinsic scatter in the relations used.

4 DISCUSSION

4.1 Optical emission-line behaviour

Increasing [O III]λ5007 Å emission has previously been observed in TDE-ECLEs, with this behaviour first identified by Yang et al. (2013) in follow-up spectra obtained several years after the Wang et al. (2012) SDSS discovery spectra. The most notable example of this evolution is seen in the TDE-ECLE SDSS J1342+0530 (Clark et al. 2024), in which the [O III]λ5007 Å emission line now dominates the spectrum. This increase in [O III] λ 5007 Å line strength in SDSS J1342+0530 has also been accompanied by the expected increase in the linked [O III] \(\lambda 4959 \) \(\text{Å emission}. \) The [O III] \(\lambda 4959 \) \(\text{Å} \) emission line is not seen in pre-DESI spectra of AT 2018dyk as the overall weakness of the feature results in a low SNR. As previously noted, a similar increase in line strength is observed post outburst in the $[O II]\lambda 3726$, 3728 Å doublet with both this and the other oxygen features also being redshifted from the expected 0 km s⁻¹ position by $\sim 100 \, \mathrm{km \, s^{-1}}$. We show all three of these oxygen features in velocity space in Fig. 12.

To investigate this emission behaviour further, we conduct line fitting of the three oxygen features showing increased line fluxes post outburst and perform a comparative analysis with SDSS J1342+0530. Given the small difference in phase between the Keck + LRIS and LCOGT + FLOYDS spectra of AT 2018dyk and the significantly higher resolution of the Keck + LRIS spectrum, the LCOGT + FLOYDS spectrum is not included in this analysis. For the same reasons, we prefer the DESI spectrum of SDSS J1342+0530 over the one taken with NTT + EFOSC2. Additionally, where possible, we analogously explore the properties of the standard AGN diagnostic lines along with the coronal Fe lines in each spectrum. The emission-line fitting makes use of the SPECUTILS (Earl et al. 2024) PYTHON package (in turn relying on ASTROPY; Astropy Collaboration 2013, 2018, 2022) and includes local region continuum fitting and removal. Given the difficulty in correcting for both stellar continua and the presence of transient emission, we do not attempt to correct the spectra of either object for these effects. Instead, we present these measurements as observed, with a focus on the relative changes in observed features and on their velocity profiles. Specifically for

AT 2018dyk, the lack of directly observable $H\beta$ emission at phases other than during the early evolution of the TDE outburst, which is dominated by TDE rather than host galaxy flux, prevents the construction of the usual optical diagnostic diagrams on a time varying basis. Frederick et al. (2019) provide measurements of these corrected line ratios (see e.g., figs 13 and 18–21), work which we do not duplicate here. As our spectral comparisons have shown, the SDSS Legacy, central spaxel MaNGA, and DESI spectra are all very similar. As such, no significant changes in measured line ratios (stellar absorption corrected or otherwise) are expected, with the exception of those involving oxygen, which as previously described, showed significant evolution by the time of the DESI spectrum.

For the $[O II]\lambda 3726$, 3728 Å doublet fit, due to the resolution of our spectra, we use a single Gaussian to represent both lines. Additionally, the lines composing the [S II] doublet and the pair of [N II] lines in the $H\alpha$ complex are tied to have the same width in wavelength space. Where one or more lines are blended, the components are fitted simultaneously. An example of the fitting results is shown in Fig. 13. The full results of this fitting are given in Appendix C, split by non-coronal (Table C1) and coronal emission lines (Table C2). A summary of the resulting line ratios is provided in Table C3.

As the latest DESI spectrum now closely matches the preoutburst SDSS spectrum (with the exception of this increased [O III] emission), and the fitted [O III] λ 5007 Å feature is consistent in both peak offset (DESI: 120 \pm 10 km s $^{-1}$ compared to SDSS: 110 \pm 20 km s $^{-1}$) and FWHM (full width at half-maximum) velocity (DESI: 280 \pm 30 km s $^{-1}$ compared to SDSS: 290 \pm 40 km s $^{-1}$) with the preoutburst SDSS spectrum, we consider the most likely cause of this increased [O III] emission to be the delayed response of more distant material to the transient TDE flux rather than a change in the long-term accretion behaviour of the SMBH within SDSS J1533+4432. If such a change had occurred, we would expect to also see changes in the other AGN diagnostic lines relative to the SDSS spectrum which is not observed (e.g., [N II] and [S II] as seen in the bottom panel of Fig. 3).

Additionally, in the Keck spectrum the observed coronal lines are of comparable strength to, though wider than, the [OIII] λ 5007 Å emission line. Differences in the FWHM velocities between coronal

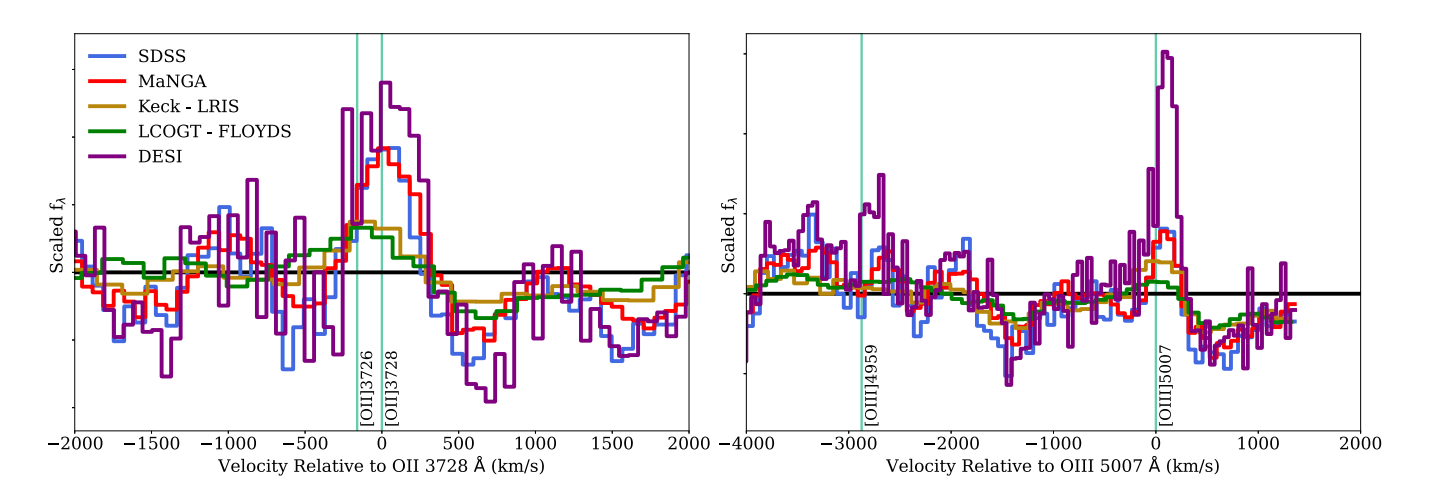


Figure 12. Left: $[O II]\lambda 3726$, 3728 Å doublet line region in velocity space relative to the expected rest position of $[O II]\lambda 3728$ Å. The relative intensity of the feature drops during outburst before increasing in strength, exceeding the relative intensity of the feature prior to the original outburst. Right: line region of the $[O III]\lambda 4959$ Å and 5007 Å lines in velocity space relative to the expected position of $[O III]\lambda 5007$ Å. The $[O III]\lambda 4959$ Å line is only observable in the most recent DESI spectrum. A sharp increase in $[O III]\lambda 5007$ Å emission is clearly observable in the most recent DESI spectrum. Slight redshifts ($\sim 100 \text{ km s}^{-1}$) in the observed line peaks are seen in both line regions. These are explored in detail in Section 4.1.

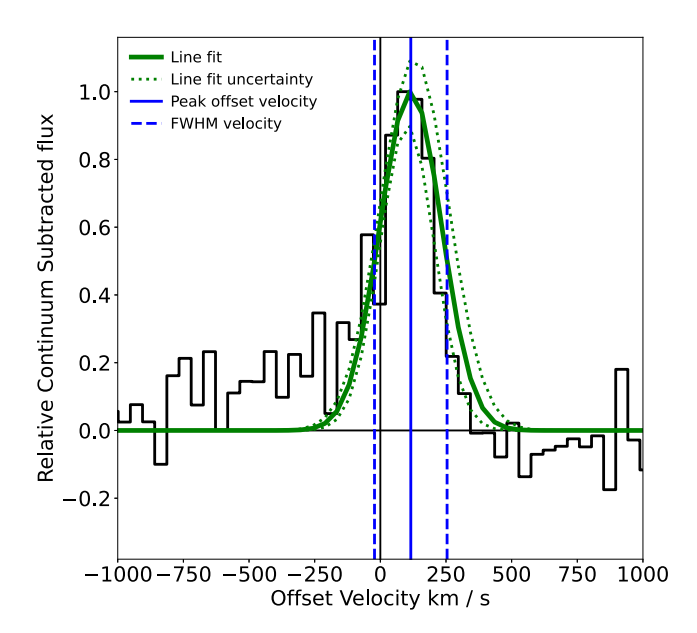


Figure 13. Fit to the [O III]λ5007 Å emission line in the DESI spectrum of AT 2018dvk.

and non-coronal emission lines were also observed in the CrL-TDE 2022upj and investigated by Newsome et al. (2024).

Following Newsome et al. (2024), we use the measured FWHM velocities and our estimate of the SMBH mass determined using the mean MaNGA stellar velocity dispersion data to calculate virial radii around the SMBH, and hence the distance between the SMBH and the emitting material. This calculation was performed for a range of emission lines for each spectroscopic observation of AT 2018dyk. Here, we again favour the higher resolution Keck spectrum over the similarly timed FLOYDS spectrum. We find that the emission locations of the spectral lines are consistent within the uncertainties between the pre (SDSS and MaNGA) and post (DESI) spectra of AT 2018dyk (Table D1 and Fig. 14). The [O III]λ4959 Å line that had developed by the time of the DESI spectrum is also consistent in distance with the other narrow lines. Both the [O III]λ4959 and

5007 Å lines are located at greater distances from the SMBH than the coronal iron features, consistent with their more delayed line strength increases in response to the TDE outburst. In the Keck spectrum, $H\alpha$ and $[O\,III]\lambda5007$ Å have increased FWHMs with a resulting decrease in the calculated virial distances, which we attribute to the effect of the ongoing TDE.

As with the measured locations of the coronal lines in TDE 2022upj (Newsome et al. 2024), we find that the [Fe XIV] emission is located nearest to the black hole, followed by the [Fe X] line. The [Fe VII] lines (the [Fe VII] λ 3759 Å line is not included in Fig. 14 due to its much larger uncertainty but is consistent with the other [Fe VII] lines) and [Fe XI] λ 7894 Å are located at the largest distances from the black hole. However, we note that the lower SNR of the [Fe XI] λ 7894 Å makes its true distance harder to measure as the FWHM velocity may be underestimated. This layered line location structure is similar to the line structure of TDE 2022upj observed by Newsome et al. (2024), indicating similar complexities in the gas structure close to the SMBH. However, the distances determined here for the line formation in AT 2018dyk are larger than those determined for TDE 2022upj. This discrepancy may be due to the larger mass of the SMBH in AT 2018dyk's host galaxy.

Depending on the mass estimate of TDE 2022upj used, we find the mass ratio between the SMBHs responsible for AT 2018dyk (when using the value measured from the mean MaNGA stellar velocity dispersion) and TDE 2022upj to be 3.6–14.5. The corresponding mean ratio between the emission-line distances is 0.9–3.5. In both cases, the mean line distance ratio is found to be lower than SMBH mass ratio. One would naively expect a correlation between the mass of the SMBH and the distance to its surrounding ISM; measurements of these ratios in future CrL-TDEs could reveal the exact nature of such a correlation and constrain its underlying physics.

4.2 MIR photometric behaviour

As described in Section 3.4, pre-outburst MIR photometry of AT 2018dyk suggests a galaxy with little underlying variability; a W1-W2 colour consistent with no significant AGN activity; and with AllWISE photometry consistent with a spiral galaxy hosting no AGN activity (obscured or otherwise) based on the classification

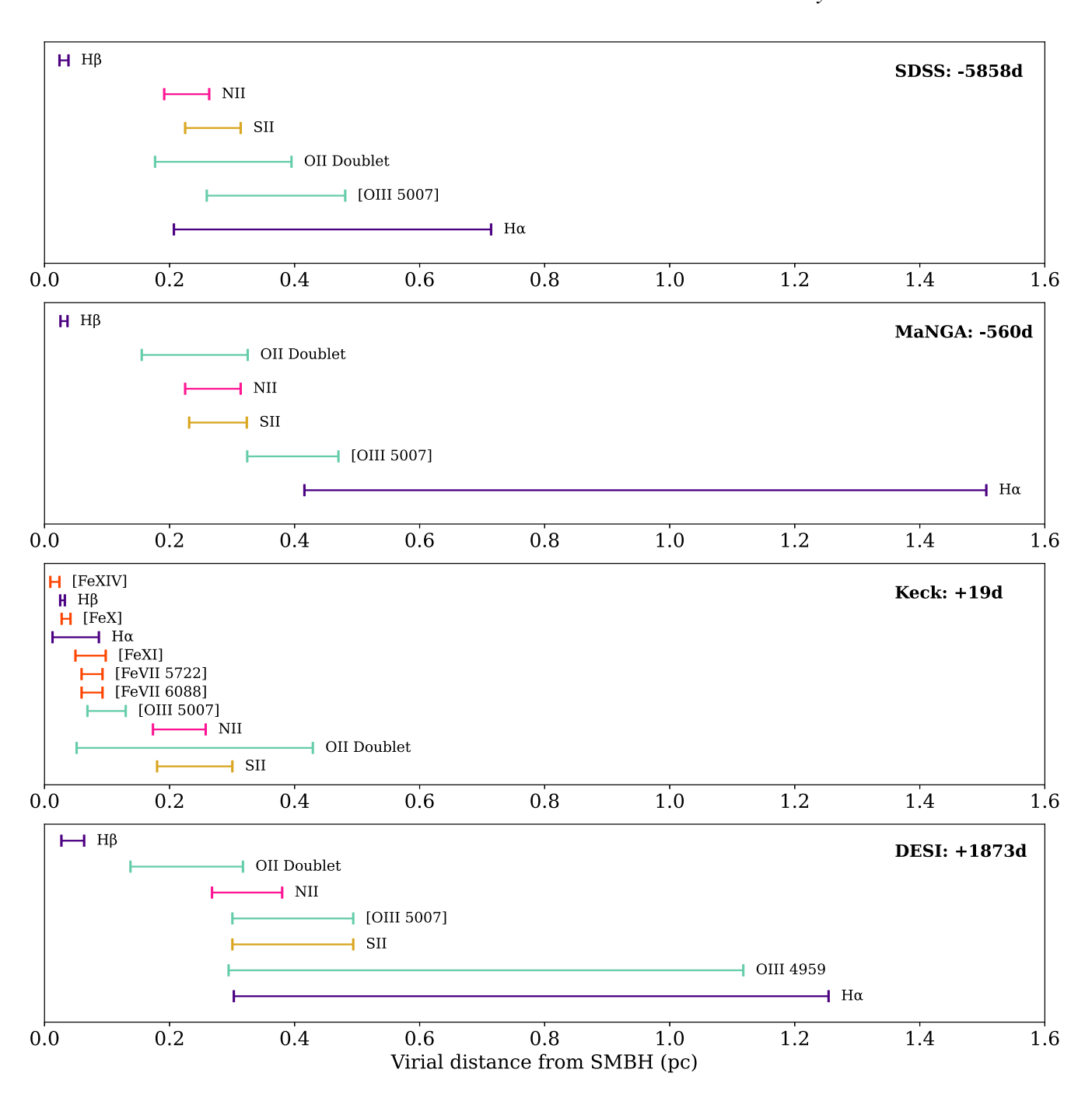


Figure 14. Virial distance estimates for the formation location of the measured narrow emission lines based on their FWHM velocities. Note the scale difference between the lines observed in the Keck spectrum compared the others. This difference is the result of several of the lines in the Keck spectrum being directly affected by the ongoing active TDE phase.

scheme of Wright et al. (2010). During the outburst, AT 2018dyk, like other CrL-TDEs, reddened significantly in W1-W2 colour, whilst remaining bluer than the Stern et al. (2012) AGN colour cut. ECLE-TDEs and other CrL-TDEs have shown stronger W1-W2 reddening during outburst and cross the Stern et al. (2012) colour cut.

This, in combination with the smaller amplitude of the MIR flare of AT 2018dyk compared to the other coronal line displaying objects in the comparison sample, and the shorter overall duration of its outburst, points to differences in the physical structure of the material responsible for reprocessing the TDE flux into the observed

MIR emission. These differences are most likely a combination of reduced covering factor, density, and overall mass of the material surrounding the SMBH. A detailed physical modelling of the ISM around the SMBH may be able to break the degeneracies between these variables, but it is beyond the scope of this work.

When explored collectively, trends are evident in the MIR behaviour of CrL-TDEs (Fig. 9). First, the relationship between $\Delta W1$ and $\Delta W2$ is not one-to-one. Instead, the quadratic curve best fit to the data (as determined by a likelihood-ratio test), reflects the increased strength of the outbursts in the W2 band compared to W1 and shown

in equation (2)

$$\Delta W2 = -0.18(\Delta WI)^2 + 0.7(\Delta WI) - 0.48 \tag{2}$$

When examined further in $\Delta(W1-W2)$ versus $\Delta W2$ colour space, those CrL-TDEs with the brightest MIR outbursts are also seen to have the reddest outbursts. This colour–luminosity relation is best fitted by the linear relation:

$$\Delta(WI - W2) = -0.25(\Delta W2) + 0.19 \tag{3}$$

Unfortunately, given that only four objects in this parameter space can be used for fitting this relation (the rest are only limits), it is not statistically significant at this time. Whilst further observations will be required to confirm this relation statistically, qualitatively such a relation is likely the result of larger quantities or densities of circumnuclear material near the SMBHs involved, or larger covering fractions reprocessing more TDE emission into the MIR bands (e.g., Hinkle 2024). We make two further observations on the robustness of this observed relation. The fourth object included in the fit for this relationship (AT 2018gn) was added to the comparison sample during internal review and agreed well with the initial identification of the relationship with the other three included transients (AT 2017gge, AT 2018dyk, and AT 2018bcb). Moreover, three additional CrL-TDEs are observed to be close to (or indeed at) their outburst colour peak at the time of most recent MIR observations (TDE 2022fpx. TDE 2022upi, and VT J1548), though would require additional observations to confirm this. All of these objects have already reached clear peaks in their W2 light curves (i.e., their $\Delta W2$ values are fixed); further increases in their $\Delta(W1 - W2)$ values would improve their already close scatter from the determined relation. This is further evidence that MIR observations of this class of objects are essential to fully understand their properties and evolution, with the end of the NEOWISE-R mission opening a significant gap in our observational

We also note that all known CrL-TDEs have displayed MIR outbursts in both W1 and W2 bands greater than 0.5 mag, consistent with both coronal emission lines and MIR outbursts requiring significant amounts of material in proximity to the SMBH for the reprocessing of TDE emission. Other TDE's (such as TDE 2019azh) show that small MIR outbursts can occur without the development of coronal lines, hinting at a range of environmental configurations and differing thresholds for the occurrence of each feature.

5 CONCLUSIONS

In this work, we have published a new follow-up spectrum of the host galaxy of the nuclear transient AT 2018dyk. Using this spectrum, as well as archival data, we have conducted a thorough analysis of the photometric and spectroscopic properties of AT 2018dyk and its host galaxy. We make the following observations.

We conclude that AT 2018dyk is the result of a TDE occurring in an environment rich in circumnuclear material, resulting in the reprocessing of TDE flux into both high ionization Fe coronal lines and an MIR outburst. Spectroscopic analysis of the local region of the host galaxy (SDSS J1533+4432) in which AT 2018dyk occurred reveals that the previously reported LINER emission signatures are the result of an evolved stellar population rather than underlying AGN activity.

Additionally, SDSS J1533+4432 – sits within or close to the transitional 'green valley', with a centrally concentrated stellar population housing an older quiescent population in its nucleus and some star formation still ongoing within the outer spiral arms. An analysis of the host properties of SDSS J1533+4432 shows that it is

consistent with known TDE host populations, though it lies toward the high end of the expected stellar mass range (Law-Smith et al. 2017; Graur et al. 2018; Hammerstein et al. 2023a).

Furthermore, the optical evolution of AT 2018dyk itself is consistent with an outburst produced by a single TDE. The most recent DESI spectrum now closely matches the archival, pre-outburst SDSS Legacy and MaNGA spectra, with the exceptions of significant increases in strength of the [O III]λ5007 Å and [O II]λ3728 Å emission features. Similar strengthening of [O III]λ5007 Å emission in particular has been observed in the original TDE-linked ECLE sample by Yang et al. (2013) and Clark et al. (2024). Given the lack of evolution in other AGN diagnostic lines compared to the SDSS spectrum, we attribute this increased emission to more distant material responding to the short-term TDE emission rather than a long-term change of AGN activity state. Emission-line fitting also confirms that AT 2018dyk matches the qualitative definition of an ECLE, with one or more coronal lines being at least 20 per cent the line strength of [O III]λ5007 Å at the time of outburst.

In addition to this optical behaviour, AT 2018dyk displayed MIR evolution consistent with a TDE-linked ECLE: a ~ 0.5 mag outburst in both the W1 and W2 bands, with an accompanying W1 – W2 reddening of ~ 0.4 mag. However, this outburst was on a shorter time-scale, and had a lower amplitude, than observed in archival TDE linked ECLEs (Dou et al. 2016; Clark et al. 2024). Photometric variability analysis of AT 2018dyk and the other CrL-TDEs shows lower levels of variability prior to and post outburst than has been seen in either CL-LINERs or AGN-ECLEs, aiding in the confirmation that these classes of transient are distinct from one another in observable properties.

Virial distance estimates based on the FWHM velocities of the narrow emission lines and SMBH masses suggest that the gas structures around the SMBHs responsible for AT 2018dyk and TDE 2022upj are similar. Whilst the calculated distances to the emitting material are larger in AT 2018dyk, the material is relatively closer to the SMBH compared to the mass ratio of the two SMBHs.

Comparisons between AT 2018dyk and other TDEs displaying MIR outbursts reveal tentative evidence for a colour–luminosity relationship in their MIR evolution. Specifically, those objects with brighter MIR flares show more significant reddening at outburst. This may be a consequence of such objects having larger dust covering fractions or other environmental factors that lead to reprocessing more of the initial UV/optical continuum produced by the TDE. Whilst the number of objects for which these measurements can be made without relying on upper limits is limited (four) and prevents the statistical confirmation of the relation, the range of behaviour already extends over 3 mag in W2 outburst amplitude, highlighting the diverse range of physical configurations in these systems. MIR observations play a critical role developing our understanding of these objects; the end of the NEOWISE-R mission has created a key gap in our observational capabilities.

In conclusion, we find that AT 2018dyk was a TDE that went on to excite iron coronal lines in its host galaxy. This object continues to strengthen the link between TDEs and variable ECLEs. It also stresses the necessity for long-term, multiwavelength follow-up of nuclear transients over a time-scale of years in order to properly classify them and study the environments in which they occur.

ACKNOWLEDGEMENTS

We thank the anonymous reviewer for their helpful comments and feedback.

PC was supported by the Science & Technology Facilities Council grant ST/V001000/1.

PC and OG were supported by the Science & Technology Facilities Council [grants ST/S000550/1 and ST/W001225/1].

CG thanks the Science Technology Facilities Council (STFC) for support from the Durham consolidated grant (ST/T000244/1).

This material is based upon work supported by the U.S. Department of Energy (DOE), Office of Science, Office of High-Energy Physics, under contract no. DE-AC02-05CH11231, and by the National Energy Research Scientific Computing Center, a DOE Office of Science User Facility under the same contract. Additional support for DESI was provided by the U.S. National Science Foundation (NSF), Division of Astronomical Sciences under contract no. AST-0950945 to the NSF's National Optical-Infrared Astronomy Research Laboratory; the Science and Technology Facilities Council of the United Kingdom; the Gordon and Betty Moore Foundation; the Heising-Simons Foundation; the French Alternative Energies and Atomic Energy Commission (CEA); the National Council of Humanities, Science and Technology of Mexico (CONAHCYT); the Ministry of Science, Innovation and Universities of Spain (MI-CIU/AEI/10.13039/501100011033), and by the DESI Member Institutions: https://www.desi.lbl.gov/collaborating-institutions. Any opinions, findings, and conclusions or recommendations expressed in this material are those of the author(s) and do not necessarilv reflect the views of the U.S. National Science Foundation. the U. S. Department of Energy, or any of the listed funding agencies.

The authors are honoured to be permitted to conduct scientific research on Iolkam Du'ag (Kitt Peak), a mountain with particular significance to the Tohono O'odham Nation.

Funding for the Sloan Digital Sky Survey IV has been provided by the Alfred P. Sloan Foundation, the U.S. Department of Energy Office of Science, and the Participating Institutions.

SDSS-IV acknowledges support and resources from the Center for High Performance Computing at the University of Utah. The SDSS website is www.sdss4.org. SDSS-IV is managed by the Astrophysical Research Consortium for the Participating Institutions of the SDSS Collaboration including the Brazilian Participation Group, the Carnegie Institution for Science, Carnegie Mellon University, Center for Astrophysics | Harvard & Smithsonian, the Chilean Participation Group, the French Participation Group, Instituto de Astrofísica de Canarias, The Johns Hopkins University, Kavli Institute for the Physics and Mathematics of the Universe (IPMU)/University of Tokyo, the Korean Participation Group, Lawrence Berkeley National Laboratory, Leibniz Institut für Astrophysik Potsdam (AIP), Max-Planck-Institut für Astronomie (MPIA Heidelberg), Max-Planck-Institut für Astrophysik (MPA Garching), Max-Planck-Institut für Extraterrestrische Physik (MPE), National Astronomical Observatories of China, New Mexico State University, New York University, University of Notre Dame, Observatário Nacional/MCTI, The Ohio State University, Pennsylvania State University, Shanghai Astronomical Observatory, United Kingdom Participation Group, Universidad Nacional Autónoma de México, University of Arizona, University of Colorado Boulder, University of Oxford, University of Portsmouth, University of Utah, University of Virginia, University of Washington, University of Wisconsin, Vanderbilt University, and Yale University.

The Liverpool Telescope is operated on the island of La Palma by Liverpool John Moores University in the Spanish Observatorio del Roque de los Muchachos of the Instituto de Astrofisica de Canarias with financial support from the UK Science and Technology Facilities Council.

DATA AVAILABILITY

The data underlying this work are available in the article and in its online supplementary material available through Zenodo (Clark et al. 2025).

REFERENCES

Abdurro'uf et al., 2022, ApJS, 259, 35

Akaike H., 1974, IEEE Trans. Autom. Control, 19, 716

Alexander K. D., Wieringa M. H., Berger E., Saxton R. D., Komossa S., 2017, ApJ, 837, 153

Antonucci R., 1993, ARA&A, 31, 473

Arcavi I. et al., 2014, ApJ, 793, 38

Arcavi I. et al., 2018, Astron. Telegram, 11953, 1

Assef R. J., Stern D., Noirot G., Jun H. D., Cutri R. M., Eisenhardt P. R. M., 2018, ApJS, 234, 23

Astropy Collaboration, 2013, A&A, 558, A33

Astropy Collaboration, 2018, AJ, 156, 123

Astropy Collaboration, 2022, ApJ, 935, 167

Auchettl K., Guillochon J., Ramirez-Ruiz E., 2017, ApJ, 838, 149

Bade N., Komossa S., Dahlem M., 1996, A&A, 309, L35

Baldwin J. A., Phillips M. M., Terlevich R., 1981, PASP, 93, 5

Becker R. H., White R. L., Helfand D. J., 1994, in Crabtree D. R., Hanisch
R. J., Barnes J., eds, ASP Conf. Ser. Vol. 61, Astronomical Data Analysis
Software and Systems III. Astron. Soc. Pac., San Francisco, p. 165

Belfiore F. et al., 2019, AJ, 158, 160

Bellm E. C., 2014, Proc. Third Hot-Wiring the Transient Universe Workshop. p. 27

Bellm E. C. et al., 2019, PASP, 131, 18002

Biswas P., Wadadekar Y., 2024, ApJ, 970, 83

Bundy K. et al., 2015, ApJ, 798, 7

Callow J. et al., 2024, MNRAS, 535, 1095

Callow J. et al., 2025, MNRAS, 539,231

Cannizzo J. K., Gehrels N., 2009, ApJ, 700, 1047

Cannizzo J. K., Lee H. M., Goodman J., 1990, ApJ, 351, 38

Cannizzo J. K., Troja E., Lodato G., 2011, ApJ, 742, 32

Chakraborty J. et al., 2025, ApJL, 983, L39

Charalampopoulos P. et al., 2022, A&A, 659, A34

Cherinka B. et al., 2019, ApJ, 158, 74

Cid Fernandes R., Stasińska G., Schlickmann M. S., Mateus A., Vale Asari N., Schoenell W., Sodré L., the SEAGal Collaboration, 2010, MNRAS, 403, 1036

Cid Fernandes R., Stasińska G., Mateus A., Vale Asari N., 2011, MNRAS, 413, 1687

Clark P. et al., 2024, MNRAS, 528, 7076

Clark P., Callow J., Graur O., Greenwell C. L., Hu L., 2025, Zenodo, Zenodo

Comerford J. M. et al., 2020, ApJ, 901, 159

DESI Collaboration, 2016a, preprint (arXiv:1611.00036)

DESI Collaboration, 2016b, preprint (arXiv:1611.00037)

DESI Collaboration, 2022, AJ, 164, 207

DESI Collaboration, 2024a, preprint (arXiv:2411.12020)

DESI Collaboration, 2024b, J. Cosmol. Astropart. Phys., 2025, 012

DESI Collaboration, 2024c, J. Cosmol. Astropart. Phys., 2025, 124

DESI Collaboration, 2024d, preprint (arXiv:2411.12021)

DESI Collaboration, 2024e, J. Cosmol. Astropart. Phys., 2025, 021

DESI Collaboration, 2024f, preprint (arXiv:2411.12022)

DESI Collaboration, 2024g, AJ, 168, 58

DESI Collaboration, 2025, preprint (arXiv:2503.14745)

Domínguez Sánchez H., Margalef B., Bernardi M., Huertas-Company M., 2022, MNRAS, 509, 4024

Dou L., Wang T.-g., Jiang N., Yang C., Lyu J., Zhou H., 2016, ApJ, 832, 188

Dou L., Wang T., Yan L., Jiang N., Yang C., Cutri R. M., Mainzer A., Peng B., 2017, ApJ, 841, L8

Earl N. et al., 2024, Astropy/Specutils: V1.15.0, Zenodo, available at: https://zenodo.org/records/11099077

894 P. Clark et al. Evans C. R., Kochanek C. S., 1989, ApJ, 346, L13 Falco E., Calkins M., Prieto J. L., Stanek K. Z., 2018, Transient Name Server Classification Report, 2018-81, 1 Faris S. et al., 2024, ApJ, 969, 104 Fischer J.-L., Domínguez Sánchez H., Bernardi M., 2019, MNRAS, 483, Fitzpatrick E. L., 1999, PASP, 111, 63 Frederick S. et al., 2019, ApJ, 883, 31 Fremling C., 2023, Transient Name Server Discovery Report, 2023-1230, 1 French K. D., Arcavi I., Zabludoff A., 2016, ApJ, 818, L21 Graur O., French K. D., Zahid H. J., Guillochon J., Mandel K. S., Auchettl K., Zabludoff A. I., 2018, ApJ, 853, 39 Guy J. et al., 2023, AJ, 165, 144 Hahn C. et al., 2023, AJ, 165, 253 Hammerstein E. et al., 2023a, ApJ, 942, 9 Hammerstein E. et al., 2023b, ApJ, 957, 86 Hills J. G., 1975, Nature, 254, 295 Hinkle J. T., 2024, MNRAS, 531, 2603 Hinkle J. T., Holoien T. W.-S., Shappee B. J., Auchettl K., 2021, ApJ, 910, Hinkle J. T., Shappee B. J., Holoien T. W. S., 2024, MNRAS, 528, 4775 Huang S., Jiang N., Lin Z., Zhu J., Wang T., 2023, MNRAS, 525, 4057 Izotov Y. I., Thuan T. X., 2009, ApJ, 707, 1560 Kelsey L. et al., 2021, MNRAS, 501, 4861 Koljonen K. I. I. et al., 2024, MNRAS, 532, 112 Komossa S. et al., 2008, ApJ, 678, L13 Komossa S. et al., 2009, AJ, 701, 105 Kormendy J., Ho L. C., 2013, ARA&A, 51, 511 Krolik J., Piran T., Ryu T., 2025, preprint (arXiv:2409.02894) Lacy J. H., Townes C. H., Hollenbach D. J., 1982, ApJ, 262, 120 Law-Smith J., Ramirez-Ruiz E., Ellison S. L., Foley R. J., 2017, ApJ, 850, 22 Levi M. et al., 2013, preprint (arXiv:1308.0847) Li J., Wang Z.-X., Zheng D., Zhang J.-J., Zhu L.-T., Chen Z.-Y., 2023, Res. Astron. Astrophys., 23, 025012 Lodato G., Rossi E. M., 2011, MNRAS, 410, 359 Loubser S. I., Babul A., Hoekstra H., Mahdavi A., Donahue M., Bildfell C., Voit G. M., 2016, MNRAS, 456, 1565 Mainzer A. et al., 2014, ApJ, 792, 30 Malyali A. et al., 2021, A&A, 647, A9 Masci F. J. et al., 2023, preprint (arXiv:2305.16279) Masterson M. et al., 2024, ApJ, 961, 211 Mateos S. et al., 2012, MNRAS, 426, 3271 Mummery A., van Velzen S., Nathan E., Ingram A., Hammerstein E., Fraser-Taliente L., Balbus S., 2024, MNRAS, 527, 2452 Nagao T., Taniguchi Y., Murayama T., 2000, AJ, 119, 2605 Netzer H., 2015, ARA&A, 53, 365 Neustadt J. M. M. et al., 2020, MNRAS, 494, 2538 Neustadt J. M. M. et al., 2023, MNRAS, 521, 3810

Newsome M., Arcavi I., Dgany Y., Pellegrino C., 2022, Transient Name

```
7055
Pessi T. et al., 2023, A&A, 677, A28
Phinney E. S., 1989, Nature, 340, 595
Piran T., Svirski G., Krolik J., Cheng R. M., Shiokawa H., 2015, ApJ, 806,
   164
Poggianti B. M., Barbaro G., 1997, A&A, 325, 1025
Rees M. J., 1988, Nature, 333, 523
Ryu T., Krolik J., Piran T., 2020, ApJ, 904, 73
Salim S., 2014, Serb. Astron. J., 189 1
Salim S. et al., 2016, ApJS, 227, 2
Salim S., Boquien M., Lee J. C., 2018, ApJ, 859, 11
Schlafly E. F., Finkbeiner D. P., 2011, ApJ, 737, 103
Schlafly E. F. et al., 2023, AJ, 166, 259
Shingles L. et al., 2021, Transient Name Server AstroNote, 7, 1
Shitrit N., Mohsen S., Keinan I., Katz T., Moore T., Bruch R. J., Yaron O.,
   2024, Transient Name Server Classification Report, 2024-3255, 1
Short P. et al., 2023, MNRAS, 525, 1568
Smee S. A. et al., 2013, AJ, 146, 32
Smith K. W. et al., 2020, PASP, 132, 85002
Smith N. et al., 2009, ApJ, 695, 1334
Somalwar J. J., Ravi V., Dong D., Graham M., Hallinan G., Law C., Lu W.,
   Myers S. T., 2022, ApJ, 929, 184
Somalwar J. J. et al., 2025, ApJ, 982, 163
Stern D. et al., 2012, ApJ, 753, 30
Stritzinger M. et al., 2012, ApJ, 756, 173
Tonry J. L. et al., 2018, PASP, 130, 64505
Ulmer A., 1999, ApJ, 514, 180
Ulrich M.-H., Maraschi L., Urry C. M., 1997, ARA&A, 35, 445
van Velzen S., Stone N. C., Metzger B. D., Gezari S., Brown T. M., Fruchter
   A. S., 2019, ApJ, 878, 82
Vázquez-Mata J. A. et al., 2022, MNRAS, 512, 2222
Veres P. M. et al., 2024, preprint (arXiv:2408.17419)
Wang T.-G., Zhou H.-Y., Wang L.-F., Lu H.-L., Xu D., 2011, ApJ, 740, 85
Wang T.-G., Zhou H.-Y., Komossa S., Wang H.-Y., Yuan W., Yang C., 2012,
   ApJ, 749, 115
Wang Y. et al., 2024, ApJ, 966, 136
Westfall K. B. et al., 2019, AJ, 158, 231
Wiseman P. et al., 2023, MNRAS, 522, 3992
Wiseman P. et al., 2025, MNRAS, 537, 2024
Wright E. L. et al., 2010, AJ, 140, 1868
Yan R. et al., 2016, AJ, 152, 197
Yang C.-W., Wang T.-G., Ferland G., Yuan W., Zhou H.-Y., Jiang P., 2013,
   ApJ, 774, 46
Yao Y. et al., 2023, ApJ, 955, L6
Yaron O., Gal-Yam A., 2012, PASP, 124, 668
York D. G. et al., 2000, AJ, 120, 1579
Young D., 2024, Plot_atlas_fp.Py, Zenodo available at: https://zenodo.org/rec
   ords/10978969
```

Paliya V. S., Stalin C. S., Domínguez A., Saikia D. J., 2024, MNRAS, 527,

APPENDIX A: SAMPLE INFORMATION

In this appendix, we provide summary information on the properties of all objects used as the comparison sample within this work.

Server AstroNote, 236, 1 Newsome M. et al., 2024, ApJ, 977, 258

Nicholl M. et al., 2019, MNRAS, 488, 1878 Nicholl M. et al., 2024, Nature, 634, 804

Oke J. B. et al., 1995, PASP, 107, 375

Onori F. et al., 2022, MNRAS, 517, 76

Table A1. Summary information for the comparison sample of other objects used in this paper. AT 2018dyk is included for convenient reference.

Object	RA (J2000)	Dec. (J2000)	Redshift (z)	Host name
AT 2018dyk	15:33:08.0149	+ 44:32:08.2039	0.037	SDSS J153308.01+443208.4
CrL-TDEs				
AT 2017gge	16:20:34.9900	+24:07:26.5000	0.067	SDSS J162034.99+240726.5
AT 2018gn	01:46:42.4500	+ 32:30:29.3004	0.037	2MASX J01464244+3230295
AT 2018bcb	22:43:42.8710	-16:59:08.4913	0.120	2MASX J22434289-1659083
AT 2021dms	03:21:24.0695	-11:08:45.7120	0.031	MCG-02-09-033
AT 2021acak	10:34:47.9900	+ 15:29:22.4200	0.136	SDSS J103447.90+152922.4
TDE 2022fpx	15:31:03.7420	+ 53:24:19.1800	0.073	SDSS J153104.92+532409.2
TDE 2022upj	00:23:56.8459	-14:25:23.2198	0.054	SDSS J002356.88-142524.0
TDE-ECLEs				
SDSS J0748+4712	07:48:20.6668	+ 47:12:14.2648	0.062	2MASS J07482067+4712138
SDSS J0952+2143	09:52:09.5629	+21:43:13.2979	0.079	2MASS J09520955+2143132
SDSS J1241+4426	12:41:34.2561	+ 44:26:39.2636	0.042	LEDA 2244532
SDSS J1342+0530	13:42:44.4150	$+\ 05:30:56.1451$	0.037	2MASX J13424441+0530560
SDSS J1350+2916	13:50:01.4946	+ 29:16:09.6460	0.078	2MASS J13500150+2916097
CrL-TDEs/CrL-AGN				
VT J154843.06+220812.6	15:48:43.0662	+ 22:08:12.6866	0.031	SDSS J154843.06+220812.6
Multi-epoch CrL-TDEs				
AT 2019avd	08:23:36.7674	$+\ 04:23:02.4598$	0.028	SDSS J082338.23+042258.3
TDE 2019qiz	04:46:37.8800	-10:13:34.9000	0.015	2MASX J04463790-1013349
AGN-ECLEs				
SDSS J0938+1353	09:38:01.6376	+ 13:53:17.0423	0.101	SDSS J093801.63+135317.0
SDSS J1055+5637	10:55:26.4177	+ 56:37:13.1010	0.074	SDSS J105526.41+563713.1
NonCrL-TDEs				
TDE 2019azh	08:13:16.9450	+ 22:38:54.0300	0.022	KUG 0810+227
CL-LINERs				
iPTF16bco	15:54:40.2643	+ 36:29:51.9540	0.237	SDSS J155440.25+362952.0
AT 2018gkr	08:17:26.4190	$+\ 10:12:10.1088$	0.168	LEDA 3091244
AT 2018aij	12:54:03.7882	+49:14:52.9152	0.101	2MASX J12540375+4914533
AT 2018ivp	10:40:45.0027	$+\ 26:03:00.0328$	0.067	LEDA 1760642
AT 2018lnh	12:25:50.2978	+ 51:08:46.4244	0.046	2MASS J12255032+5108463
ZTF18aasuray	11:33:55.9457	+67:01:07.0572	0.040	2MASX J11335602+6701073

APPENDIX B: MIR ANALYSIS

B1 Additional variability analysis

To better quantify the MIR variability of AT 2018dyk and the comparison object sample, we explore the standard deviation (σ) and maximum change in magnitude (δ) in three phases: before outburst (A), during outburst (B), and post-outburst (C). For some objects, one or more of these phases have not been observed and so are omitted from the corresponding tables. The means for each classification of objects are also reported. For both individual *WISE* filters and in MIR colour, the CrL-TDEs including AT 2018dyk, are observed to be less variable than the AGN-ECLEs prior to outburst and display similar colour variability. AT 2018dyk has also been observed to have returned to pre-outburst levels of variability, with the other CrL-TDEs still in their outburst phases. As expected, during outburst the variability of the CrL-TDEs increases dramatically in both metrics. For comparison processes, AT 2018dyk is excluded from the calculation of the mean values of the remaining CrL-TDEs.

The δ_B values (i.e., maximum change in magnitudes during outburst) differ from the Δ values of overall maximum change as the Δ calculation includes the quiescent value as a reference point rather than just the internal maximal change in magnitude of the observations comprising the outburst.

B2 MIR power-law fitting parameters

Here, we present the results of the power-law fits to the MIR data for each of the objects within the comparison sample that have been shown to have variable coronal iron lines and classified as either a TDE-ECLE or a single epoch CrL-TDE. The results are detailed in Table B3 and presented visually with comparison to the raw data points for the updated fits for the CrL-TDEs considering all data points in Fig. B1 and for the CrL-TDEs where an early excess in the MIR light curves has been excluded in Fig. B2. Fits for CrL-TDEs are only shown where there are at least five epochs of observation following peak MIR luminosity. Additionally, the results for the updated fitting using all WISE data available for the TDE-ECLE sample is also given in Fig. B3.

B3 MIR outburst peak analysis

Here, in Table B4, we include the full-fitting parameters and statistical test results for the MIR outburst peak analysis as described in Section 7 and Fig. 9.

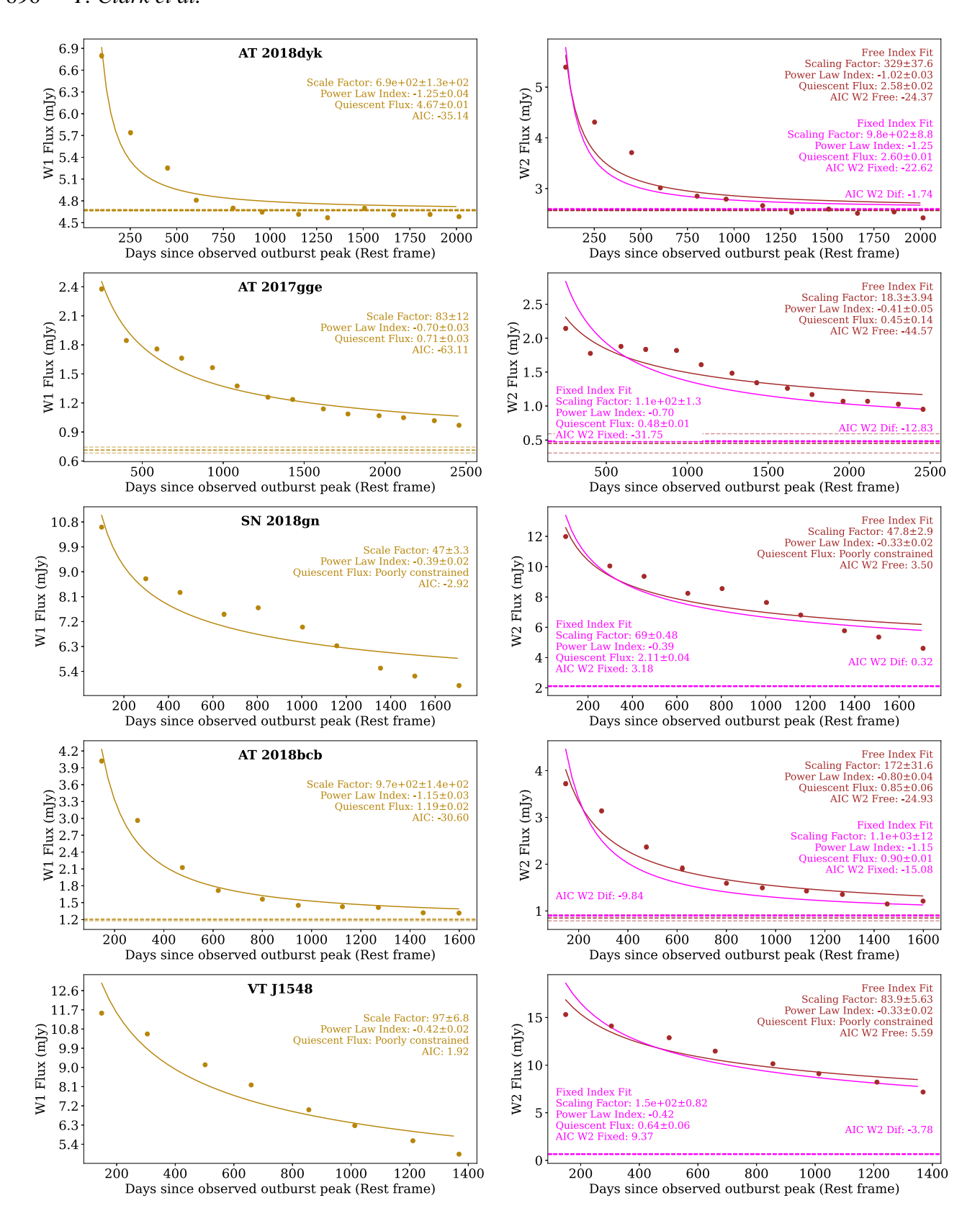


Figure B1. Power-law fits to the W1 (left) and W2 (right) photometry of the CrL-TDE sample where 5 or more epochs of observation have been obtained post MIR peak. Quiescent-flux values (C) are included when constrained by the fitting (C > 0 and $\Delta C < 0.15$) and shown by the dashed lines accompanied by the 1σ uncertainties. Method follows that of Clark et al. (2024) using the final NEOWISE-R release.

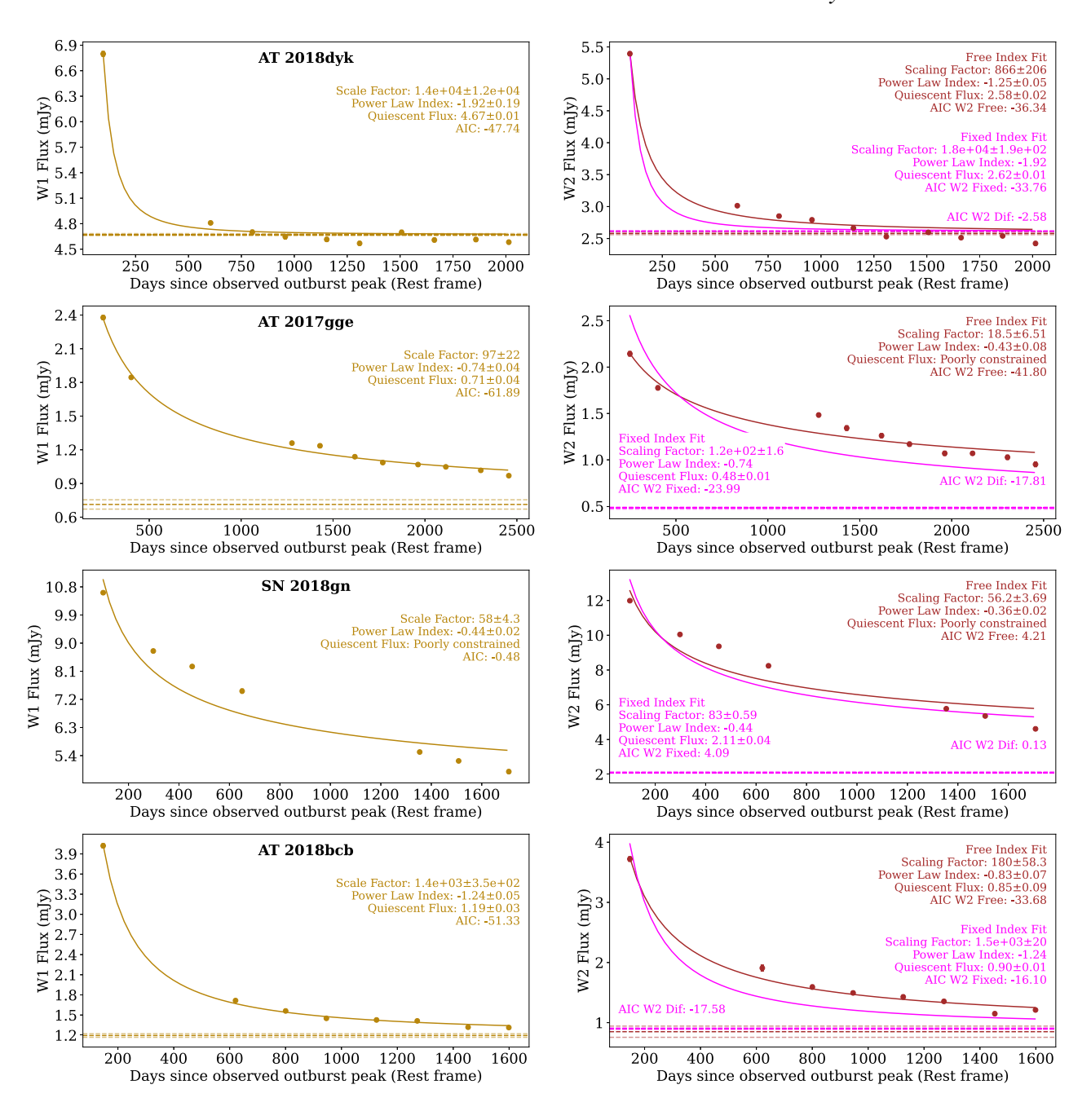


Figure B2. Power-law fits to the W1 (left) and W2 (right) photometry of the CrL-TDE sample where 5 or more epochs of observation have been obtained post-MIR peak and where an early excess is present within the MIR light curve with the observations from this excess removed. Quiescent-flux values (C) are included when constrained by the fitting (C > 0 and $\Delta C < 0.15$) and shown by the dashed lines accompanied by the 1σ uncertainties. Method follows that of Clark et al. (2024) using the final NEOWISE-R release.

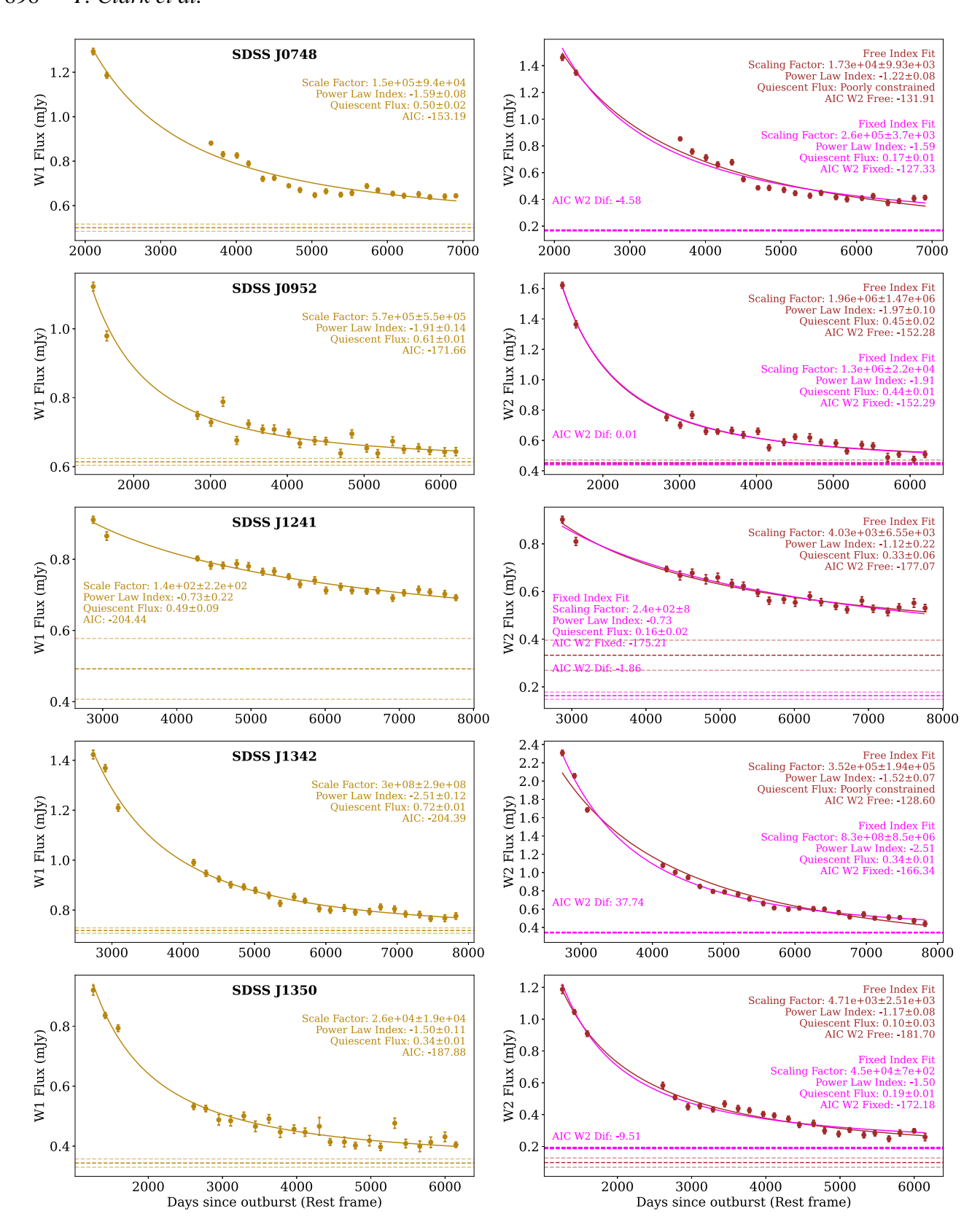


Figure B3. Power-law fits to the W1 (left) and W2 (right) photometry of the TDE-ECLE sample. Quiescent-flux values (C) are included when constrained by the fitting (C > 0 and $\Delta C < 0.15$) and shown by the dashed lines accompanied by the 1σ uncertainties. Method follows that of Clark et al. (2024) using the final NEOWISE-R release.

Table B1. Standard deviations of the per-band MIR light curve for each object divided in to three phases.

Object	Classification	$\sigma W1_{\rm A}$	σW1 _B	σW1 _C	σW2 _A	σW2 _B	σW2 _C	$\sigma(W1-W2)_{\rm A}$	$\sigma(W1-W2)_{\rm B}$	$\sigma(W1-W2)_{\rm C}$
AT 2018dyk	CrL-TDE	0.01	0.14	0.01	0.01	0.27	0.03	0.02	0.14	0.02
AT 2017gge	CrL-TDE	0.03	0.29	_	0.05	0.29	_	0.06	0.09	_
AT 2018gn	CrL-TDE	0.01	0.34	_	0.02	0.48	_	0.02	0.20	_
AT 2018bcb	CrL-TDE	0.03	0.38	_	0.06	0.41	_	0.06	0.09	_
AT 2021dms	CrL-TDE	0.02	0.29	_	0.03	0.49	_	0.04	0.23	_
TDE 2022fpx	CrL-TDE	0.08	0.41	_	0.10	0.61	_	0.08	0.05	_
TDE 2022upj	CrL-TDE	0.02	0.70	_	0.06	0.93	_	0.05	0.25	_
VT J1548	CrL-TDE	0.01	0.74	_	0.03	0.94	-	0.03	0.24	_
Mean	CrL-TDE*	0.03	0.45	-	0.05	0.59	-	0.05	0.15	_
AT 2019avd	Multi-epoch CrL-TDE/CrL-AGN	0.01	0.28	_	0.03	0.36	_	0.02	0.17	_
TDE 2019qiz	Multi-epoch CrL-TDE	0.02	0.24	-	0.02	0.49	-	0.02	0.26	_
Mean	Multi-epoch CrL-TDE	0.01	-	-	0.02	-	-	0.02	-	-
SDSS J0748+4712	TDE-ECLE	_	0.21	_	_	0.42	_	-	0.22	_
SDSS J0952+2143	TDE-ECLE	_	0.15	_	_	0.32	_	_	0.18	_
SDSS J1241+4426	TDE-ECLE	_	0.08	_	_	0.16	_	_	0.08	_
SDSS J1342+0530	TDE-ECLE	_	0.19	-	-	0.48	_	-	0.30	_
SDSS J1350+2916	TDE-ECLE	_	0.25	-	-	0.46	_	-	0.23	_
Mean	TDE-ECLE	-	0.17	-	-	0.37	-	-	0.20	-
SDSS J0938+1353	AGN-ECLE	0.04	_	_	0.03	_	_	0.02	_	_
SDSS J1055+5637	AGN-ECLE	0.13	-	-	0.14	-	-	0.03	_	_
Mean	AGN-ECLE	0.08	-	-	0.09	-	-	0.02	-	-
TDE 2019azh	NonCrL-TDE	0.02	-	0.02	0.02	-	0.03	0.02	-	0.02
iPTF16bco **	CL-LINER	0.09	0.05	0.04	0.13	0.07	0.04	0.07	0.05	0.04
AT 2018aij	CL-LINER	0.03	0.11	0.03	0.06	0.12	0.04	0.06	0.04	0.00
AT 2018gkr	CL-LINER	0.30	_	-	0.41	-	-	0.16	_	_
AT 2018ivp	CL-LINER	-	0.15	_	_	0.17	_	_	0.03	_
AT 2018lnh **	CL-LINER	0.09	0.17	_	0.12	0.11		0.06	0.09	
ZTF18aasuray	CL-LINER	_	0.24	_	_	0.34	_	_	0.11	_
Mean	CL-LINER	0.13	0.15	0.03	0.18	0.16	0.04	0.09	0.07	0.02

Notes. A: pre-outburst, B: during outburst, and C: post-outburst. Where an object's per-outburst behaviour has not been observed, 'A' phase values are not quoted, likewise for objects not displaying a clear outburst 'B' values are not quoted or where an object is still displaying outburst activity at time of the last observation where 'C' values are not possible to measure. Objects have been divided by classification, with group means (and the values for AT 2018dyk) shown in bold.

^{*} Excluding AT 2018dyk for comparison purposes. Given its occurrence within an AGN hosting galaxy, AT 2021acak is also excluded from this analysis.

^{**} MIR outbursts displayed by these objects and outlined here occur several years after the identification of the 'CL' event.

Table B2. Maximum changes of the per-band MIR light curves for each object divided in to three phases.

Object	Classification	$\delta W1_{ m A}$	$\delta W1_{ m B}$	$\delta W1_{\mathrm{C}}$	$\delta W2_{\rm A}$	$\delta W2_{ m B}$	$\delta W2_{\mathrm{C}}$	$\delta(W1-W2)_{\rm A}$	$\delta(W1-W2)_{\rm B}$	$\delta(W1-W2)_{\rm C}$
AT 2018dyk	CrL-TDE	0.04	0.38	0.03	0.05	0.63	0.18	0.05	0.35	0.10
AT 2017gge	CrL-TDE	0.10	0.97	_	0.15	0.88	_	0.19	0.29	_
AT 2018gn	CrL-TDE	0.05	1.24	_	0.05	1.81	_	0.07	0.68	_
AT 2018bcb	CrL-TDE	0.10	1.21	_	0.17	1.28	_	0.18	0.27	_
AT 2021dms	CrL-TDE	0.6	0.81	_	0.11	1.25	_	0.12	0.60	_
TDE 2022fpx	CrL-TDE	0.31	0.98	_	0.43	1.41	_	0.29	0.51	_
TDE 2022upj	CrL-TDE	0.08	1.50	_	0.22	2.00	_	0.17	0.55	_
VT J1548	CrL-TDE	0.04	2.47	-	0.07	3.25	-	0.08	0.90	-
Mean	CrL-TDE*	0.11	1.31	-	0.17	1.70	-	0.16	0.54	_
AT 2019avd	Multi-epoch CrL-TDE/CrL-AGN	0.04	0.98	_	0.09	1.08	_	0.07	0.53	-
TDE 2019qiz	Multi-epoch CrL-TDE	0.06	0.70	_	0.08	1.47	_	0.07	0.77	-
Mean	Multi-epoch CrL-TDE	0.05	-	-	0.08	-	-	0.07	-	-
SDSS J0748+4712	TDE-ECLE	_	0.77	_	_	1.48	_	_	0.74	_
SDSS J0952+2143	TDE-ECLE	_	0.61	_	_	1.33	_	-	0.73	_
SDSS J1241+4426	TDE-ECLE	-	0.30	-	-	0.61	-	_	0.35	_
SDSS J1342+0530	TDE-ECLE	_	0.67	_	_	1.80	_	-	1.14	_
SDSS J1350+2916	TDE-ECLE	-	0.91	-	-	1.70	-	_	0.89	_
Mean	TDE-ECLE	-	0.65	_	-	1.38	-	-	0.77	-
SDSS J0938+1353	AGN-ECLE	0.12	_	_	0.12	_	_	0.07	_	_
SDSS J1055+5637	AGN-ECLE	0.55	-	_	0.60	-	_	0.13	_	-
Mean	AGN-ECLE	0.33	_	_	0.36	-	-	0.10	-	-
TDE 2019azh	NonCrL-TDE	0.07	-	0.09	0.06	-	0.08	0.07	_	0.09
iPTF16bco **	CL-LINER	0.34	0.12	0.12	0.45	0.18	0.10	0.22	0.14	0.09
AT 2018aij	CL-LINER	0.09	0.24	0.08	0.15	0.31	0.10	0.19	0.13	0.06
AT 2018gkr	CL-LINER	0.93	_	_	1.17	_	_	0.55	_	_
AT 2018ivp	CL-LINER	_	0.54	_	_	0.61	_	_	0.15	_
AT 2018lnh **	CL-LINER	0.33	0.41	_	0.42	0.26	_	0.18	0.22	_
ZTF18aasuray	CL-LINER	_	0.71	_	_	0.94	_	_	0.33	_
Mean	CL-LINER	0.42	0.4	0.10	0.55	0.46	0.10	0.28	0.19	0.08

Notes. A: pre-outburst, B: during outburst, and C: post-outburst. Where an object's per-outburst behaviour has not been observed, 'A' phase values are not quoted, likewise for objects not displaying a clear outburst 'B' values are not quoted or where an object is still displaying outburst activity at time of the last observation where 'C' values are not possible to measure. Objects have been divided by classification, with group means (and the values for AT 2018dyk) shown in bold.

^{*} Excluding AT 2018dyk for comparison purposes. Given its occurrence within an AGN hosting galaxy, AT 2021acak is also excluded from this analysis.

^{**} MIR outbursts displayed by these objects and outlined here occur several years after the identification of the 'CL' event.

Downloaded from https://academic.oup.com/mnras/article/540/1/871/8124822 by Hartley Library user on 11 August 2025

Table B3. MIR power-law fitting parameters. Model selected reflects a standard power-law decay typical of TDEs with a luminosity floor reflecting the quiescent galaxy luminosity as was favoured in earlier analyses (Dou et al. 2016; Clark et al. 2024). Following Clark et al. 2024, fitting in the W1 and W2 bands is initially independent (Free fits) though due to the poorly constrained nature of some of the W2 quiescent flux values the results of fitting the W2 data where the decay index B is fixed to that of the W1 band are also reported. The results of fitting are compared through an AIC test, with the 'Free' fits being preferred in all cases at some level where a statistical preference is displayed with the exception of SDSS J1342+0530, though as the decay law index is the most important parameter in this analysis, the values included in the main text (Fig. 7) reflect the results of the 'Free' fit. As described in the main text, several CrL-TDEs (including AT 2018dyk) display light-curve 'bumps' or 'shoulders' (deviations from smooth declines) and we report fits to the data both including (all points) or excluding (excess exclusion) these lightcurve regions from the fitting. The fits to the data themselves are shown in Figs B1-B3.

					Model:	Model: $f(t) = At^{B} + C$				
Object	A_{W1}	B_{W1}	C_{W1} (mJy)	AW2Free	$B_{W2 \mathrm{Free}}$	Cw2Free (mJy)	A_{W2} Fixed	$C_{W2 Fixed}$ (mJy) $\Delta AIC_{Free-Fixed}$	AAIC Free - Fixed †	$\mathbf{\Delta AIC}_{\mathbf{Excluded}-\mathbf{All}}\square$
AT 2018dyk All points	690.27±125.00	−1.25±0.04	4.67±0.01	329.29±37.62	-1.02±0.03	2.58±0.02	979.43±8.85	2.60±0.01	-1.74	:
Excess exclusion	13969.49 ± 12120.68	-1.92 ± 0.19	4.67 ± 0.01	866.42 ± 206.39	-1.25 ± 0.05	2.58 ± 0.02	18452.22 ± 187.25	2.62 ± 0.01	-2.58	-9.60, -11.97
CrL-TDES										
AT 2017gge – all points	83.31 ± 11.88	-0.70 ± 0.03	0.71 ± 0.03	18.31 ± 3.94	-0.41 ± 0.05	0.45 ± 0.14	112.70 ± 1.26	0.48 ± 0.01	-12.83	:
AT 2017gge – excess exclusion	97.38±22.22	-0.74 ± 0.04	0.71 ± 0.04	18.55 ± 6.51	-0.43 ± 0.08	$0.45\pm0.20*$	122.20 ± 1.57	0.48 ± 0.01	-17.81	1.22, 2.77
SN 2018gn – all points	46.92 ± 3.31	-0.39 ± 0.02	3.36±0.25*	47.83±2.90	-0.33 ± 0.02	2.05±0.44*	68.90 ± 0.48	2.11 ± 0.04	0.32	:
SN 2018gn – excess exclusion	57.55±4.33	-0.44 ± 0.02	$3.36\pm0.21*$	56.18 ± 3.69	-0.36 ± 0.02	$2.05\pm0.37*$	83.19 ± 0.59	2.11 ± 0.04	0.13	2.51, 1.01
AT 2018bcb – all points	968.83 ± 137.60	-1.15 ± 0.03	1.19 ± 0.02	171.76 ± 31.61	-0.80 ± 0.04	0.85 ± 0.06	1134.85 ± 12.20	0.90 ± 0.01	-9.84	:
AT 2018bcb – excess exclusion	1386.85 ± 345.24	-1.24 ± 0.05	1.19 ± 0.03	179.55 ± 58.28	-0.83 ± 0.07	0.85 ± 0.09	1503.32 ± 19.59	0.90 ± 0.01	-17.58	-20.73, -8.75
VT J154843.06+220812.6	<i>9</i> 6.70±6.77	-0.42 ± 0.02	$1.07\pm0.33*$	83.91 ± 5.63	-0.33 ± 0.02	$0.61\pm0.74*$	146.22 ± 0.82	0.64 ± 0.06	-3.78	:
TDE-ECLES										
SDSS J0748+4712	$1.54e + 05\pm9.38e + 04$	-1.59 ± 0.08	0.50 ± 0.02	$1.73e + 04\pm9.93e + 03$	-1.22 ± 0.08	0.00 ± 0.05	$2.63e + 05\pm3.72e + 03$	0.17 ± 0.01	-4.58	
SDSS J0952+2143	$5.67e + 05\pm5.54e + 05$	-1.91 ± 0.14	0.61 ± 0.01	$1.96e + 06\pm1.47e + 06$	-1.97 ± 0.10	0.45 ± 0.02	$1.34e + 06\pm2.18e + 04$	0.44 ± 0.01	0.01	
SDSS J1241+4426	139±219	-0.73 ± 0.22	0.49 ± 0.09	$4.03e + 03\pm6.55e + 03$	-1.12 ± 0.22	0.33 ± 0.06	241±7.96	0.16 ± 0.02	-1.86	
SDSS J1342+0530	$3.03e + 08\pm2.95e + 08$	-2.51 ± 0.12	0.72 ± 0.01	$3.52e + 05\pm1.94e + 05$	-1.52 ± 0.07	0.00 ± 0.05	$8.26e + 08\pm8.49e + 06$	0.34 ± 0.01	37.74	
SDSS J1350+2916	$2.58e + 04\pm1.91e + 04$	-1.50 ± 0.11	0.34 ± 0.01	$4.71e + 03\pm2.51e + 03$	-1.17 ± 0.08	0.10 ± 0.03	$4.46e + 04\pm699$	0.19 ± 0.01	-9.51	

Notes. For the 'W2 fixed' parameters, the value of B was set to match that determined by the W1 fitting. Fits defined as 'excess exclusion' have the points post peak showing flux excesses removed prior to the fitting. * Indicates a poorly constrained quiescent flux value, i.e., where $C \le 0$ or $\Delta C \ge 0.15$

† In this case, a negative value indicates that the 'Free' index fit is more favoured.

☐ For this comparison, the more favoured 'Free' fits are compared and a negative value indicates the fit excluding the early excess points is more favoured. Given as two values: W1 and W2 values.

Table B4. Fitting parameters obtained in the Δ value analysis. Data and fits shown in Fig. 9.

	Model	Parameter	Value	t-statistic	<i>p</i> -value	σ
ΔW2 versus ΔW1	Quadratic *					
		a	-0.18	-2.26	1.09e - 01	1.60
		b	0.7	3.13	5.23e - 02	1.94
		c	-0.48	-4.34	2.26e - 02	2.28
$\Delta(W1 - W2)$ versus $\Delta W2$	Linear \Box					
		m	-0.25	-5.65	2.99e - 02	2.17
		c	0.19	2.99	9.59e - 02	1.67

Notes. * Selected through maximum-likelihood analysis and AIC value comparison between a fixed constant, a linear model and a quadratic model Selected through maximumlikelihood analysis and AIC value comparison between a fixed constant and a linear model. A quadratic model was not included in this comparison due to the small number of data points (3) available for inclusion

APPENDIX C: EMISSION -LINE FITTING

Here, we report the results of the emission-line fitting conducted for the spectra of AT 2018dyk and the comparison TDE-ECLE SDSS J1342+0530. Tables C1 and C2 summarize the fitting information for the non-coronal and coronal lines, respectively. Similarly,

Table C3 summarizes the resulting line ratios. Note that whilst the emission lines here are measured following correction for the local continuum, they have not been specifically corrected for stellar absorption and should thus be used primarily for relative comparisons.

Downloaded from https://academic.oup.com/mnras/article/540/1/871/8124822 by Hartley Library user on 11 August 2025

Table C1. Emission-line fitting results for non-coronal lines. Dots indicate where an emission feature/component was not detected in the given spectrum. Lines are fitted with independent properties, with the exception of the [N II] which are tied during fitting to have the same Gaussian standard deviations.

$ \begin{array}{cccccccccccccccccccccccccccccccccccc$	AT 2018dyk		SDSS: -5853 d			MaNGA: -560 d			Keck: +23 d			DESI: + 1873 d	
$ \begin{array}{cccccccccccccccccccccccccccccccccccc$	Feature	EQW (Å)	Offset V (km s ⁻¹)	FWHM V (km s^{-1})		Offset V (km s ⁻¹)	FWHM V (km s^{-1})	EQW (Å)	Offset V (km s ⁻¹)	FWHM V (km s^{-1})		Offset V (km s ⁻¹)	FWHM V (km s^{-1})
$ \begin{array}{cccccccccccccccccccccccccccccccccccc$	[O1]\(\chi_{6300}\\\\\\\\\\\\\\\\\\\\\\\\\\\\\\\\\\\	:	:	:	:	:	:	:	:	:	:	:	:
$ \begin{array}{cccccccccccccccccccccccccccccccccccc$	[OII] Doublet *	-3.6 ± 1.2	120 ± 20	330 ± 60	-3.8 ± 1.1	140 ± 20	360 ± 60	-1.0 ± 0.7	09 ∓ 06	360 ± 140	-4.9 ± 1.9	160 ± 30	370 ± 70
$ \begin{array}{cccccccccccccccccccccccccccccccccccc$	[Ош]λ4959 Å	:	:	:	:	:	:	:	:	:	-0.5 ± 0.3	140 ± 30	210 ± 60
$ \begin{array}{cccccccccccccccccccccccccccccccccccc$	[O III]\(\frac{1}{2}\)5007 \(\hat{A}\)	-1.2 ± 0.3	110 ± 20	290 ± 40	-1.0 ± 0.1	110 ± 10	280 ± 20	-2.4 ± 0.6	60 ± 30	560 ± 80	-2.8 ± 0.6	120 ± 10	280 ± 30
$ \begin{array}{cccccccccccccccccccccccccccccccccccc$	$H\alpha$ narrow	-0.5 ± 0.3	90 ± 30	260 ± 70	-0.4 ± 0.2	70 ± 20	180 ± 50	-23.9 ± 0.7	50 ± 10	790 ± 290	-0.5 ± 0.3	90 ± 30	200 ± 60
$ \begin{array}{cccccccccccccccccccccccccccccccccccc$	$H\alpha$ broad	:	:	:	:	:	:	-22.6 ± 1.7	80 ± 20	2350 ± 1010	:	:	:
$ \begin{array}{cccccccccccccccccccccccccccccccccccc$	[N II]\(\chi 6548 \hat{A}\)	-1.3 ± 0.2	50 ± 20	370 ± 20	-1.1 ± 0.2	70 ± 20	340 ± 20	-1.7 ± 0.3	30 ± 10	380 ± 30	-1.1 ± 0.2	50 ± 20	310 ± 20
$ \begin{array}{c ccccccccccccccccccccccccccccccccccc$	[NII]\(\chi_6584\) Å	-3.2 ± 0.3	70 ± 10	370 ± 20	-2.9 ± 0.3	70 ± 20	340 ± 20	-3.1 ± 0.4	-40 ± 20	380 ± 30	-3.5 ± 0.3	70 ± 10	310 ± 20
$ \begin{array}{c ccccccccccccccccccccccccccccccccccc$	[S II]λ6717 Å	-0.9 ± 0.2	120 ± 20	340 ± 20	-0.8 ± 0.1	70 ± 10	340 ± 20	-0.5 ± 0.2	0 ± 30	360 ± 40	-0.9 ± 0.2	40 ± 20	280 ± 30
$ \begin{array}{c ccccccccccccccccccccccccccccccccccc$	[Sπ]λ6731 Å	-1.0 ± 0.2	70 ± 20	340 ± 20	-0.8 ± 0.1	80 ± 10	330 ± 20	-0.7 ± 0.2	-20 ± 30	360 ± 40	-0.9 ± 0.2	70 ± 20	280 ± 30
$ \begin{array}{cccccccccccccccccccccccccccccccccccc$	$H\beta$	2.6 ± 0.1	190 ± 40	1000 ± 100	2.9 ± 0.1	190 ± 30	1000 ± 70	-9.5 ± 0.5	30 ± 10	1040 ± 30	1.9 ± 0.1	130 ± 70	830 ± 160
EQW $(km s^{-1})$ $(km s^{-1}$	SDSS J1342+0530 *:		3DSS: MID 52373			JAMT: MTD 55021			DECI. MID 50270				
$ \begin{array}{cccccccccccccccccccccccccccccccccccc$			Offset V			Offset V	FWHM V		Offset V	FWHM V			
$\begin{array}{cccccccccccccccccccccccccccccccccccc$	Feature	(Å)	$(km s^{-1})$	(km s^{-1})	(Å)	$(km s^{-1})$	$(\mathrm{km}\ \mathrm{s}^{-1})$	(Å)	$(km \ s^{-1})$	(km s^{-1})			
$ \begin{array}{cccccccccccccccccccccccccccccccccccc$	[O1]\(\chi_{6300}\)\(\hat{A}\)	-1.2 ± 0.6	-70 ± 100	820 ± 230	-1.5 ± 0.3	-80 ± 10	260 ± 30	-1.0 ± 0.4	100 ± 10	150 ± 30			
$\begin{array}{cccccccccccccccccccccccccccccccccccc$	[OII] Doublet *	-9.0 ± 1.5	150 ± 10	350 ± 30	Ont	of wavelength cover	rage	-10.8 ± 3.7	130 ± 30	370 ± 70			
$\begin{array}{cccccccccccccccccccccccccccccccccccc$	[O III]λ4959 Å	-0.9 ± 0.3	100 ± 20	190 ± 40	-5.3 ± 0.5	-100 ± 10	280 ± 20	-12.1 ± 0.9	100 ± 10	220 ± 10			
$\begin{array}{cccccccccccccccccccccccccccccccccccc$	[O III]\(\chi_{\text{5007}}\) Å	-4.5 ± 0.4	70 ± 10	250 ± 10	-14.4 ± 1.4	-90 ± 10	350 ± 20	-38.7 ± 2.1	90 ± 10	200 ± 10			
$\begin{array}{cccccccccccccccccccccccccccccccccccc$	$H\alpha$ narrow	-13.0 ± 0.5	70 ± 10	250 ± 10	-13.1 ± 0.7	-80 ± 10	330 ± 10	-17.1 ± 0.6	110 ± 10	180 ± 10			
$\begin{array}{cccccccccccccccccccccccccccccccccccc$	$H\alpha$ broad	:	:	:	:	:	:	:	:	:			
$\begin{array}{cccccccccccccccccccccccccccccccccccc$	[N II]\(\chi 6548 \hat{A}\)	-1.8 ± 0.4	190 ± 20	330 ± 30	-2.0 ± 0.4	-80 ± 20	260 ± 20	-2.4 ± 0.3	100 ± 10	190 ± 10			
$\begin{array}{cccccccccccccccccccccccccccccccccccc$	[N11]λ6584 Å	-3.4 ± 0.5	80 ± 10	330 ± 30	-5.0 ± 0.6	$-118.39 \pm$	260 ± 20	-7.0 ± 0.6	70 ± 10	190 ± 10			
$\begin{array}{cccccccccccccccccccccccccccccccccccc$						10							
$\begin{array}{cccccccccccccccccccccccccccccccccccc$	[S II]λ6717 Å	-1.4 ± 0.2	90 ± 10	280 ± 20	-1.5 ± 0.3	-100.41 ± 10	220 ± 20	-1.9 ± 0.4	90 ± 10	190 ± 20			
40 ± 10 210 ± 10 -3.3 ± 0.3 -90 ± 6 300 ± 10 -4.7 ± 0.9 110 ± 10	[SII]\(\chi 6731 \text{\text{\text{\deft}}}\)	-1.4 ± 0.2	100 ± 10	280 ± 20	-1.2 ± 0.2	-65.60 ± 10	220 ± 20	-2.0 ± 0.4	90 ± 10	190 ± 20			
	$H\beta$	-2.2 ± 0.2	40 ± 10	210 ± 10	-3.3 ± 0.3	$9 \mp 06 -$	300 ± 10	-4.7 ± 0.9	110 ± 10	190 ± 20			

when, we foul bounder is a single Gaussian into the JOHJ 720 A and JOHJ 720 A chrission times which, at the resolution of ** The evolutionary phase of this object is not well constrained. As such, we report the MJD of each spectrum rather than phase.

Table C2. Emission-line fitting results for the coronal lines.

AT 2018dyk *			
		Keck: +23 d	
	EQW	Offset V	FWHM V
Feature	(Å)	(km s^{-1})	(km s^{-1})
[Fe VII]λ3759 Å	-2.5 ± 0.8	200 ± 60	840 ± 150
[Fe VII]λ5160 Å			
[Fe VII]λ5722 Å	-1.9 ± 0.4	120 ± 30	640 ± 60
[Fe VII]λ6088 Å	-2.1 ± 0.3	50 ± 20	640 ± 50
[Fe x]λ6376 Å	-2.5 ± 0.4	-50 ± 30	950 ± 80
[Fe xι]λ7894 Å	-1.0 ± 0.3	-220 ± 40	650 ± 100
[Fe XIV]λ5304 Å	-2.6 ± 1.0	130 ± 110	1370 ± 290

SDSS J1342+0530 **

	S	DSS: MJD 5237	73	M	MT: MJD 559	21	DI	ESI: MJD 592	79
Feature	EQW (Å)	Offset V (km s ⁻¹)	FWHM V (km s-1)	EQW (Å)	Offset V (km s ⁻¹)	$\begin{array}{c} \text{FWHM V} \\ (\text{km s}^{-1}) \end{array}$	EQW (Å)	Offset V (km s ⁻¹)	$\begin{array}{c} FWHM V \\ (km s^{-1}) \end{array}$
[Fe VII]λ3759 Å				Out of	wavelength co	verage	-2.8 ± 1.9	200 ± 20	150 ± 60
[Fe VII]λ5160 Å				-0.9 ± 0.5	-70 ± 30	250 ± 80			
[Fe VII]λ5722 Å				-1.7 ± 0.3	-90 ± 10	260 ± 20	-1.8 ± 0.5	110 ± 20	250 ± 40
[Fe VII]λ6088 Å				-2.2 ± 0.2	-100 ± 10	250 ± 10	-1.2 ± 0.5	40 ± 20	160 ± 40
[Fe x]λ6376 Å	-2.3 ± 0.4	20 ± 10	310 ± 30	-0.8 ± 0.3	-220 ± 20	300 ± 50			
[Fe xι]λ7894 Å	-3.2 ± 0.3	10 ± 10	310 ± 20	Out of	wavelength co	verage			
[Fe XIV]λ5304 Å	-1.5 ± 0.5	40 ± 30	340 ± 60	Out of	wavelength co	verage		•••	

Notes. * Only the Keck spectrum is included here as no coronal lines were observed in any of the other spectra.

^{**} The evolutionary phase of this object is not well constrained. As such, we report the MJD of each spectrum rather than phase.

Table C3. Emission-line ratios determined through Gaussian fitting.

AT 2018dyk				
	SDSS: -5853 d	MaNGA: −560 d	Keck: +19 d	DESI: +1873
Line ratio				
$\log_{10}([N II] / H\alpha)$	0.8 ± 0.2	0.9 ± 0.2	2.4 ± 0.2	0.9 ± 0.3
log ₁₀ ([O III]λ5007 Å /Hβ)	• • •	• • •	-0.6 ± 0.1	
$\log_{10}([S II]\lambda 6717, 6731 \text{ Å /H}\alpha)$	0.5 ± 0.2	0.6 ± 0.2	2.0 ± 0.3	0.6 ± 0.3
log ₁₀ ([O I] 6300 Å / Hα)	0.3 ± 0.3	0.5 ± 0.3	1.9 ± 0.3	0.3 ± 0.4
[O III]λ5007 Å / [O III]λ4959 Å				4.6 ± 2.7
[S II]λ6717 Å / [S II]λ6731 Å	1.0 ± 0.2	1.1 ± 0.2	0.7 ± 0.3	1.0 ± 0.3
[Fe VII]λ3759 Å / [O III]λ5007 Å			1.1 ± 0.5	
[Fe VII]λ5160 Å / [O III]λ5007 Å	• • •		***	
[Fe VII]λ5722 Å / [O III]λ5007 Å	• • •		1.6 ± 0.5	
[Fe VII]λ6088 Å / [O III]λ5007 Å			1.8 ± 0.5	
[Fe x]λ6376 Å / [O III]λ5007 Å		•••	2.1 ± 0.6	
[Fe xI]λ7894 Å / [O III]λ5007 Å		•••	0.8 ± 0.3	
[Fe xiv]λ5304 Å / [O iii]λ5007 Å			1.1 ± 0.5	
[Fe VII]\(\lambda\)3759 \(\hat{A}\) / [Fe VII]\(\lambda\)6088 \(\hat{A}\)		•••	0.6 ± 0.2	
[Fe VII]λ5160 Å / [Fe VII]λ6088 Å				
[Fe VII]\\(\lambda\)5722 \(\lambda\) / [Fe VII]\\(\lambda\)6088 \(\lambda\)			0.9 ± 0.2	
[Fe x]λ6376 Å / [Fe vII]λ6088 Å			1.2 ± 0.2	
[Fe xi]\(\lambda\)7894 \(\lambda\) / [Fe vii]\(\lambda\)6088 \(\lambda\)			0.4 ± 0.1	
[Fe xiv]\(\text{\text{3}}\) [Fe vii]\(\text{\text{6}}\) [Fe viii]\(\text{\text{6}}\) [Fe viii]\(\text{\text{6}}\)			0.6 ± 0.3	
SDSS J1342+0530*				
5555 g1c 12 05504	SDSS: MJD 52373	MMT: MJD 55921	DESI: MJD 59279	
Line ratio				
$\log_{10}([N II] / H\alpha)$	-0.6 ± 0.1	-0.4 ± 0.1	-0.4 ± 0.1	
$\log_{10}([O \text{III}]\lambda 5007 \text{Å} / \text{H}\beta)$	0.3 ± 0.1	0.6 ± 0.1	0.9 ± 0.1	
$\log_{10}([S II]\lambda 6717, 6731 \text{ Å}/H\alpha)$	-0.7 ± 0.1	-0.7 ± 0.1	-0.6 ± 0.1	
$\log_{10}([\text{O I}]\lambda6300 \text{ Å} / \text{H}\alpha)$	-1.0 ± 0.2	-0.9 ± 0.1	-1.2 ± 0.2	
[O III]λ5007 Å / [O III]λ4959 Å	4.7 ± 1.7	2.4 ± 0.3	3.0 ± 0.3	
[S II]\(\lambda\) A / [S II]\(\lambda\) A	1.0 ± 0.3	1.2 ± 0.3	1.0 ± 0.3	
[Fe VII]λ3759 Å / [O III]λ5007 Å		Out of wavelength coverage	0.1 ± 0.1	
[Fe VII] λ 5160 Å / [O III] λ 5007 Å	•••	0.1 ± 0.1		
[Fe VII] λ 5722 Å / [O III] λ 5007 Å	•••	0.1 ± 0.1 0.1 ± 0.1	0.1 ± 0.1	
[Fe VII] λ 6088 Å / [O III] λ 5007 Å		0.2 ± 0.1	0.1 ± 0.1 0.1 ± 0.1	
[Fe x]λ6376 Å / [O III]λ5007 Å	0.5 ± 0.1	0.2 ± 0.1 0.1 ± 0.1	0.1 ± 0.1	
[Fe xi]λ7894 Å / [O iii]λ5007 Å	0.5 ± 0.1 0.5 ± 0.1	0.1 ± 0.1 0.2 ± 0.1		
[Fe XIV]λ5304 Å / [O III]λ5007 Å	0.3 ± 0.1 0.4 ± 0.1	Out of wavelength coverage	•••	
[Fe VII]λ3759 Å / [Fe VII]λ6088 Å	0.4 ± 0.1	Out of wavelength coverage	1.1 ± 0.9	
[Fe VII]\(\lambda 5160 \text{ Å / [Fe VII]\(\lambda 6088 \text{ Å}\)	•••	Out of wavelength coverage 0.4 ± 0.2	1.1 ± 0.9	
[Fe VII]λ5160 A / [Fe VII]λ6088 A [Fe VII]λ5722 Å / [Fe VII]λ6088 Å	•••	0.4 ± 0.2 0.8 ± 0.2	1.5 ± 0.8	
	•••	0.8 ± 0.2 0.4 ± 0.1	1.5 ± 0.8	
[Fe x]λ6376 Å / [Fe vII]λ6088 Å [Fe xI]λ7894 Å / [Fe vII]λ6088 Å		0.4 ± 0.1 1.4 ± 0.2	•••	

Note.* The evolutionary phase of this object is not well constrained. As such, we report the MJD of each spectrum rather than phase.

Out of wavelength coverage

APPENDIX D: EMISSION-LINE VIRIAL DISTANCE ESTIMATES

[Fe XIV]λ5304 Å / [Fe VII]λ6088 Å

In this appendix, we summarize the virial distance measurements measured from the FWHM of the narrow emission lines as described in Section 4.1.

Table D1. Virial distance measurements determined from the FWHM velocities of the narrow emission features.

AT 2018dyk				
	SDSS: -5853 d	MaNGA: −560 d	Keck: +19 d	DESI: +1873 d
	Virial distance	Virial distance	Virial distance	Virial distance
Feature	(pc)	(pc)	(pc)	(pc)
[Fe VII]λ5722 Å	•••	•••	0.08 ± 0.02	
[Fe VII]λ6088 Å			0.08 ± 0.02	
[Fe x]λ6376 Å			0.03 ± 0.01	
[Fe XI]λ7894 Å			0.07 ± 0.02	
[Fe XIV]λ5304 Å			0.02 ± 0.01	
[O II] Doublet *	0.29 ± 0.11	0.24 ± 0.09	0.24 ± 0.19	0.23 ± 0.09
[O III]λ4959 Å		•••	• • •	0.71 ± 0.41
[O III]λ5007 Å	0.37 ± 0.11	0.40 ± 0.07	0.10 ± 0.03	0.40 ± 0.10
Ηα	0.46 ± 0.26	0.97 ± 0.55	0.05 ± 0.04	0.78 ± 0.48
$H\beta$	0.03 ± 0.01	0.03 ± 0.01	0.03 ± 0.01	0.05 ± 0.02
[NII] **	0.23 ± 0.04	0.27 ± 0.05	0.22 ± 0.04	0.33 ± 0.06
[S II] ***	0.27 ± 0.05	0.28 ± 0.05	0.24 ± 0.06	0.40 ± 0.10

Notes. * The '[O II] Doublet' is a single Gaussian fit to the [O II] λ 3726 and 3728 Å emission lines which, at the resolution of the available spectra, are too blended to be separated.

This paper has been typeset from a TEX/LATEX file prepared by the author.

^{** &#}x27;[N II]' here represents both the [N II]\\(\delta\)6548 and 6585 Å emission lines as these were tied to have the same width during the fitting process.

^{*** &#}x27;[S II]' here represents both the [S II] λ 6717 and 6731 Å emission lines as these were tied to have the same width during the fitting process. SMBH mass used for these calculations is $7.27 \times 10^6 \pm 8.64 \times 10^5 \, \mathrm{M}_{\odot}$.

¹School of Physics and Astronomy, University of Southampton, Southampton SO17 1BJ, UK

²Institute of Cosmology and Gravitation, University of Portsmouth, Portsmouth PO1 3FX, UK

³Department of Astrophysics, American Museum of Natural History, New York, NY 10024, USA

⁴Centre for Extragalactic Astronomy, Department of Physics, Durham University, South Road, Durham DH1 3LE, UK

⁵McWilliams Center for Cosmology and Astrophysics, Department of Physics, Carnegie Mellon University, 5000 Forbes Ave, Pittsburgh, 15213 PA, USA ⁶Lawrence Berkeley National Laboratory, 1 Cyclotron Road, Berkeley, CA 94720, USA

⁷Physics Department, Boston University, 590 Commonwealth Avenue, Boston, MA 02215, USA

⁸Dipartimento di Fisica 'Aldo Pontremoli', Università degli Studi di Milano, Via Celoria 16, I-20133 Milano, Italy

⁹Department of Physics & Astronomy, University College London, Gower Street, London WC1E 6BT, UK

¹⁰Department of Physics and Astronomy, The University of Utah, 115 South 1400 East, Salt Lake City, UT 84112, USA

¹¹ Instituto de Física, Universidad Nacional Autónoma de México, Circuito de la Investigación Científica, Ciudad Universitaria, Cd. de México C. P. 04510. México

¹² Fermi National Accelerator Laboratory, PO Box 500, Batavia, IL 60510, USA

¹³ Center for Cosmology and AstroParticle Physics, The Ohio State University, 191 West Woodruff Avenue, Columbus, OH 43210, USA

¹⁴Department of Physics, The Ohio State University, 191 West Woodruff Avenue, Columbus, OH 43210, USA

¹⁵NSF NOIRLab, 950 N. Cherry Ave., Tucson, AZ 85719, USA

¹⁶Department of Physics, Southern Methodist University, 3215 Daniel Avenue, Dallas, TX 75275, USA

¹⁷CNRS/IN2P3, Laboratoire de Physique Nucléaire et de Hautes Energies (LPNHE), Sorbonne Université, FR-75005 Paris, France

¹⁸Institució Catalana de Recerca i Estudis Avançats, Passeig de Lluís Companys, 23, E-08010 Barcelona, Spain

¹⁹Institut de Física d'Altes Energies (IFAE), The Barcelona Institute of Science and Technology, Edifici Cn, Campus UAB, E-08193 Bellaterra (Barcelona). Spain

²⁰Department of Physics and Astronomy, Siena College, 515 Loudon Road, Loudonville, NY 12211, USA

²¹Departament de Física, EEBE, Universitat Politècnica de Catalunya, c/Eduard Maristany 10, E-08930 Barcelona, Spain

²²CIEMAT, Avenida Complutense 40, E-28040 Madrid, Spain

²³Department of Physics, University of Michigan, 450 Church Street, Ann Arbor, MI 48109, USA

²⁴National Astronomical Observatories, Chinese Academy of Sciences, A20 Datun Rd., Chaoyang District, Beijing 100012, P. R. China